Separation of Tread-pattern Noise in Tire-pavement Interaction Noise

Jianxiong Feng

Thesis submitted to the Faculty of the Virginia Polytechnic Institute and State University in partial fulfillment of the requirements for the degree of

Master of Science
in
Mechanical Engineering

Ricardo A. Burdisso, Co-Chair

Corina Sandu, Co-Chair

Wing F. Ng, Member

02/10/2017

Blacksburg, Virginia

Keywords: tire-pavement interaction tire noise; tread pattern parameters; order tracking analysis; synchronous averaging; signal processing techniques

Separation of Tread-pattern Noise in Tire-pavement Interaction Noise

Jianxiong Feng

ABSTRACT

Tire-pavement interaction noise is one of the dominant sources of vehicle noise, and one of the most significant sources of urban noise pollution. One critical generation mechanism of tire-pavement interaction noise is tire tread excitation. The tire tread contributes to the tire-pavement interaction noise mainly through two mechanisms: (1) tread block impact, and (2) the compression and expansion of the air in the tread groove at the contact patch. The tread pattern is the critical part of the tire design since it can be easily modified. Hence, the main focus of this study is to quantify the tread pattern contribution in total tire-pavement interaction noise. To achieve this goal, the noise produced by the tread pattern is separated from the total tire-pavement interaction noise. Since the tread pattern excitation is periodic with tire rotation, the noise produced by the tread is assumed to be related to the tire rotation. Hence, the order domain synchronous averaging method is used in this study to separate and quantify the tread pattern contribution to the total tire-pavement interaction noise. The experiment has been carried out using an On-Board-Sound-Intensity (OBSI) system. Five tires were tested including the Standard Reference Test Tire (SRTT). Compared to the conventional OBSI system, an optical sensor was added to the system to monitor the tire rotation. The once per revolution signal provided by the optical sensor is used to identify the noise signals associate to each revolution.

In addition to the averaging method using optical signals, other data processing techniques have been investigated for separating the tread-pattern noise without utilizing the once per revolution signal. These techniques are autocorrelation analysis, a frequency domain filter, principal component analysis, and independent component analysis.

In the tread-pattern noise generation, the tread profile is the most important input parameter. To characterize the tread profile, the tread pattern spectral content and air volume velocity spectral content for all the five tires are computed. Then, the tread pattern spectrum and the air volume velocity spectrum are both correlated with the separated tread-pattern noise by visual inspection of the spectra shape.

GENERAL AUDIENCE ABSTRACT

Tire-pavement interaction noise is one of the dominant sources of vehicle noise, and one of the most significant sources of urban noise pollution. One critical generation mechanism of tire-pavement interaction noise is tire tread (the part that is in contact with the ground on the surface of the tire) excitation. This type of noise is called the tread-pattern noise. This study is dedicated to separating the tread-pattern noise from the total tire-pavement interaction noise, which has not been reported in the open literature. The separation of the tread-pattern noise can provide critical criteria for the tread-pattern acoustic design, which is one of the most important factors in the tire tread pattern design. Hence, the acoustic design of the tread pattern can be evaluated directly from the tread-pattern noise measurement, thus improving the design efficiency. In addition, the standalone study on the tread-pattern noise can reveal more fundamental physical underpins how the geometry of the tread can affect the noise generated. This finding has the potential to inspire the design of the tires with higher acoustic performance over the tires being used currently.

ACKNOWLEDGEMENTS

I would like to express my deep gratitude to Dr. Ricardo Burdisso, Professor in Mechanical Engineering Department at Virginia Tech, for his guidance, assistance, and understanding. Dr. Burdisso has been serving as my advisor since the beginning of my graduate study. His guidance allows me to develop fundamental research skills and insight into engineering problems. The current work that has been done would not be possible without his precise intuition and patient support.

I would also like to Dr. Corina Sandu, Professor in Mechanical Engineering at Virginia Tech, for serving as my co-advisor since the second year of the graduate study. Dr. Sandu's expertise in vehicle and tire dynamics is critical to advancement of the project. My sincere admiration and gratitude is also given to Dr. Wing Ng for accepting to be a part of my committee and giving me suggestions as I worked to complete my thesis.

I would also like to thank Mr. Tan Li for his friendship and collaboration on the project. Special appreciation is given to NEXEN TIRE for providing the tires used in the project, and Hankook for digitizing the tires. Kind acknowledgements are extended to the CenTire for the financial support to my study and living expenses in the United States.

Table of contents

List of Figures

List of Tables

1 Introduction

1.1 Background

It is widely acknowledged that tire-pavement interaction noise (TPIN) is one of the main sources of urban noise pollution. It is the dominant noise source when the vehicle speed is higher than 50km/h (Sandberg, 2001). Modern TPIN research started around mid-1970's as engines became less noisy and aerodynamic design of vehicle bodies was optimized (Sandberg et al, 2002). However, due to the complicated nature of noise generation mechanisms (Dare, 2012), it is still difficult to predict the TPIN accurately. Amongst all the mechanisms, the tread pattern is considered to be one critical factor in the TPIN noise generation. According to the literature, approximately 16,000 tread patterns had been used on tires before 2004 (Hanson et al., 2004), and many new tread pattern designs are still being developed each year. Hence, the tread pattern design is critical in the tire industry, which must compromise between noise generation, traction, and safety. Amongst all of the aspects of tread pattern design, tread pattern acoustics is of primary interest for the industry, and there are extensive interests to investigate the noise generated by tread pattern. The effects of the tread patterns on the total TPIN have been investigated both experimentally (Ejsmont et al., 1984) and numerically (Chen et al., 2014). The experimental data showed that different arrangement of tread blocks and tread grooves have significant influence on the air pumping, tire vibration and pipe resonance of the tire, thus changing the emitted tire noise significantly. The numerical data showed that randomization of the arrangement of the tread pattern blocks can be used to distribute the noise component in a broader frequency range. However, limited agreement was shown between the numerical results and experimental data.

The ability to predict and measure the tread-pattern noise will facilitate improvement of tread pattern designs. To be able to study the effects of the tread pattern on noise, the measured tread-pattern noise component must be separated from the noise generated by other sources. However, studies on the noise produced by tread pattern directly have yet to be reported, which necessitates the work to separate the tread-pattern noise in the thesis.

1.2 Literature review

1.2.1 Tread pattern produced noise

The tire tread pattern is the arrangement of ribs, blocks, and grooves on the tire surface. An illustration of a tire with one particular design of tread pattern is shown as Figure 1- 1. The tire tread can be designed with various patterns that have different functionality. A detailed and systematic introduction of tire tread terminology can be found in Appendix-A.

Figure 1- 1: Illustration of the tire.

The tire tread profile can be obtained using a CTWIST machine, as shown in Figure 1- 2. The line scan camera is used in the CTWIST machine to scan the surface of the tire and obtain the 3D tread profile. The scanning device is connected to a computer, which converts the scanned profile into matrix containing the relative height of the tread surface points.

Figure 1- 2: Illustration of the CTWIST machine. (www.starrett.com/metrology/metrology-products/laser-measurement-systems)

The tire tread pattern can generate noise though three mechanisms: (1) tread block impact; (2) air pumping; and (3) pipe resonance in the grooves (Ejsmont et al., 1984). In accordance with the tread-pattern noise production mechanisms, three approaches have been proposed to reduce the tire noise related to tread pattern (Sandberg et al., 2002): (1) pattern randomization to reduce tread impact concentrated in specific frequencies; (2) groove ventilation to reduce air pumping; and (3) modification of the geometry of tread segments (length, width, depth, angle of block/groove) to reduce tread impact in certain frequencies. Simple examples are given in Figure 1- 3. Figure 1- 3 (a) shows the regular tread pattern formed by rectangles without offset. This pattern generates periodic excitation with certain impact frequency. Hence, the regular pattern can lead to high noise levels in certain frequencies if used on vehicles. The pattern can be randomized by having offset of tread blocks between different tread ribs, as shown in Figure 1- 3 (b). In addition, Figure 1- 3 (c) shows the modification of the tread segment geometry by changing the angle between sides of the segments. The geometry modification can also be achieved through alternate, more complex methods.

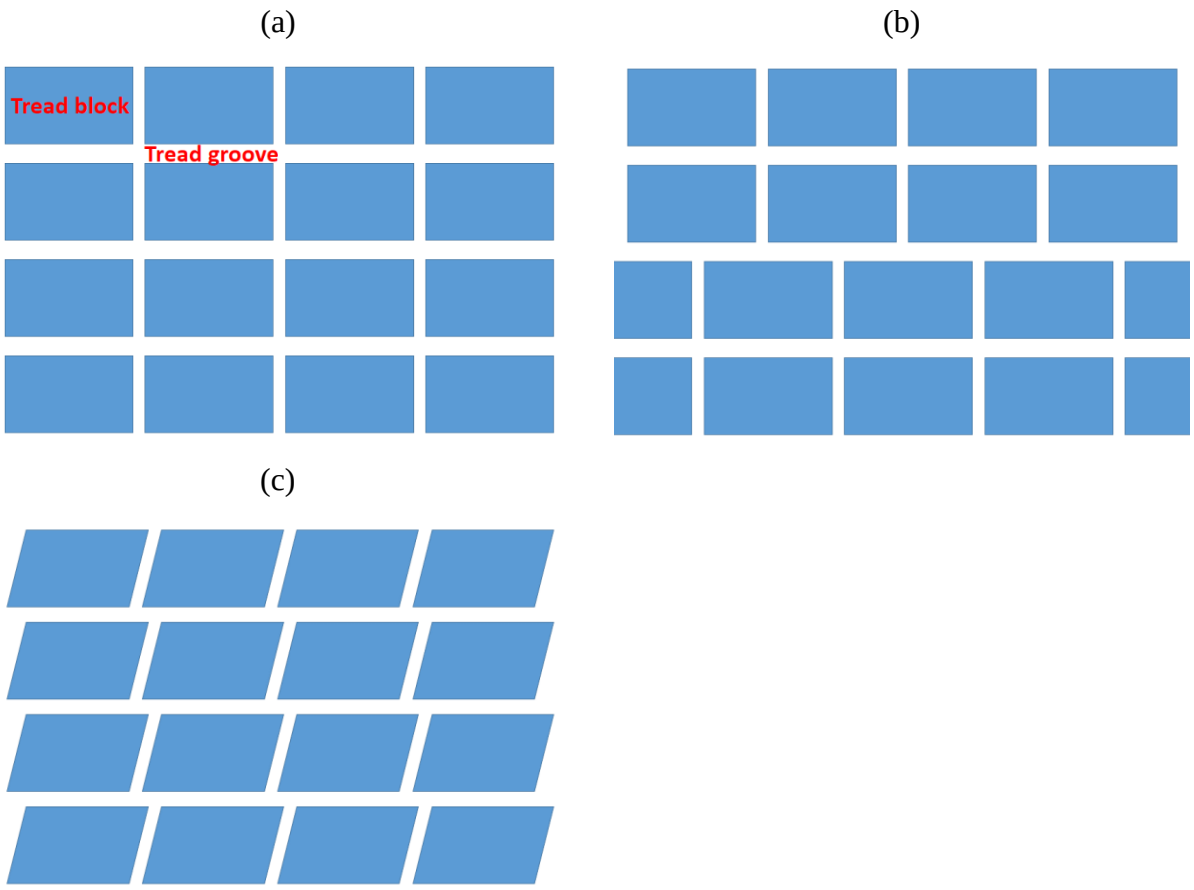

Figure 1- 3: Illustration of simple tread patterns: (a) regular pattern, (b) pattern with offset, and (c) pattern with modified geometry.

One well-known method to model tread-pattern noise, using the relative rotation of the rib, was developed (Parker et al., 1988). First, the tread pattern is digitized into a binary matrix on proper coordinates, in which digit 0 represents tread grooves and digit 1 represents tread blocks. Then, the accurate footprint profile of the leading/trailing edge is defined using an appropriate algorithm. The noise producing function, which defines the noise production of each element in the matrix, is then summed sequentially along the profile over the tread circumference. The summation is converted into analog signals, representing the sound production. Based on this work, other methods were developed for tread-pattern noise prediction. For example, Cao et al. coupled the tread-pattern noise production model with road noise production model, thus enabling simultaneous modeling of the pattern/road interaction noise (Cao et al., 2008). In addition, Liu et al. applied a fuzzy generic arithmetic to the conventional tread-pattern noise

modeling, which significantly improves the efficiency of the optimization of the tread pattern parameters (Liu et al, 2010).

Other methods have also been proposed to model tread-pattern noise. In one method, the tread pattern excitation was modeled by linearly superposing the force produced by each tread element in contact with the road (Kim et al, 2000). Dynamic contact pressure, which is distributed unevenly at the contact patch, was considered in this study. Compared to assuming even pressure distribution at the contact patch, this method improves the accuracy of the pattern noise prediction below 1 kHz. In addition, a human perception model was developed to correlate the tread pattern design with human perception of noise (Bekke et al., 2014). In the proposed model, the tread pattern geometry was treated as an input for noise prediction. Then, tread pattern input was processed to predict the tread-pattern noise in a conventional way proposed in the patent (Parker et al., 1988). The novel part of this study was the further correlation of the tread pattern generated noise with human perception using sound quality metrics.

Liljegren investigated the correlation between tread pattern design and the noise generated by tires (Liljegren, 2008), using the commercial software SPERoN (Statistical Physical Explanation of Rolling Noise). The software has been developed in recent years by researchers at Chalmers University and consulting firms M+P/ Muller-BBM. A hybrid approach containing both a contact model and a statistical model is used in the codes to predict the tire/pavement noise. For the contact model, the inputs are pavement surface profiles and 3-D tread profiles. Then, the contact force is calculated as a function of inputs such as tread profile and tread stiffness. After the contact force is calculated, it is used as the input parameter to the other half of the hybrid model, which is statistical model. For the statistical model, other inputs aside from contact force include airflow resistivity and vehicle speed. The statistical model correlates those input parameters with the measured noise data. In summary, the hybrid model can predict the effects of both tread pattern parameters and environmental factors on tire/pavement noise generation.

Air pumping is also an important noise generation mechanism that is related to the tire tread pattern design. Following the first investigation of air pumping generated noise (Hayden, 1971), most studies identified the source of air pumping as the volume change of tire cavities. Studies

based on monopole (simple sound source) have been made extensively and experiments have shown good agreement with this approach (Ejsmont et al., 1984). Aside from the monopole model, a hybrid technique was developed to predict the air pumping noise (Kim et al., 2006). Gagen argues that the simple monopole model does not reflect the complex air squeezing process (Gagen, 1999). He assumes that the air is not sensitive to local volume changes, which is similar to a damped oscillator, while the monopole theory equates local air movements exactly with the volume changes of the system. Experiments were carried out to validate both the monopole theory and Gagen's model (Eisenblaetter et al., 2010). The results showed that Hayden's model failed for the leading edge signal as the pressure pulse duration was shown to be constant for different tire speeds. The experiment supported Gagen's approach as being preferable to Hayden's model.

1.2.2 Order tracking analysis and synchronous averaging

Order tracking analysis and time synchronous time averaging are both reviewed in this section. Order tracking analysis is a signal processing method to investigate the signals that are related to machine rotations. It is widely used for rotating machinery diagnostics, such as gear boxes and shafts. Rotating machinery produces periodic vibration and acoustic signals that are related to the machine rotation. For tires, the excitation of the tread pattern blocks is periodic with the rotation. Hence, the tread-pattern noise should also be related to the tire rotation. Due to the similarity between the tire and rotating machinery operation, the order tracking analysis can also be used to quantify the periodic signals related to the tire rotation, which is tread-pattern noise. To separate the tread pattern related noise, the synchronous averaging method is used in this thesis. The synchronous time averaging method is a conventional method that is used to cancel the signals that are unrelated to the machine rotation. However, in this study, the averaging algorithm is modified so that the averaging is taken in the order domain rather than in the time domain.

In the order tracking analysis, order power spectrum is used instead of frequency power spectrum (Gade et al., 1995). An order power spectrum gives information about the amplitude and/or the phase of the signal as a function of harmonic (integer multiples) order of the rotation frequency. This means that a harmonic or sub-harmonic order component remains in the same analysis line independent of the speed of the machine. In order to produce phase angle-based

data, the uniform time interval data must be processed to convert the time-based data to phase-angle-based data (Potter, 1990). Prior to Potter's work, numerous hardware components were used to perform the conversion, such as a sensor that monitors the rotation of a shaft and a counter that registers the pulses when the shaft is rotating. Aside from the hardware, one or more tracking analog filters needs to be used to limit the aliasing error associated with the data sampling, and a tracking ratio synthesizer is used to generate sampling pulses synchronously with the rotation of the shaft. Potter et al. proposed a new computed order tracking scheme that reduces the complicated hardware equipment and eliminates the inherent time delay associated with the hardware (Potter et al., 1989; Potter, 1990). Using computed order tracking, the signals are sampled at a constant time increment. Then, the signals are resampled by interpolation to have a constant phase increment. Studies were also carried out to examine the effects of several factors, which are inherent in the computed order tracking method, on the accuracy of computed order tracking (Fyfe et al., 1997). Among these factors are rotational speed, filtering, and the interpolation method. It was found that increasing sampling rates on key-phasor and data signals can improve the accuracy of the order tracking. Additionally, the improvement of key-phasor timing accuracy can also increase the order spectral quality.

The synchronous time averaging method has been implemented extensively to get rid of noise unrelated to the rotation (McFadden, 1985, 1989; Tuma et al., 1999). The signals are sampled at a frequency which is synchronized with the machine rotation. Then the signals are averaged with a sufficient number of rotations. The signals that are asynchronous with the rotation are cancelled out, leaving only the signals that are periodic with the rotation. In the current study, the synchronous averaging are combined with order tracking analysis, which means the averaging is taken in the order domain rather than the time domain.

1.2.3 Signal processing techniques for periodic signals detection and separation

Aside from order tracking analysis and synchronous averaging, there are several other signal processing techniques that can be used to find the periodicity of the signals or to separate signals from different sources. Amongst those techniques, four of them are of interest in the thesis: (1) autocorrelation; (2) frequency domain filter; (3) principal component analysis (PCA); (4) independent component analysis (ICA). The implementation of those techniques does not require

a sensor to keep track of the phase position of the rotating component, which in this case is the tire. Hence, they are investigated in this study to test whether they can separate the periodic signals related to tread pattern excitation. These techniques are reviewed in this section.

The autocorrelation function is computed from the correlation with the signal itself (Priestley, 1982), and it can be used to detect the periodicity in signals as well as de-noise the signal (Parthasarathy, 2006). The basic idea for autocorrelation to detect the periodicity is that the periodic signal is still correlated with itself after time lag T. This can be shown in the following equation,

$$S(t+T) = S(T) \qquad \text{Eqn. 1-1}$$

where S is the periodic signal and T is the period. However, non-periodic signals are not self-correlated when delayed (Martin et al., 2010). Autocorrelation has been applied to de-noise the signals and find periodicity in different backgrounds. Gur et al. implemented autocorrelation to remove background noise and to detect the harmonic components of manatee vocalization (Gur et al., 2007). Xue et al. proposed to use autocorrelation to de-noise the signal as a form of pre-processing of the empirical mode decomposition (Xue et al. 2012). Grosche used the autocorrelation to reveal the musically meaningful periodic information (Grosche et al., 2009).

In rotating machinery diagnostics, a method based on the short time Fourier transform technique has been applied to characterize and to separate different vibration sources (Antone, 2005). This method is fast and efficient for the characterization of three groups of sources: (1) periodic, (2) random stationary, and (3) random non-stationary sources. The technique used a frequency-domain (FD) algorithm (Antoni et al, 2004b) to separate the periodic signals from the non-deterministic signals. First, the algorithm calculates the transfer function between signal segments that are temporally far from each other, as shown in Figure 1- 4. Then, the transfer function for many similar segments pairs are averaged, thus rejecting the signal components that are not correlated. In this study, the FD algorithm will be applied to the simulated TPIN signal, to investigate whether it is capable of separating the periodic components that are related to the tire rotation.

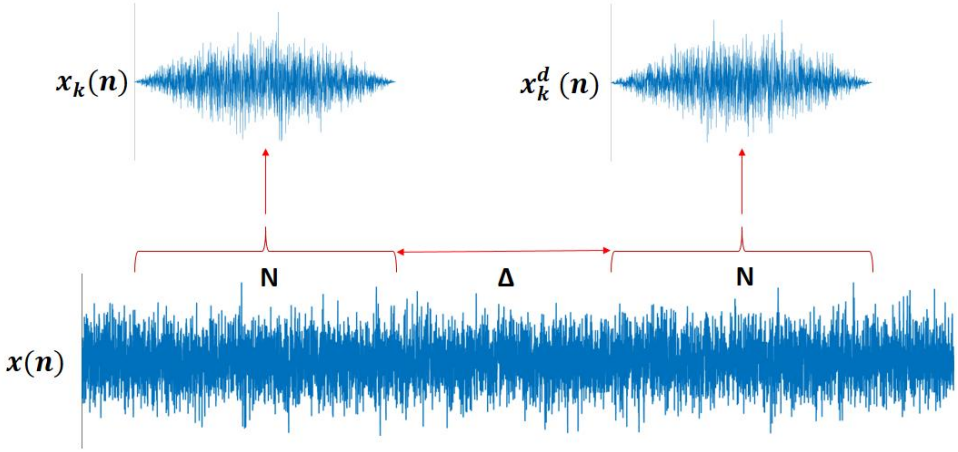

Figure 1- 4: Demonstration of signal segments for FD algorithm.

The blind source separation technique can be applied to separate noise generated by different sources when little information is known about the sound source characteristics (Hyvärinen et al, 2001). Firstly, blind source separation can be achieved through principle component analysis (PCA). The PCA can summarize the data using linear combination of the original observations, to achieve dimension reduction (Tabachnik et al., 2007). In this process, the multivariate signals are re-combined using a coefficient matrix, which is called rotation, to maximize the variance of the data. In this way, the rotated data matrix with maximum variance contains as much data as possible compared to the original observation. The PCA analysis has been applied to analyze noise data measured on different pavement types (Ongel et al., 2008). This study analyzed the effects of various pavements on noise level. However, the application of the PCA to the multi-channel acoustic signals collected by On-Board-Sound-Intensity (OBSI) system has yet to be reported.

Independent component analysis, which is based on PCA, is a more powerful tool for performing blind source separation (Hyvärinen et al, 2001). For ICA, the measure is based on non-Gaussianity and the axes are not independent. A covariance matrix can be obtained using the observed data. After removing the unwanted signals, we can force the inversion of the separation matrices and transform the data back into the original observed space. The ICA algorithm is a very efficient tool to separate signals that are maximally independent and non-Gaussian

(Hyvärinen, 2013). In the ICA algorithms that have already been developed, a fixed-point ICA algorithm was developed to perform fast ICA on the observed data (Hyvärinen et al, 1997). This algorithm can separate several non-Gaussian signals with high efficiency, hence, it is adopted in this study.

1.3 Thesis Objectives

This study aims to separate noise signals that are related to tread pattern from the total TPIN noise, as well as to correlate the tread-pattern noise with the tread pattern parameters. The noise generated by the tread pattern has the characteristic of being periodic with the tire rotation, because the number of tread block impacts for each rotation is certain. This is similar to the noise generated by rotating machinery, such as gears.

The first goal of the study is to separate the tread-pattern noise using the optical signal, which is collected synchronously with the noise data by an optical sensor. The conventional order tracking analysis was used to track the signals related to the tire rotation. In addition to the standard order tracking analysis, signals within each revolution are averaged coherently in the order domain to eliminate the signals that are not related to the tire rotation, thus extracting the signals related to the tread pattern.

The second goal of the current study is to test the effectiveness of several signal processing techniques on separating the tread pattern noise. Four techniques were implemented: (1) autocorrelation analysis; (2) frequency domain filter; (3) principal component analysis; (4) independent component analysis. The results of different algorithms were analyzed and compared with the results obtained by using optical signal. The effectiveness of each method is discussed based on the results obtained.

The third goal is to investigate the correlation between the tread-pattern noise and tread pattern parameters. The tread pattern parameters, which will be detailed in chapter 5, characterize the tread pattern spectral content. The shape of the tread-pattern noise spectra are compared with the tread pattern spectral content to investigate the correlation between the tread pattern characteristics and the tread pattern produced noise.

1.4 Thesis Organization

This thesis is organized in six chapters. Chapter 1 gives the background of the current research, literature review, the goals and organization of the thesis document. Chapter 2 presents the experimental setup, test procedure, data collected, the data processing. In Chapter 3, firstly, the methodology to separate tread-pattern noise using optical signal is described. Then, the results of the measured data processing are presented and discussed. Chapter 4 investigates several signal processing techniques, which are applied to the OBSI noise data. The effectiveness and capability of the methods are discussed and the results are compared with the synchronous averaging method. Chapter 5 firstly calculates the spectra of the tread pattern parameters, which characterizes the tread pattern spectral content. Then, the correlation between the tread pattern parameters and the tread-pattern noise is investigated. Chapter 6 concludes the study and gives suggestions for future work based on the current results.

2 Experiments

The experiments were carried out to collect tire-pavement interaction noise data as well as optical signals. In this chapter, first, the experimental setup is described. Then, testing and data collection procedures are presented. Finally, the test data are processed preliminarily using conventional spectral analysis. The limitation of the spectral analysis to quantify different noise components is discussed.

2.1 Experimental setup

Five different tires were tested. The numbers assigned to each of the five tires tested reflect the fact that they were part of a larger group of tires. The specifications of the tires are shown in Table 2- 1. The tread patterns of the tires are illustrated in Figure 2- 1. All the tires have the same radius, while Tire 20 (SRTT) has different width. The number of blocks shown in Table 2- 1 is the number of tread elements within one tire circumference. The number of plies in the tread band and side-walls is one critical factor indicating tire structures. As the table indicates, some tires have same number of plies. The rubber hardness, which was measured immediately after the test, is nearly the same for all tires.

Table 2- 1: Specifications of the tested tires.

No.	Size	Condition	Number of Blocks	Number of Plies (Tread)	Number of Plies (Sidewall)	Rubber Hardness (Shore A)
12	215/60R16	Winter/Snow	77	4	1	56
15	215/60R16	All season	72	4	1	55
18	215/60R16	All season	65	5	2	65
19	215/60R16	Winter/Snow	60	5	2	64
20	225/60R16	All season	81	3	1	65

Figure 2- 1: Numbering and tread patterns of the tires.

The test was conducted on a section of the U.S. Route 460 near Virginia Tech (between Toms Creek Rd. and North Main St. with a total length of around 1.3 miles). The pavement is a non-porous asphalt pavement, details of which are shown in Figure 2- 2. The test was run on both the eastbound and westbound section. However, due to the similarity of the pavement on the two sections, only results on eastbound section will be discussed in this thesis.

Figure 2- 2: Testing pavement. (source from Google Map)

The OBSI system was used in this study to collect the noise data, as shown in Figure 2- 3. The sampling frequency of the OBSI systems was set to be 25.6 kHz. The OBSI system based on the AASHTO TP-76 standard is widely used for tire-pavement noise measurement. The standard OBSI system has two intensity probes, one at leading edge and another one at the trailing edge of the tire. Each intensity probe contains two microphones. Before each installation, microphones need to be calibrated to maximize sensitivity. Compared to a conventional OBSI system, an optical sensor is additionally incorporated into the modified OBSI system used for the experiments. The specifications of the optical sensor can be found in Appendix-B. One of the microphones (Channel-4) was disconnected, allowing the channel to be used for optical signal collection instead. Hence, only three channels were used to collect tire-pavement noise pressure data in this experiment. The optical sensor was mounted in an aluminum rectangular tube, which was connected to the OBSI system through an L-shape bar and screws. The aluminum tube can prevent the interference of sunlight, thus improving the accuracy of the optical sensing system. The optical sensor radiated an optical beam onto the side wall of a black disk that rotated simultaneously with the tire. Once the optical beam hit the retro-reflective tape, it was reflected back to the optical sensor. The sensor then received the reflected optical beams and converted them into an electric signal. The generation of the optical signal pulse was synchronous with the completion of one tire revolution. Therefore, data from the optical signals can be used to determine the exact start time of each tire revolution. In addition, the signal can be used to accurately estimate speed and acceleration. The vehicle used for testing was a 2012 Chevrolet Impala LT (front wheel drive). As shown in Figure 2- 4, the OBSI system was mounted on the right-rear wheel of the vehicle with a camber angle close to zero (Li et al, 2016 (a); Li et al, 2016 (b)).

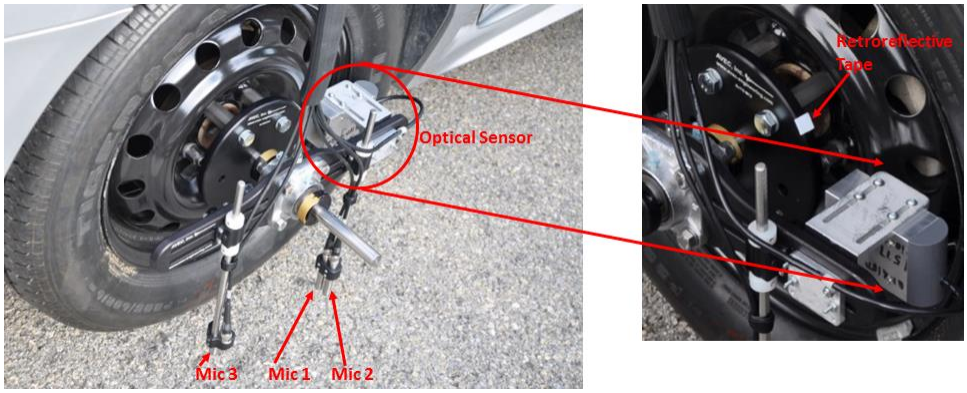

Figure 2- 3: OBSI system with optical sensor.

2.2 Experimental procedures

All the tires were tested between March 7 and March 11, 2016. As is shown in Table 2- 2, the weather during these days was consistently sunny. The stability of the weather condition ensured a consistent pavement condition.

Table 2- 2: Testing conditions.

Tire No.	Test Date	Weather Condition	Inflation Pressure (Pa)	Humidity (%)	Tire Temperature (°F)
Tire 12	Day 4	Sunny	40	70	84
			32	64	88
			26	58	92
Tire 15	Day 3	Sunny	40	92	81
			32	76	88
			26	69	94
Tire 18	Day 2	Sunny	40	71	77
			32	66	86
			26	60	88
Tire 19	Day 4	Sunny	40	81	82
			32	80	87
			26	77	83
Tire 20	Day 1	Sunny	40	50	96
			32	50	104
			26	54	100

Figure 2- 4: OBSI system installed on the car.

All five tires were tested following the same test procedure, which is detailed in this paragraph. The test began at the lab with the installation of the OBSI system, as shown in Figure 2- 4 (Li et al, 2016 (a); Li et al, 2016 (b)). After the assembly of the equipment, the testing vehicle was driven to the selected location at the westbound starting points. The tested tire was inflated to a specified pressure prior to the testing. The environmental factors and tire conditions, which included wind speed, air temperature, pavement temperature, and tire hardness, were recorded using an OBSI log file. Other factors, which include time, humidity, tire temperature, and inflation pressure, were manually recorded in a table, as shown in Table 2- 1. The test of each tire follows the test matrix as shown in Table 2- 3. After testing the inflation pressure and speeds for one tire, the car was driven back to the lab and the OBSI system was uninstalled.

In total, three inflation pressures (26 psi, 32 psi, and 40 psi) were tested. Under each inflation pressure, noise data were collected for five constant speeds (45 mph, 50 mph, 55 mph, 60 mph, and 65 mph). In addition to the constant speed cases, one acceleration case was tested. In the acceleration test, the car was accelerated from 45 mph to 65 mph within about 10 seconds. Then, the speed remained at 65 mph for the rest of the run. For each run, the total time length of the data is 1 to 1.5 minutes, which covers a 1.3 mile pavement length. After each test at a particular inflation pressure, the car was parked at the starting location, and the environmental factors and tires parameters were measured again.

Table 2- 3: Test matrix for one tire.

40 psi			32 psi			26 psi		
Run	Dir.	Speed [mph]	Run	Dir.	Speed [mph]	Run	Dir.	Speed [mph]
1	E	45	1	E	45	1	E	45
2	W	45	2	W	45	2	W	45
3	E	50	3	E	50	3	E	50
4	W	50	4	W	50	4	W	50
5	E	55	5	E	55	5	E	55
6	W	55	6	W	55	6	W	55
7	E	60	7	E	60	7	E	60
8	W	60	8	W	60	8	W	60
9	E	Accel➔65	9	E	Accel➔65	9	E	Accel➔65
10	W	Accel➔65	10	W	Accel➔65	10	W	Accel➔65

2.3 Spectral analysis of the experimental data and its limitation

The total time duration of one test run is 1 to 1.5 minutes. The amount of data in each run is more than enough for data processing. About 10 seconds of data are windowed out of the 1-1.5 minutes of data for each run.

The optical signal is shown in Figure 2- 5. The optical sensor generates a pulse when completing each revolution. As shown in Figure 2- 5 (a), it can be seen that each time the optical sensor received the beam reflected by the retro-reflective tape, nearly constant 5 volts electrical signal was generated from the sensor. As shown in Figure 2- 5 (b), when the reflected optical beam hit the optical sensor, the generated electric signal will oscillate for a short time and then remains at 5 volts for about 0.0015 seconds (1.8505s-1.8520s). The moment at which high voltage oscillation starts is regarded as the time completing one revolution, which is indicated in Figure 2- 5 (b).

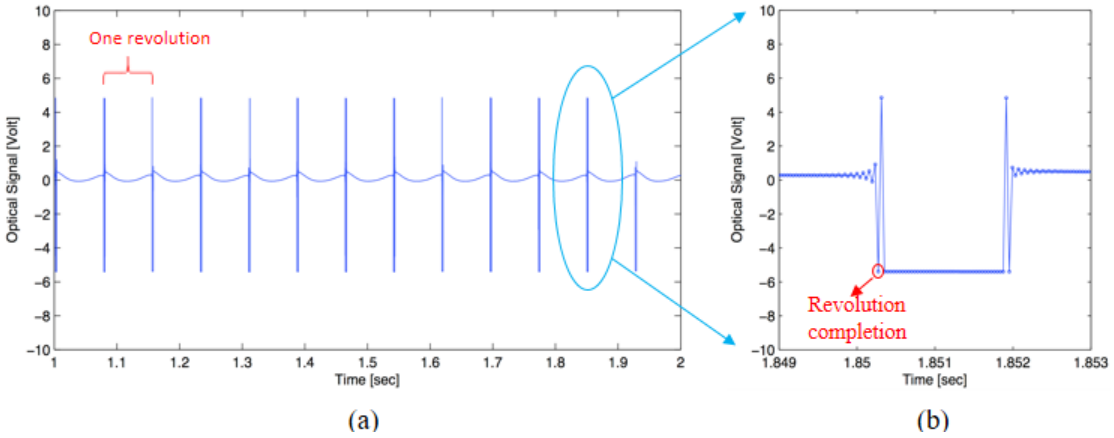

Figure 2- 5: Optical signal demonstration-Tire 20 at 60 mph.

An example of the microphone signals is displayed in Figure 2- 6 (Tire 12 at 60 mph). It shows the sound pressure variation within 1 second. The blue line is the sound pressure signal, and the red lines is the superimposed optical signal. It can be seen that the amplitude of the time history is about 20 Pa for all three microphones, which means that near-field tire noise level is high. The tire noise time history shows obvious periodicity at low frequencies, while the high frequency periodicity is not evident. To clearly investigate the frequency components in the signal, frequency domain analysis is utilized.

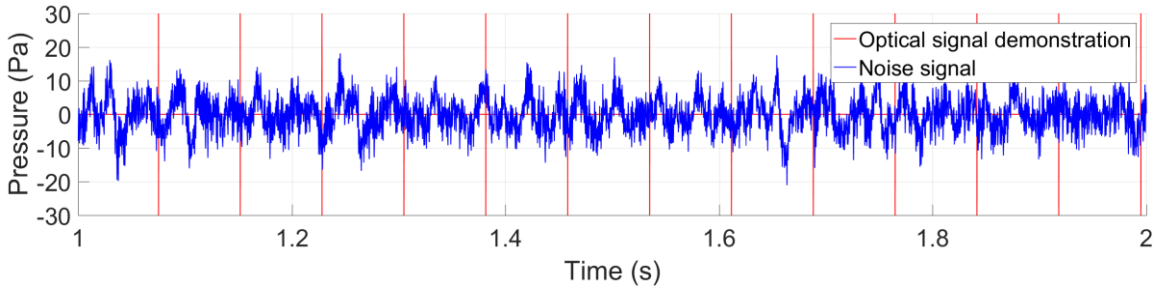

(a) Mic-1

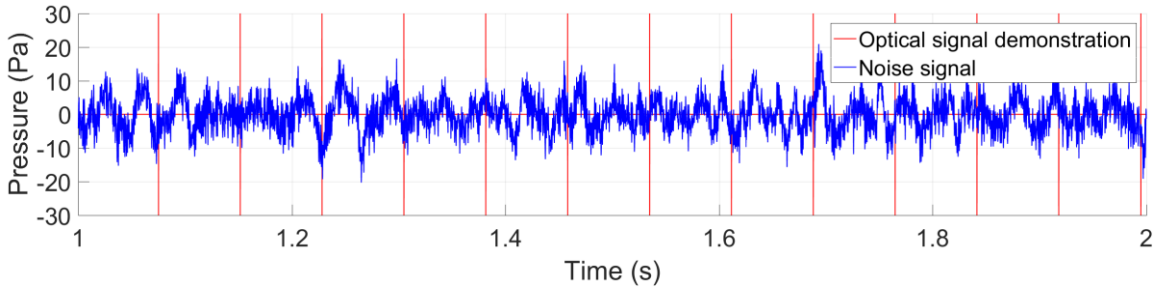

(b) Mic-2

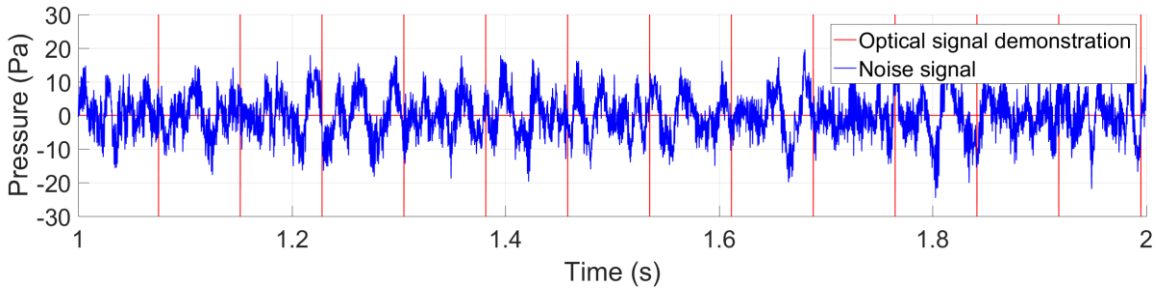

(c) Mic-3

Figure 2- 6: Time history of microphone signals and optical signal-Tire 12 at 60 mph.

The spectra for the three microphones signals for Tire 12 at 60mph are shown in Figure 2- 7. It can be seen that Mic-1 and Mic-2 have very similar spectral content, due to the close spacing of the two microphones. Hence, the data from Mic-1 will be chosen to represent the leading edge noise. The trailing edge noise, which is recorded by Mic-3, shows different frequency spectral shape compared to leading edge noise. Hence, the trailing and leading edge noise will be both analyzed in this thesis. It can be observed that there is high amplitude noise content below 300 Hz, which is induced by wind passing by the microphone. This phenomenon is unable to be avoided even when the microphones are covered by a wind screen. However, the noise

components below 300 Hz is not of our interest in this study, because A-weighting makes this part of the spectrum insignificant in the noise spectrum.

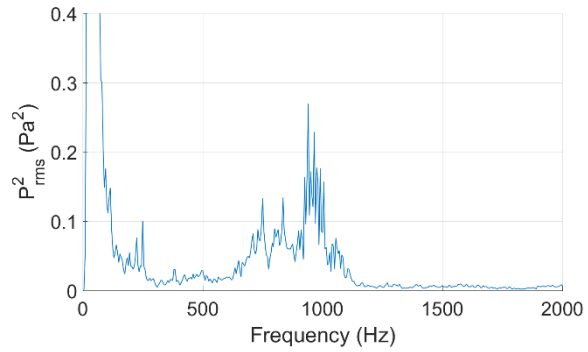

(a) Mic-1

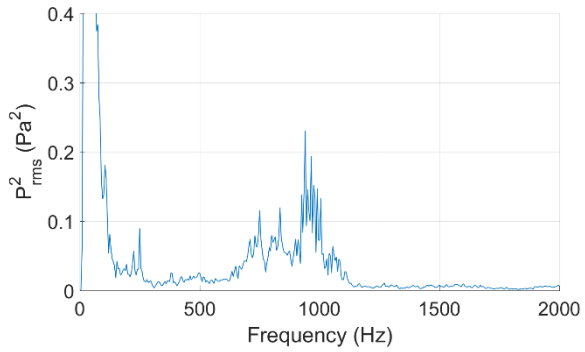

(b) Mic-2

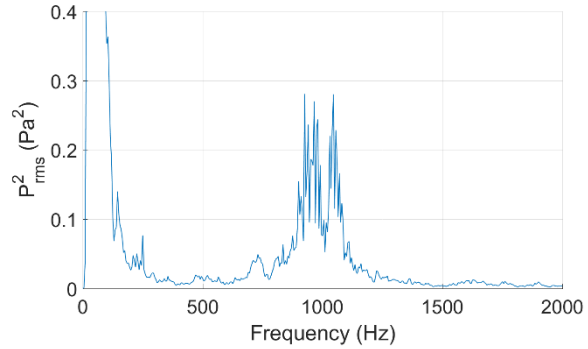

(c) Mic-3

Figure 2- 7: Frequency power spectra of microphone signals-Tire 12 at 60 mph. (Frequency resolution = 5Hz)

The spectra at different speeds for Tire 12 are shown in Figure 2- 8. It can be observed that there is one noise component that is positively correlated with the vehicle speed. The frequency of the tread pattern related noise is supposed to change with speed due to the change of fundamental tread pattern impact frequency. Hence, it is inferred that the spectra of Tire 12 shows a significant amount of tread-pattern noise related content.

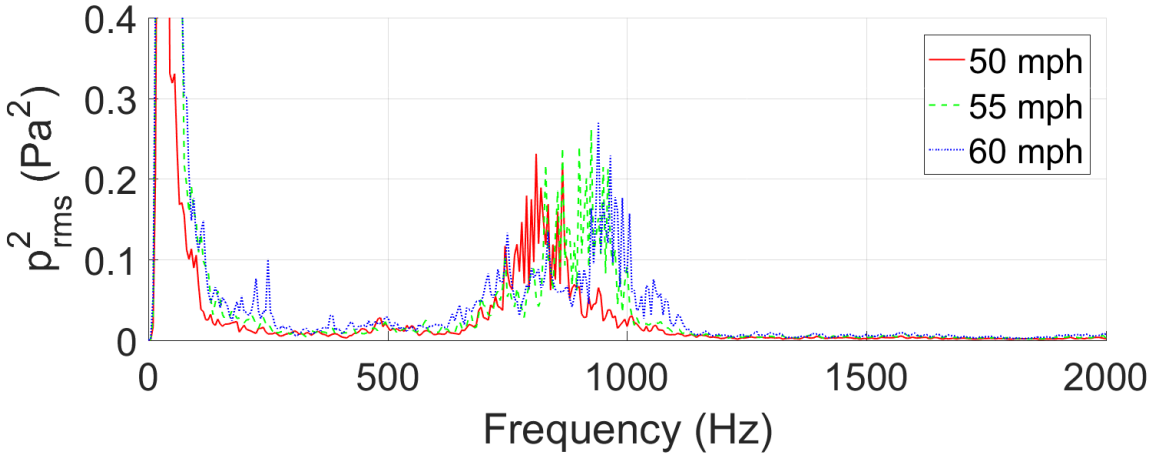

(a) Leading edge

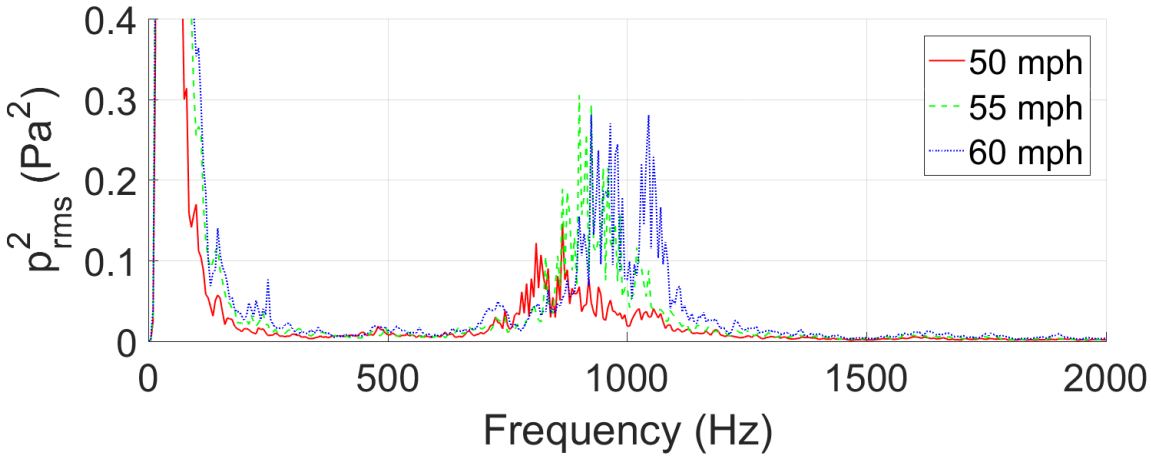

(b) Trailing edge

Figure 2- 8: Comparison of frequency power spectra for different speeds-Tire 12. (Frequency resolution = 5 Hz)

To obtain better insight into the different noise components for Tire 12, the spectrogram from the acceleration case is calculated and shown in Figure 2- 9. It is notable that there are two components in the noise spectra. Component 1 changes with speed, which is related to the tread pattern excitation. The other component stays at the same frequency regardless of the speed change. To investigate the effects of tread pattern on noise generation, the order domain synchronous averaging is applied to the total TPIN to separate the component 1 from noise caused by other mechanisms in Chapter 3.

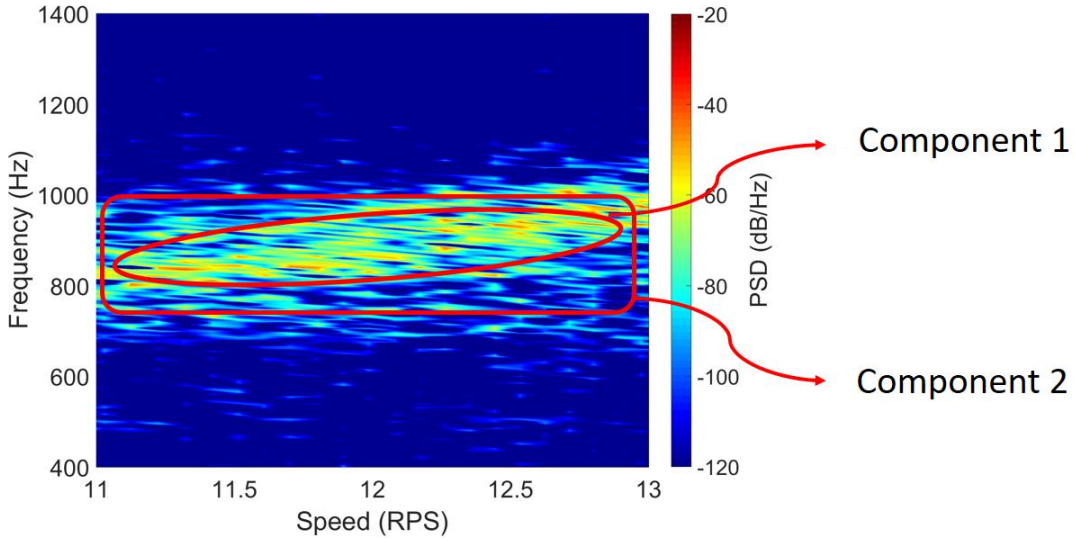

Figure 2- 9: Spectrogram for acceleration at leading edge-Tire 12.

3 Tread-pattern noise separation using optical signal

In this chapter, the separation of tread-pattern noise using an optical sensor is presented. The optical sensor provides a once per revolution signal, which can be used for order tracking analysis and synchronous averaging. First, the detailed methodology of the tread-pattern noise separation is presented. Then, the validation of this method is shown through a simulated case, in which a tread-pattern simulated signal is successfully separated from other noise sources. The experimental separation of the tread pattern related noise for both constant speed and acceleration cases are shown. The effect of the numbers of averages on the tread-pattern noise is investigated for the constant speed case (60 mph). The separation results for different speeds (50/55/60 mph) are compared and the 60 mph cases are investigated in detail. Additionally, the effect of the number of averages is also investigated for the acceleration case. The tread-pattern noise separation on different pavements was also performed for further validation of the method. Finally, one special case with unusual tone in the noise spectra was investigated, and it was verified that the tone was not related to the tread pattern.

3.1 Separation Methodology

Order domain synchronous averaging is used to separate the tread-pattern noise in this study. Compared to time synchronous averaging, the averaging is taken using the Fourier complex values after the time signal is resampled and transformed into the order domain. Figure 3- 1 shows the procedures of the tread-pattern noise separation algorithm. To make the procedures more intuitive, plots of one example (Tire 12 at 60 mph) are shown in Figure 3- 2.

First, the time signal is resampled to have the same number of data points per revolution, independent of the actual time length, as shown in Figure 3- 2 (b) and (c). The resampled data points should have constant phase increment rather than time increment. To obtain the phase of each sampling point, the time integral of the rotational speed is used,

$$\phi(\mathrm{t}) = \int_0^t \frac{rpm(\tau)}{60} d\tau \qquad \text{Eqn. (3-1)}$$

where ϕ is the phase of each sampling point.

Then, in order to avoid the aliasing of the high-frequency components, the signal is filtered using a low-pass filter. After the low-pass filtering, the resampling is performed using the optical signal. The optical signal provides the time T_k, which is the time to complete k^{th} revolution. Using the calculated phase at each sampling point and the once per revolution time T_k, the low-pass filtered signal is linearly interpolated onto a uniform grid in the phase domain,

$$p_n^{t\_r} = \frac{\phi_n^{t\_r} - \phi_{n-1}^t}{\phi_n^t - \phi_{n-1}^t}(p_n^t - p_{n-1}^t) + p_{n-1}^t \qquad \text{Eqn. (3-2)}$$

where ϕ_n^t is the phase of the n^{th} point of the non-resampled total noise signal, p_n^t is the n^{th} point of the non-resampled total noise signal, $p_n^{t\_r}$ is the n^{th} point of the resampled total noise signal. As it is shown in Figure 3- 2 (b) and (c), the total noise signal is resampled within each revolution. The resampled signal has a constant sampling frequency revolution, such as 1800 points/rev for Tire 12 at 60 mph (the original sampling frequency in this study is 25.6 kHz).

Then, for each revolution, the discrete Fourier transform (DFT) is applied to the resampled total noise signal, in order to convert the signal from the time domain into the order domain.

$$P_{k-a}^{t} = \sum_{n=0}^{N} p_{k-n}^{t\_r} \cdot e^{-2\pi ian/N} \qquad \text{Eqn. (3-3)}$$

where k represents the k[th] revolution, N is the total number of resampled points in one revolution, $p_{k-n}^{t\_r}$ is the n[th] point of the resampled total signal time history the k[th] revolution, P_{k-a}^{t} is a[th] the Fourier transform value of the resampled total signal for the k[th] revolution. The illustration of the order spectrum of the signal within each revolution window is shown in Figure 3- 2 (d).

After order domain complex Fourier transform values are calculated for all the revolutions, they are averaged coherently

$$\bar{P_a} = \frac{1}{M} \sum_{k}^{M} P_{k-a}^{t} \qquad \text{Eqn. (3-1)}$$

where M is the total number of revolutions, and k represents the k[th] revolution, $\bar{P_a}$ is the a[th] averaged order domain Fourier transform value. After the averaging, the Fourier complex value of the signals that are not related to the rotation of the tire will be rejected and have a 0-mean value. With enough number of revolutions averaged, only the periodic signals that are related to the tire rotation will be preserved. For example, as shown in Figure 3- 2 (e), it can be observed that most signals between 70-80 orders, which are of our interest, are preserved after averaging for Tire 12 at 60 mph.

The tread-pattern signals are periodic with the tire rotation, which are assumed to be the same for all the revolutions. Hence, the DFT values for all the revolutions are the equal to the averaged values,

$$P_{k-a}^{tr} = \bar{P}_a \qquad \text{Eqn. (3-4)}$$

where k represents k[th] revolution, *tr* is abbreviation for tread-pattern noise signal, P_{k-a}^{tr} is the a[th] Fourier transformed value for the tread-pattern signal in the k[th] revolution.

Then, the time history of the tread-pattern signals for each revolution can be computed using the inverse DFT of order domain complex values,

$$p_{k-n}^{tr} = \frac{1}{N}\sum_{a=0}^{N} P_{k-a}^{tr} \cdot e^{2\pi i a n/N} \qquad \text{Eqn. (3-5)}$$

where N is the total number of points in each revolution, p_{k-n}^{tr} is the n[th] point of the tread-pattern noise time signal for the k[th] revolution. The tread-pattern signal is repeated for all the revolutions, so the tread-pattern noise time signal can be constructed by putting the signal in each revolution together sequentially (demonstrated as Figure 3- 2 (e) and (f)). The non-tread pattern signals, which are not related to tread pattern excitation, can be obtained by the linear subtraction between the the total noise signal and tread-pattern signal, as shown in Eqn. (3-6). The non-tread-pattern signal is illustrated as Figure 3- 2 (g).

$$p^{n-tr} = p^{t} - p^{tr} \qquad \text{Eqn. (3-6)}$$

where p^{n-tr} is the non-tread-pattern noise signal. Following the methodology, the time history and power spectra of total noise signals, tread-pattern noise signals, and non-tread-pattern noise signals can be obtained. In the next section, the validation of the method is shown. In this case, only the tread-pattern simulated signal is separated. In Chapter 5, the tread-pattern noise spectra are compared with the tread pattern parameters. The results provide more support to the effectiveness of the methodology.

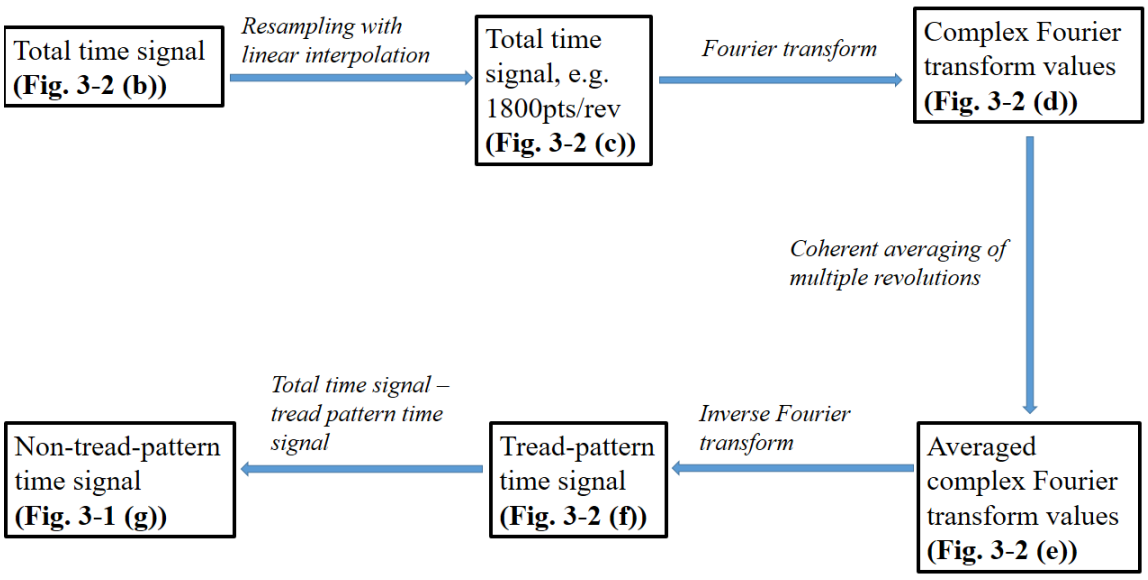

Figure 3- 1: Flow chart of the tread-pattern and non-tread-pattern noise signal separation methodology.

.

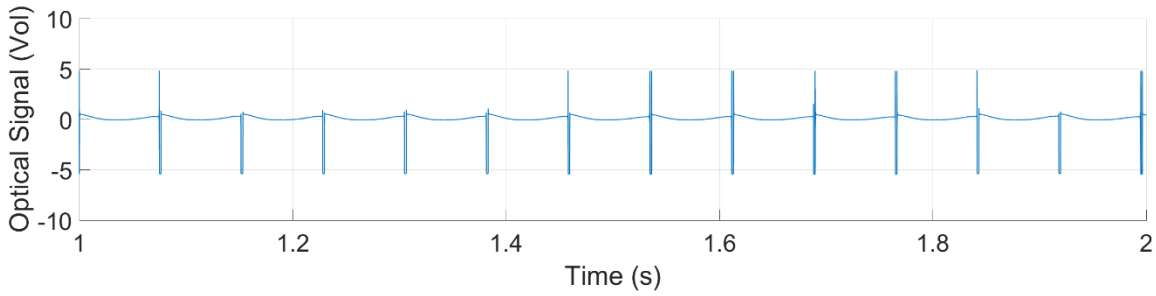

(a) Optical sensor signal example

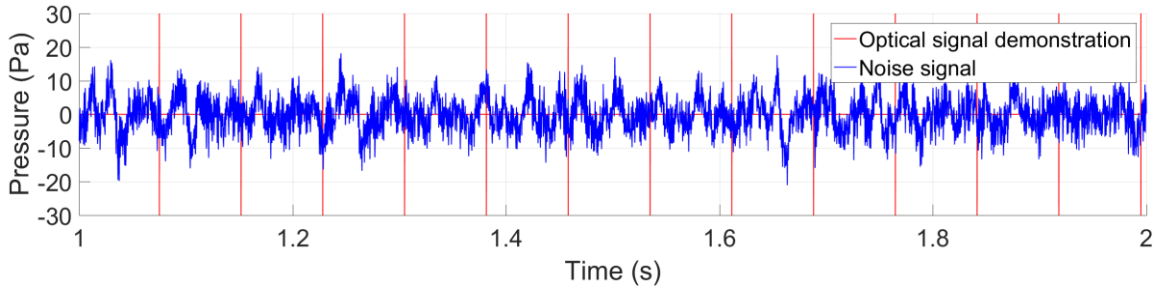

(b) Total microphone time signal (each window representing one tire revolution)

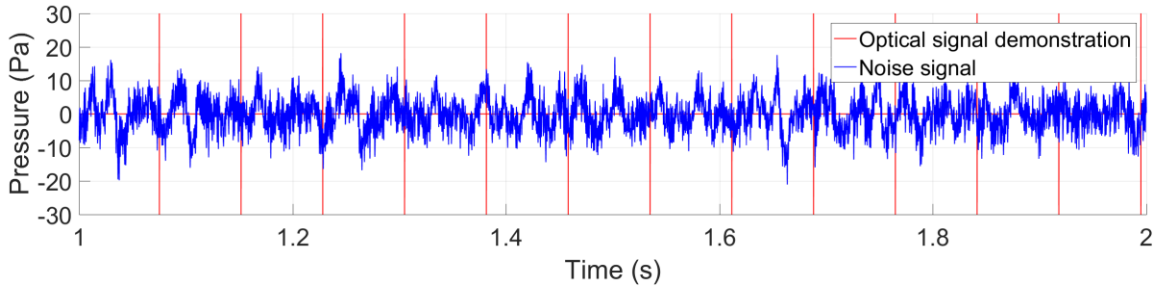

(c) Resampled total microphone time signal

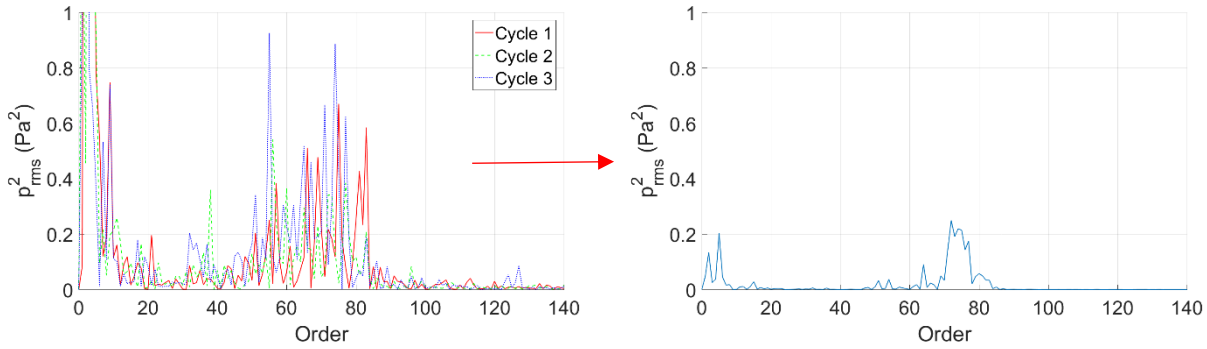

(d) Order power spectra of microphone signals (3 cycles)

(e) Averaged order power spectra

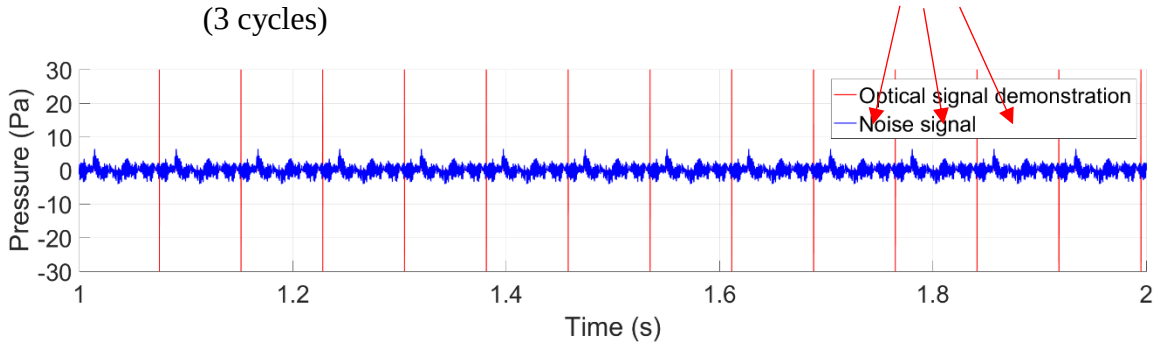

(f) Tread-pattern noise signal

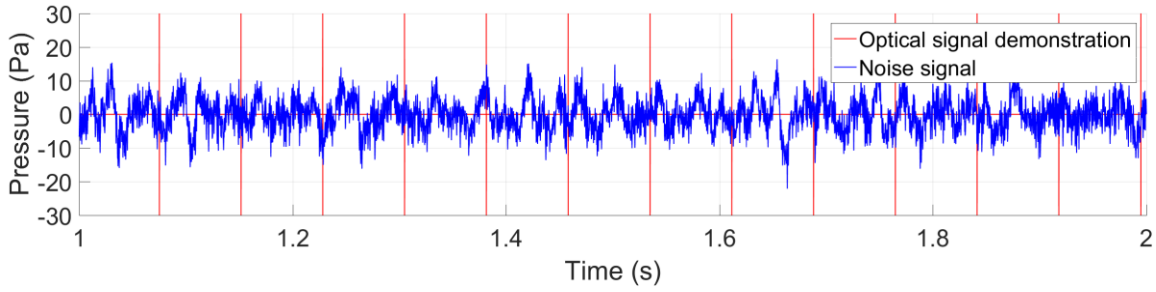

(g) Non-tread-pattern noise signal

Figure 3- 2: Illustration of separation of tread-pattern and non-tread-pattern noise signal: Tire 12 for 60 mph.

3.2 Validation of the methodology with simulated signal

The validation of the method is first tested by using a synthesized signal. Three signals are combined: (1) a 200Hz constant amplitude sine wave; (2) a 80 order sine wave, which contains 80 periods per tire revolution; and (3) white noise. The goal of the method is to separate the signals that are related to the tire (tires mentioned in Chapter 2) rotation. Hence, in the synthesized signal, the signal components that have constant order (80/rev) should be separated. The 80 order signal is generated using the optical signal as reference. For each revolution, 80 sine waves are fit into the window. In total, approximately 8 seconds of signals are generated, the details of each signal component are shown in Table 3- 1.

Table 3- 1: Details of the simulating signal components

Signal component	Frequency	Sampling Frequency	Time length
80 order sine wave	80 per revolution	25600 Hz	7.79s (100 rev)
Sine wave	200 Hz	25600 Hz	7.79s (100 rev)
White noise	\	25600 Hz	7.79s (100 rev)

Figure 3- 3 (a) is the time history of the synthesized signal. Figure 3- 3 (b) and (c) show the time history of the separated 80 order signal and the mixture of the other two signals, respectively. The time history shown in Figure 3- 3 (a) and (c) appears to be similar, because the periodic signal is buried in the white noise. Figure 3- 3 (b) appears to be more periodic. To gain more insight into the physical properties of the signal, the power spectra of the signals are calculated. As shown in Figure 3- 4, the addition of the spectrum in (b) and (c) is equal to (a), which indicates that the 80 order signal is successfully separated from the 200Hz sine wave and white noise. This validates that the method is capable of separating the signal related to the tire rotation.

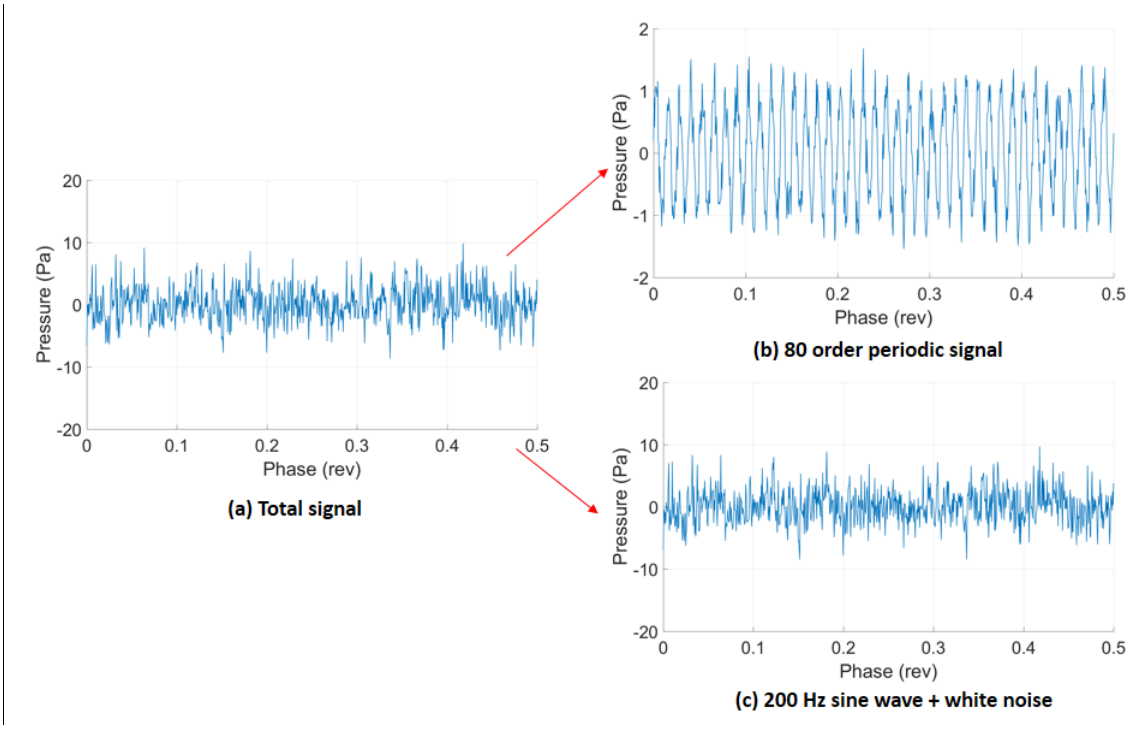

Figure 3- 3: Phase history of the simulating signals.

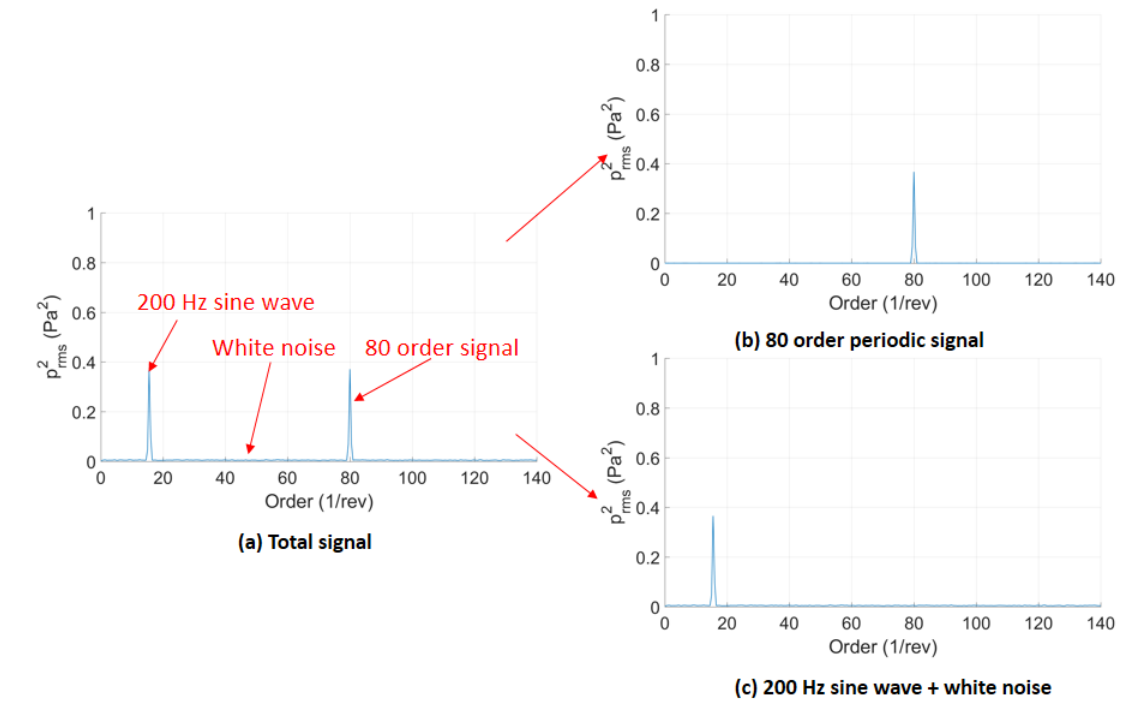

Figure 3- 4: Order spectra of the simulating signals.

3.3 Signal separation results for constant speed

3.3.1 Effects of number of averages on the tread-pattern noise

One critical factor that has significant influence on the tread-pattern noise separation is the number of revolutions used for averaging when processing the signals. Hence, in this section, different numbers of revolution are used to test its effects on the tread-pattern noise. Specifically, three numbers of revolutions (60/80/100) are used. One tire with significant tread-pattern noise (Tire 19) and one tire with only weak tread pattern contribution (Tire 20) are chosen for analysis here. The 60 mph and 32 psi case is analyzed.

As shown in Figure 3- 5, for Tire 19, the separated noise is almost the same for the three numbers of averaged revolutions, at both leading and trailing edge. This means that 60 revolutions are enough to get rid of the signals that are not related to the tire rotation. For Tire 20, which displays much less pattern-produced noise, it can also be observed from Figure 3- 6 that the three number of averaged revolutions do not show significant influence on the separated tread-pattern noise spectra. According to the results of both tires (Tire 19/Tire 20), for the constant speed cases, 60 revolutions are chosen to achieve the balance between computational cost and separation effectiveness.

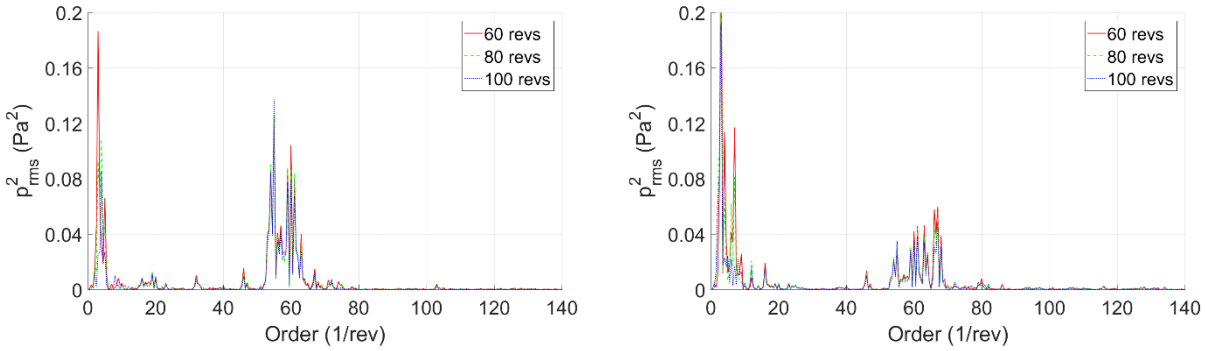

(a) Leading edge (b) Trailing edge

Figure 3- 5: Comparison of the tread pattern noise with different number of averages-Tire 19 @ 60 mph. (order resolution = 0.5)

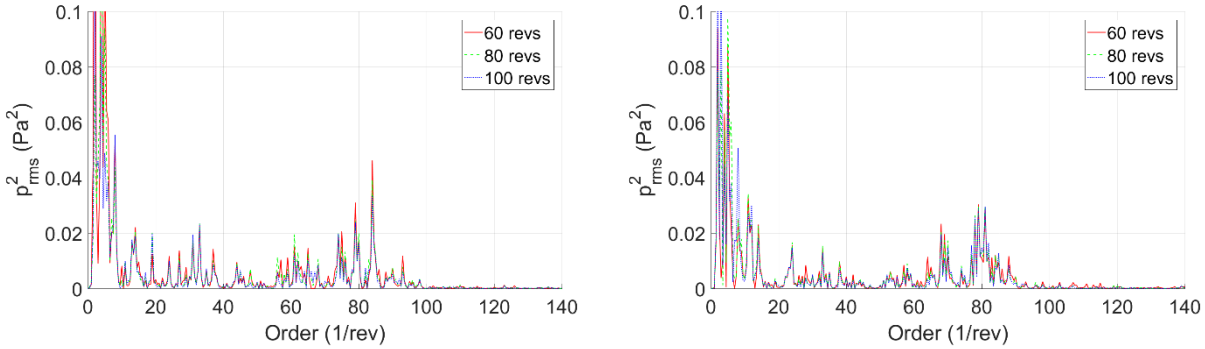

(a) Leading edge (b) Trailing edge

Figure 3- 6: Comparison of the tread pattern noise with different number of averages-Tire 20 @ 60 mph. (order resolution = 0.5)

3.3.2 Tread-pattern noise separation results

The effects of the speeds on the tread-pattern noise are investigated for Tire 12 and Tire 20. The number of averaged revolutions is 60 for all the speeds and tires. Tire 12 has significant tread pattern produced noise. It can be seen from Figure 3- 7 (a) that for the leading edge, the speed variation changes the order distribution by a small amount. From Figure 3- 7 (b), it can be seen that the increase in speed enhances the tread-pattern noise level significantly at the trailing edge.

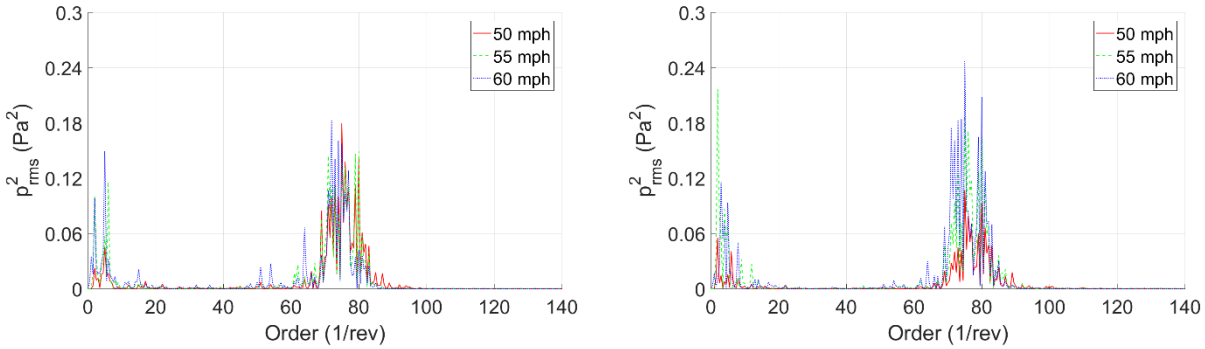

(a) Leading edge (b) Trailing edge

Figure 3- 7: Comparison of the separated signals at different speed-Tire 12 @ 60 mph. (order resolution = 0.5)

For Tire 20, the tread pattern does not produce much noise. It can be seen from Figure 3- 8 that, compared to Tire 12, the shape of the spectrum of the tread-pattern noise of Tire 20 is more sensitive to the speed change, especially at the leading edge. Specifically, the tread-pattern noise for different speeds at the leading edge does not concentrate around a certain order. At the trailing edge, there are significant signals around 80 orders for different speeds, and the speed does not have significant effects on the shape of the tread-pattern noise spectra.

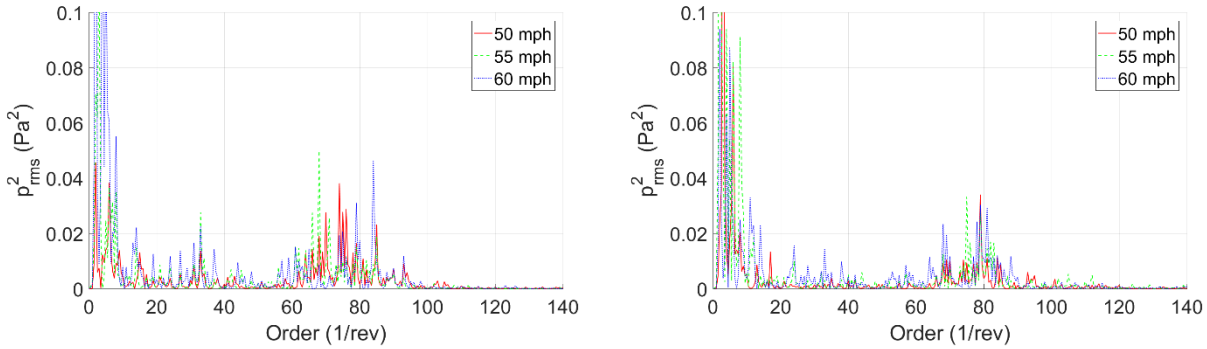

(a) Leading edge (b) Trailing edge

Figure 3- 8: Comparison of the separated signals at different speed-Tire 20 @ 60 mph. (order resolution = 0.5)

From the results for Tire 12 and Tire 20, it can be seen that for the tire with significant tread pattern noise contribution, the increased speed will enhance the noise level significantly but does not change the order distribution. While for the tire that does not have significant tread-pattern noise, the trend is not very clear with the speed change. The tread-pattern noise is closely related to the arrangement of the tread blocks. Hence, in the later results analysis, the correlation between the tread-pattern noise components and the number of blocks in one circumference will be investigated.

After investigating the effects of speeds on the tread-pattern noise in constant speed cases, the separation results for Tire 12 and Tire 20 at 60 mph/ 32 psi are shown. The results of other tires can be found in Appendix-E. The order spectra of the total TPIN noise, the tread-pattern noise, and non-pattern noise are plotted together in the same graph for comparison. Thus, it is necessary to obtain information detailing to what extent the tread pattern noise can be separated from the total TPIN. For all the cases analyzed here, 60 revolutions are used for the order domain averaging. First, one demonstration of the signal time history for Tire 20 is presented in Figure 3-9. It can be seen from the amplitude of the time history that the tread pattern noise of Tire 20 is much smaller than the total noise, which can also be observed in the order spectra plot.

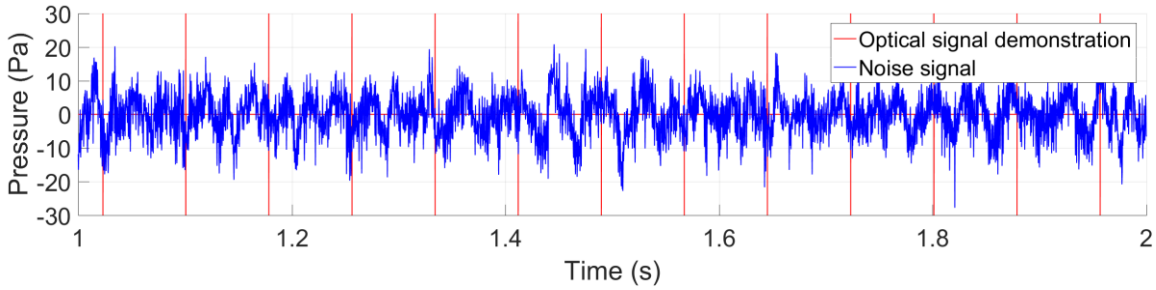

(a) Total noise

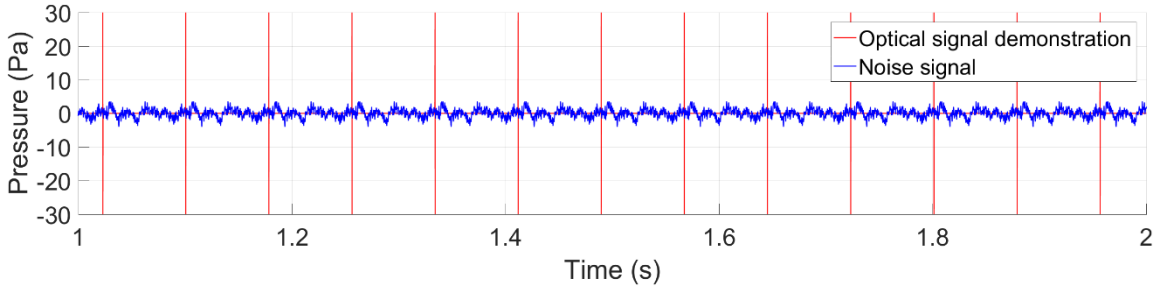

(b) Tread-pattern noise

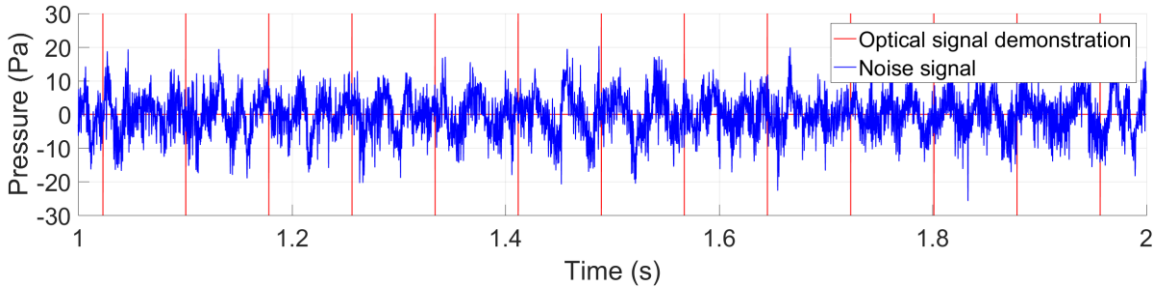

(c) Non-tread-pattern noise

Figure 3- 9: Time history of the signals of Tire 20 at 60 mph-leading edge.

Tire 20 has a small tread-pattern noise component, as shown as in Figure 3- 10. For Tire 20, the tread-pattern noise can be observed around 81 order, which is the fundamental impact frequency per revolution. However, it can be observed that the non-pattern noise is almost the same as the total TPIN noise at both leading and trailing edge. This indicates that the tread pattern does not contribute a significant amount of noise for Tire 20. Additionally, the low level of pattern-produced noise partly explains the phenomena that the pattern noise spectra does not show a clear trend with speed change. Hence, for Tire 20, it can be concluded that most of the noise is generated from other mechanisms, which are not directly related to the tread-pattern excitation.

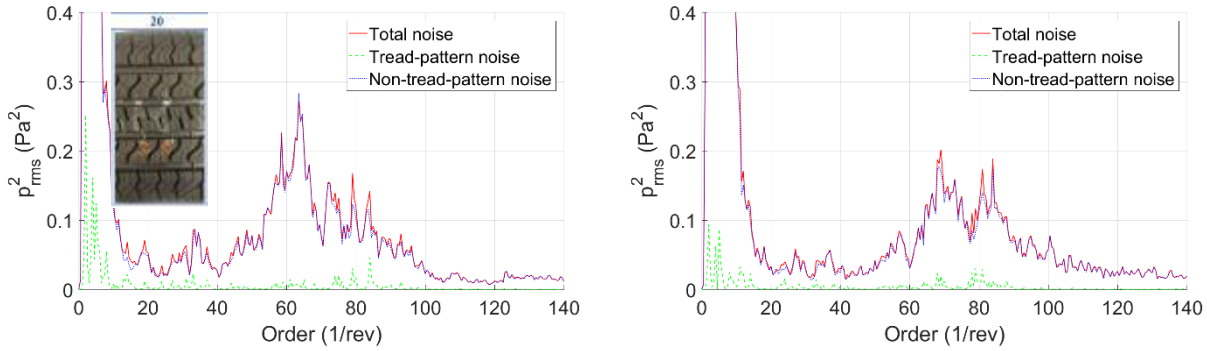

(a) Leading edge (b) Trailing edge

Figure 3- 10: Tire noise separation for Tire 20 at 60 mph (order resolution: 0.5).

Contrast to Tire 20, Tire 12 has high level of tread-pattern noise. As shown in Figure 3- 11, there is significant noise around the fundamental tread impact frequency. In addition, the non-pattern related noise spectra show clear differences between the total TPIN for these two tires. This indicates that the type of tire used for Tire 12 is inclined to generate more periodic impact or more air pumping. It is clear that the Tire 12 shows a more symmetric pattern which is not well randomized for better traction in the snow. This provides one explanation to the high tread-pattern noise that Tire 12 makes.

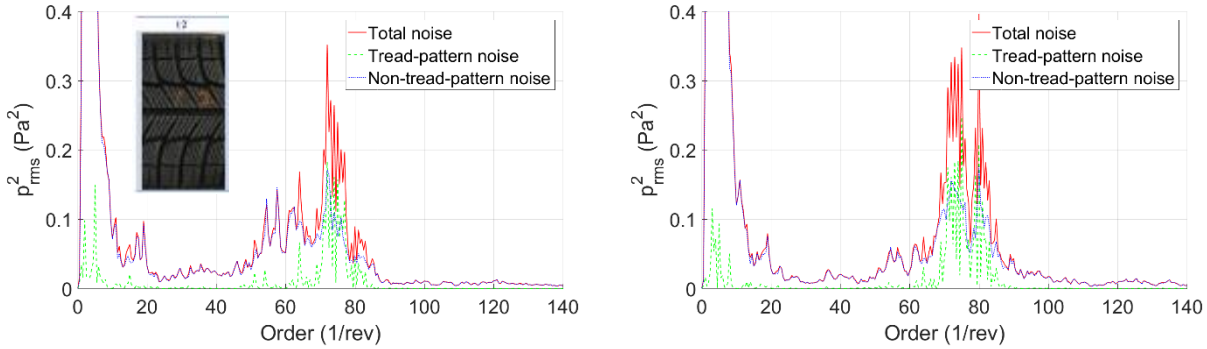

(a) Leading edge (b) Trailing edge

Figure 3- 11: Tire noise separation for Tire 12 at 60 mph (order resolution: 0.5).

3.3.3 Comparison of the non-tread-pattern noise of different tires on the same pavement

The five tires were all tested on the same pavement, which is believed to be the largest factor that determines the TPIN. Hence, after the separation, it is hypothesized that the non-tread-pattern noise signal spectra are similar to each other. To test the hypothesis, the results before and after separation are both shown for comparison. As shown in Figure 3- 12, at the leading edge, the order distribution of the spectra for the five tires match much better after the separation of tread-pattern noise. As shown in Figure 3- 13, at the trailing edge, the spectra also match more closely after the separation of the tread-pattern noise. However, there are still some discrepancies for the non-tread-pattern noise of the five tires. The difference between various tires could result from different environmental conditions and tire properties such as rubber hardness and tire stiffness.

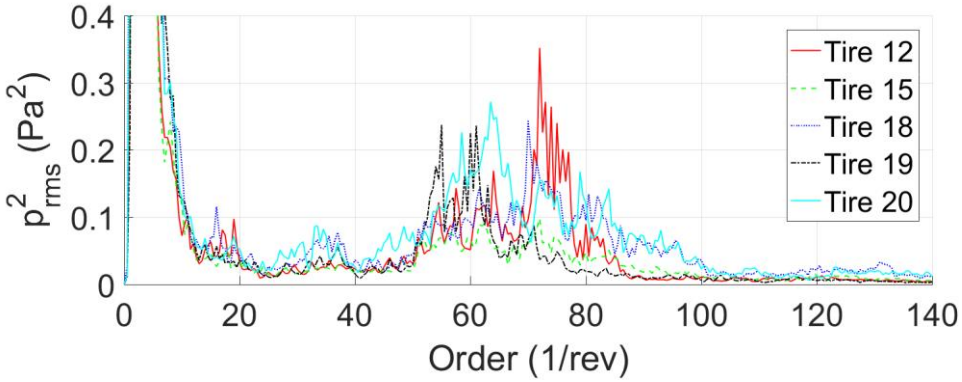

(a) Total noise

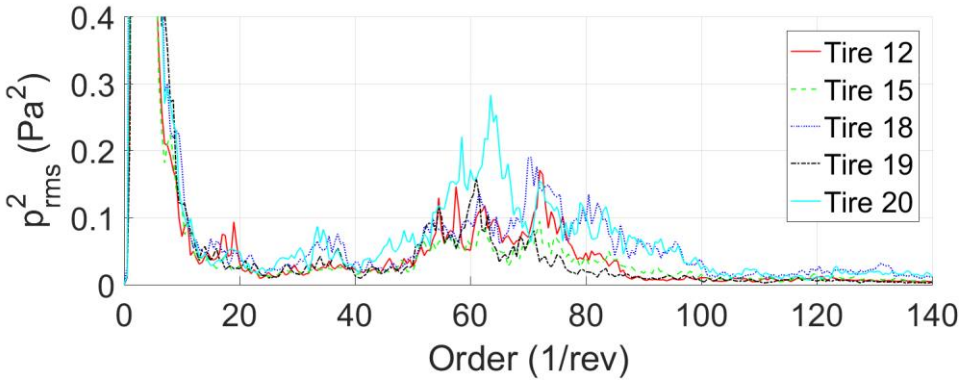

(b) Non-tread-pattern noise

Figure 3- 12: Comparison of noise spectrum of all five tires at 60 mph-leading edge (order resolution: 0.5).

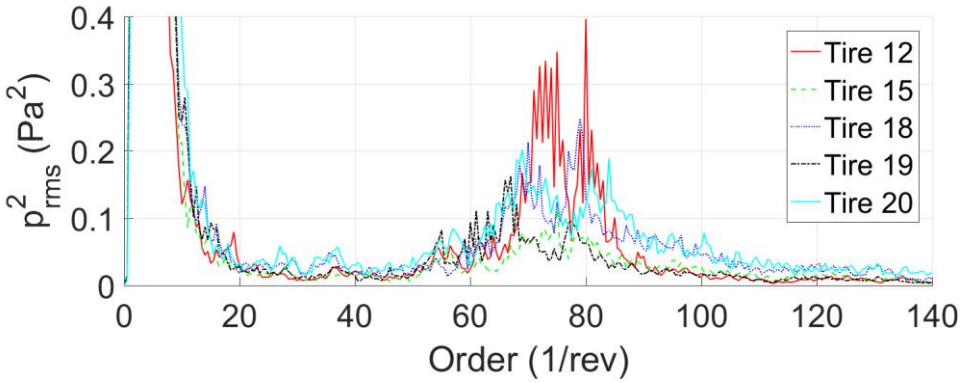

(a) Total noise

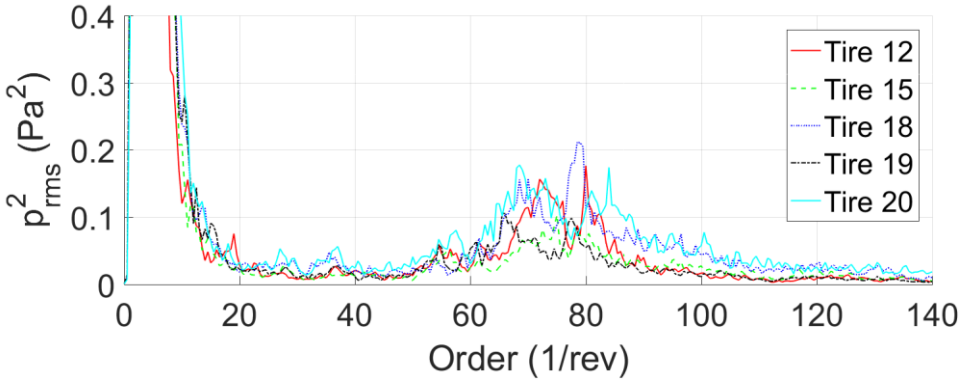

(b) Non-tread-pattern noise

Figure 3- 13: Comparison of noise spectrum of all five tires at 60 mph-trailing edge (order resolution: 0.5).

3.3.4 Comparison of the tread-pattern noise of the same tire on different pavement

The last section revealed that, for different tire types on the same pavement, the non-tread-pattern noise appears to be similar. In turn, the same tire on different types of pavement should display similar tread-pattern noise. To verify the hypothesis and test the effectiveness of the separation methodology, the noise spectra for the same tire/speed on different pavements are compared with each other.

One set of data on a section of newly-paved road that is smoother was collected for Tire 12 at 60 mph and 26 psi. Due to the limit of the time duration of the data, 35 revolutions are used for the average in this thesis. Figure 3- 14 shows the comparison of the tread-pattern noise on different pavement. As shown in Figure 3- 14, the tread-pattern noise spectra for the same tire on different pavements have similar shapes. This indicates that the tread-pattern noise separation is not influenced by differences in pavement type. For further validation, the non-tread-pattern noise for Tire 12 on different pavements is also compared, as shown in Figure 3- 15. However, it can be observed that there is a large area of mismatch from 55 to 65 order, e.g. the "new pavement" is significantly quieter than the older pavement.

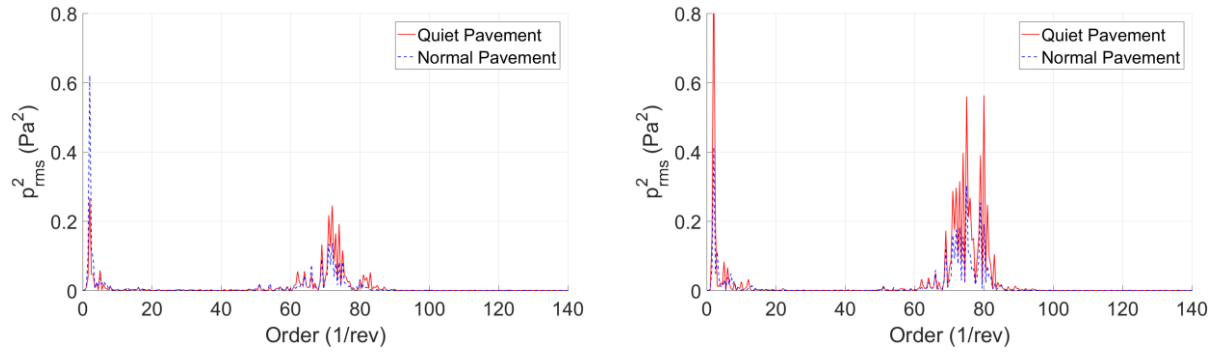

(a) Leading edge (b) Trailing edge

Figure 3- 14: Comparison of the tread pattern noise on different pavement for Tire 12 at 60 mph (order resolution: 0.5).

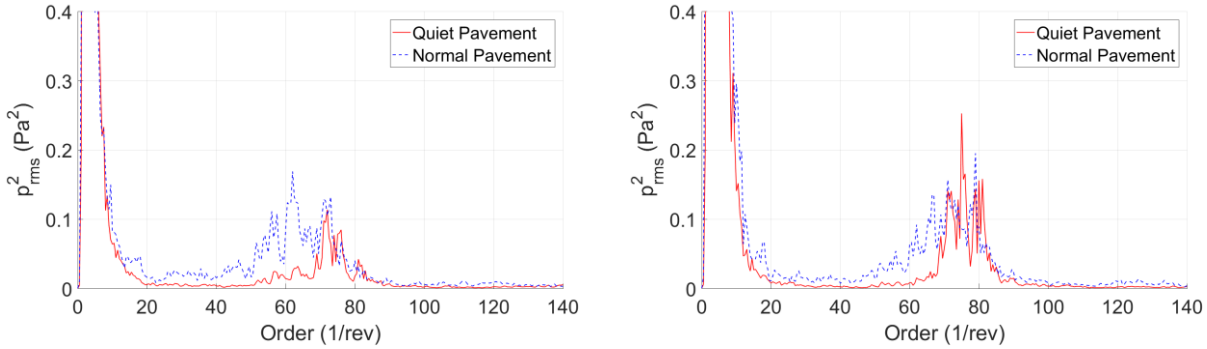

(a) Leading edge (b) Trailing edge

Figure 3- 15: Comparison of the non-tread pattern noise on different pavement for Tire 12 at 60 mph (order resolution: 0.5).

The results provide further validation to the currently used separation methodology. In addition, the results prove that the pavements have significant influence on the non-tread tire-pavement interaction noise, as expected.

3.4 Signal separation results for acceleration case

3.4.1 Effects of number of averages on the tread-pattern noise separation

In the current study, for the acceleration cases, the rpm order map is used rather than averaged order spectrum to investigate the signals that remain at the same order with the change of the speed. Unlike the constant speed cases, for acceleration, short time sequences are used for average instead of the entire time duration due to the speed variation. Different number of revolutions used for averaging in each time sequence has influence on the separation results. Hence, the results from different revolutions (2/4/6/8/10) used in each short sequence are investigated. The overlap is chosen to be half of the number of the revolutions used in one sequence (50% overlap). The rpm order map for the tread-pattern noise and the non-tread-pattern noise are presented in this investigation.

Tire 12 was selected for investigation in particular due to the high level of tread-pattern noise it generated. Figure 3- 16 shows the tread-pattern noise and the non-tread-pattern noise for all five numbers of averages used. The left column shows the tread-pattern noise and the right column shows the non-tread-pattern noise. From Figure 3- 16 (a), it can be seen that when only two averages are used, most tread-pattern noise can be separated; however, some non-tread-pattern noise components are also separated. Hence, over-separation will happen if only two averages are used. As the number of averages increases, the separation becomes more stable and mixing between the tread-pattern noise and the non-tread-pattern noise is reduced. It can be observed that when the number of averages is larger than six, the separation does not show noticeable change. Hence, it can be concluded from the current results that six revolutions are sufficient to remove the non-tread-pattern noise.

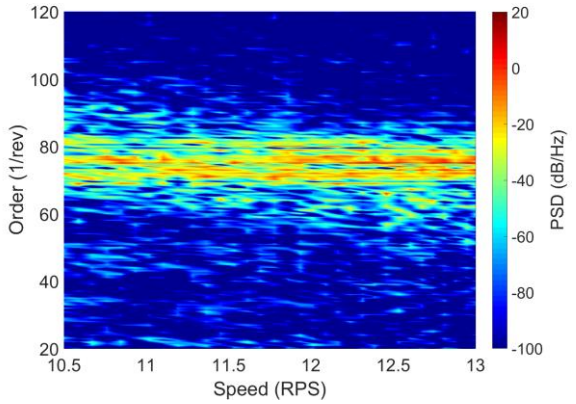

Tread-pattern noise

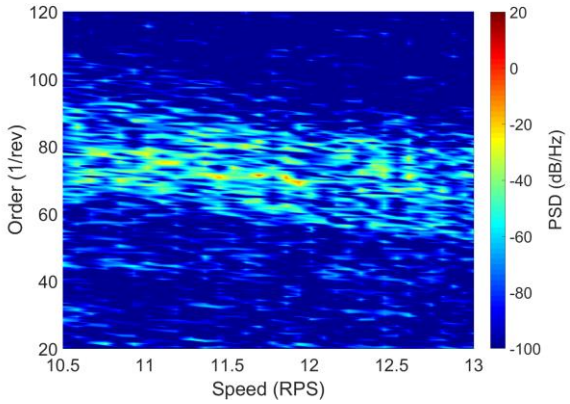

Non-tread-pattern noise

(a) 2 revs

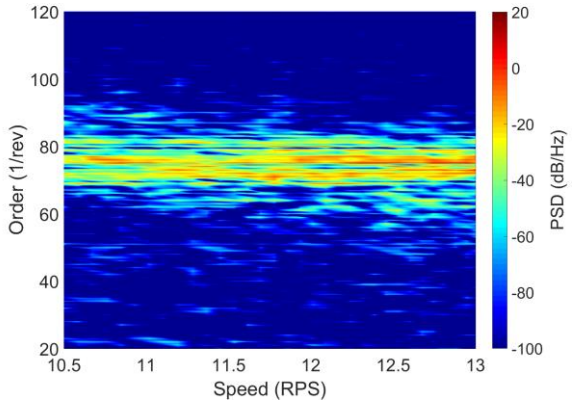

Tread-pattern noise

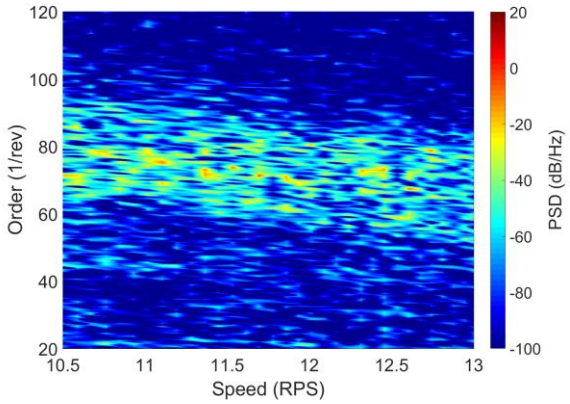

Non-tread-pattern noise

(b) 4 revs

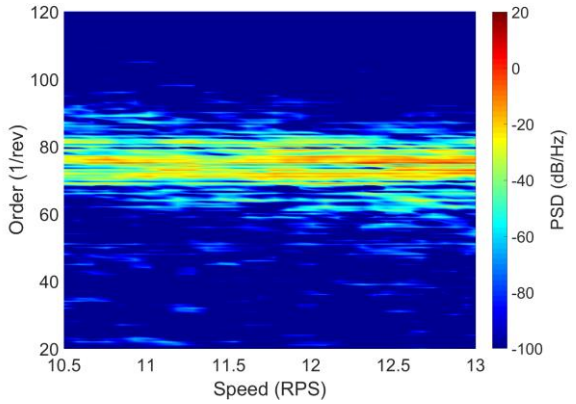

Tread-pattern noise

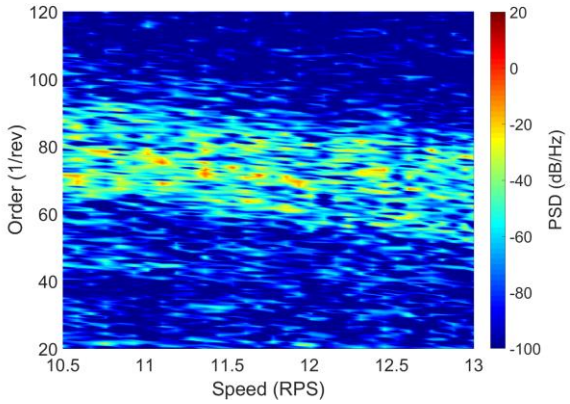

Non-tread-pattern noise

(c) 6 revs

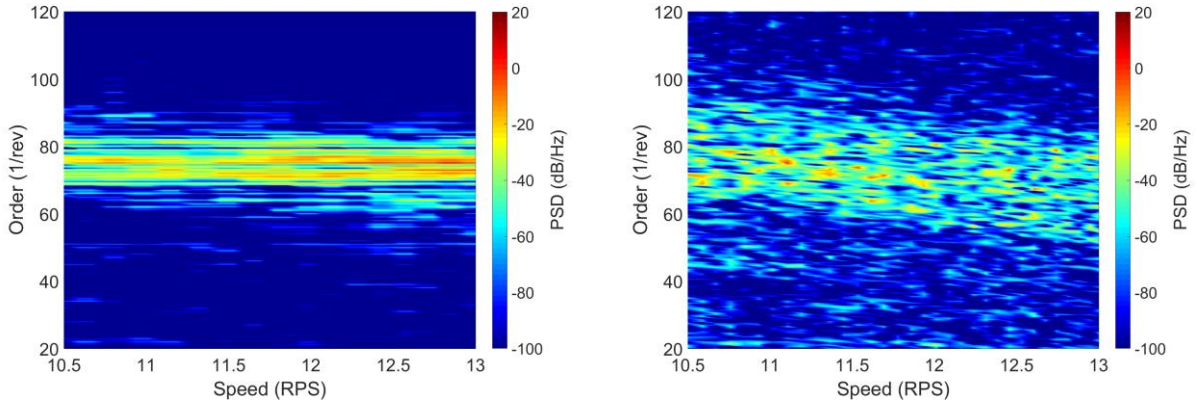

Tread-pattern noise Non-tread-pattern noise

(d) 8 revs

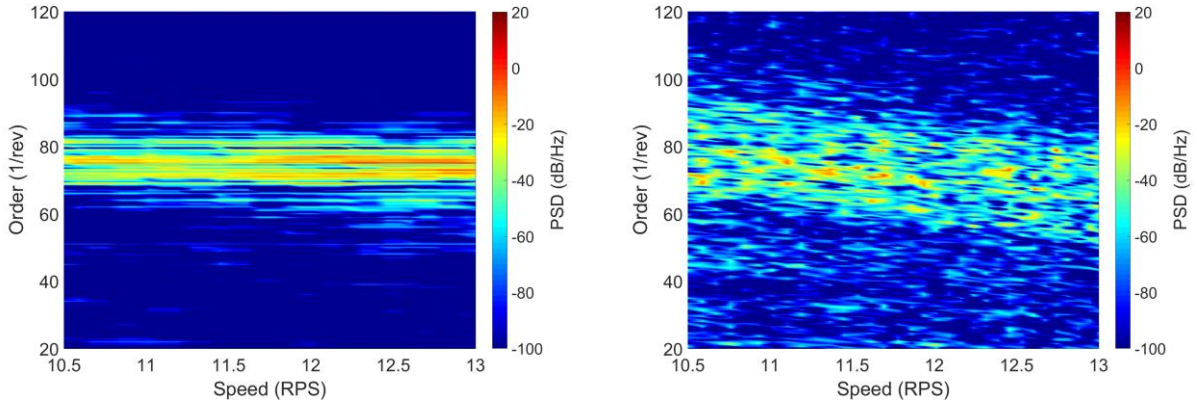

Tread-pattern noise Non-tread-pattern noise

(e) 10 revs

Figure 3- 16: Comparison of the tread-pattern noise for Tire 12 using different averaged revolutions (order resolution: 0.5).

3.4.2 Comparison of tread-pattern/non-tread-pattern/total noise

In this section, the order spectra of total noise, tread-pattern noise, and non-tread-pattern noise are placed together for comparison. Thus, the extent of tread-pattern noise separation is displayed. To maintain consistency with former investigations, Tire 12 is also chosen here. The results of the other tires can be found in Appendix-E. The number of revolution used is six with 50% overlap. It is shown in Figure 3- 17 and Figure 3- 18 that, at both the leading and trailing edge, most of the periodic components related to the tread pattern excitation have been separated

out. The results are analogous to the results of the constant speed (60mph) case, for which high amplitude of tread pattern noise can be observed. The separated signals remain at the order centered at the number of blocks of tread, which is 77.

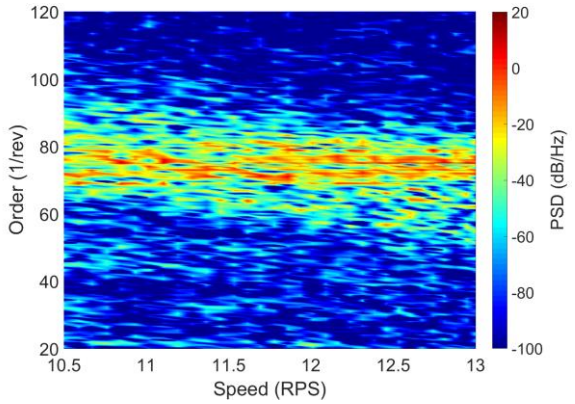

(a) Total Noise

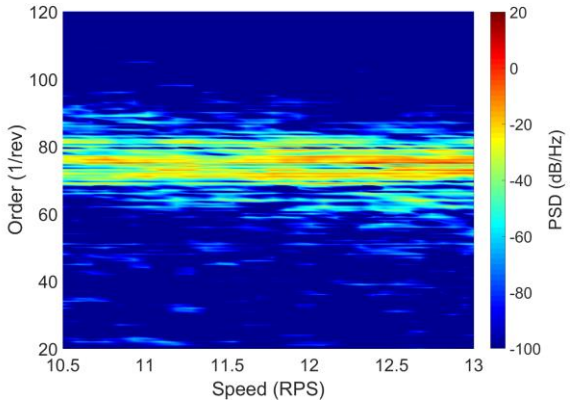

(b) Tread-pattern Noise

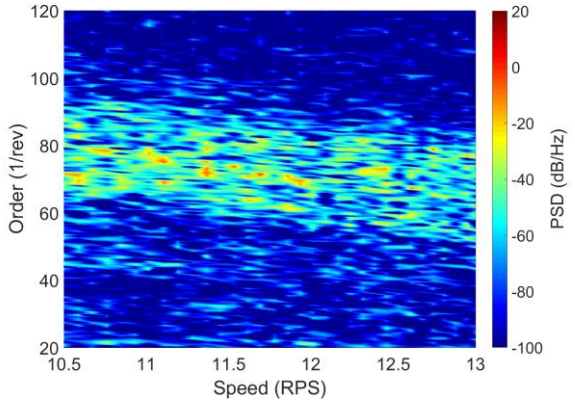

(c) Non-tread-pattern Noise

Figure 3- 17: Tire noise separation for Tire 12 in acceleration (order resolution: 0.5)-leading edge.

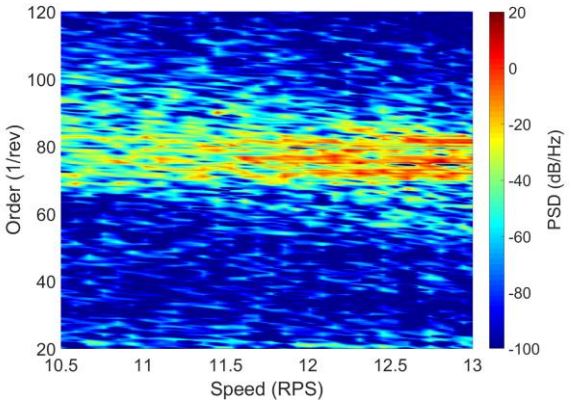

(a) Total Noise

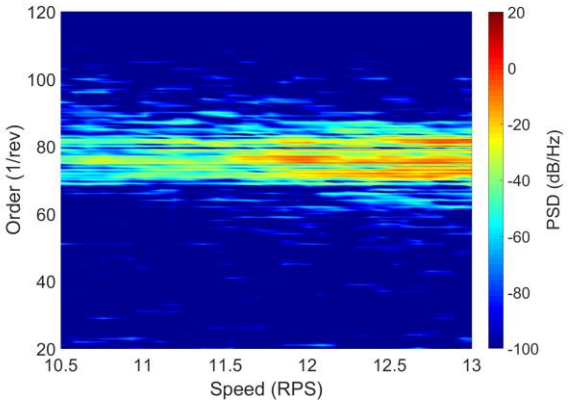

(b) Tread-pattern Noise

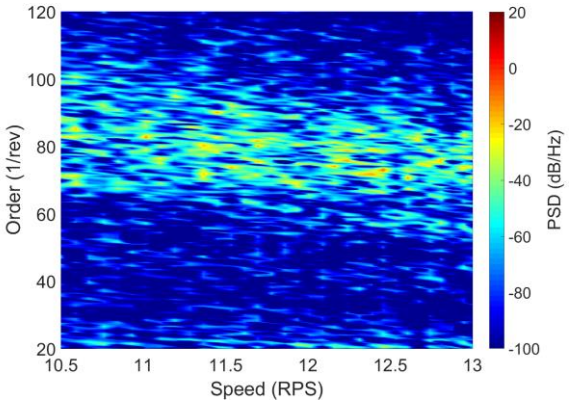

(c) Non-tread-pattern Noise

Figure 3- 18: Tire noise separation for Tire 12 in acceleration (order resolution: 0.5)-trailing edge.

3.5 Signal separation results analysis for tone case

The experimental data do not always adhere to expectations. For example, noticeable tones appear at one section of the east-bound road. These unexpected tones are hypothesized to be related to the pavement rather than tread pattern. Hence, separation was carried out for the signals with tone, in an attempt to identify whether or not they are related to the tread pattern. The Tire 20 at 60mph case was chosen for analysis. As shown in Figure 3- 19, for both the leading and the trailing edge, the tones do not appear in the tread pattern related noise component, which indicates that they are not related to the tire rotation. The separated tread pattern components are similar to the tread pattern noise separated from the TPIN without the tone. It can be concluded that the tone is related to the pavement properties, which will be further investigated in later experiments.

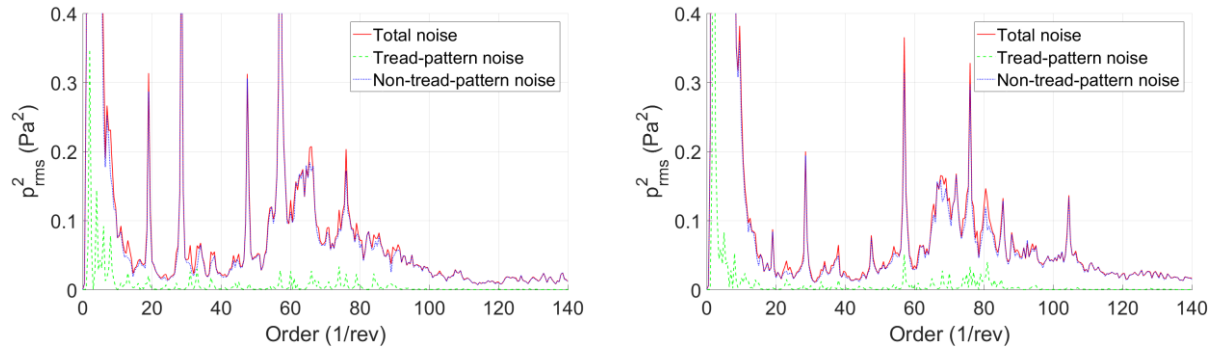

(a) Leading edge (b) Trailing edge

Figure 3- 19: Tire noise separation for the tone case with Tire 20 at 60 mph (order resolution: 0.5).

4 The application of signal processing techniques to tread-pattern noise separation

Though the TPIN separation using the optical sensor was successful, the separation of tread-pattern noise without optical signals is still of scientific interest. Hence, this thesis also investigates the application of several signal processing techniques for separating tread-pattern noise without using optical signals. First, the autocorrelation method is used to find periodicity in the signal. Then, a frequency domain filter, which has the capability of extracting deterministic signals from the total measured signals, is implemented on the simulated signal. However, this method did not succeed in separating signals related to tire rotation. Hence, the filter was not applied to the measured data. The principal component analysis (PCA) is used to summarize the information gathered from the measured multi-channel signals. Independent component analysis (ICA) is used to decompose multi-channel signals into different types of signal mixtures. The results obtained by each of these methods are analyzed and compared to the tread-pattern noise computed in Chapter 3. The effectiveness of each method for separation of the tread-pattern noise signals is also discussed. However, the methods being used currently all have their limitations in separating the tread pattern related signals.

4.1 Autocorrelation analysis

Autocorrelation, by definition, is the cross-correlation with the signal itself at different time delays. Autocorrelation is a widely used tool for checking randomness and finding periodicity of data. The basic idea for autocorrelation to detect the periodicity is that the periodic signal is still correlated with itself after time lag T. Hence, autocorrelation can be used for detecting the periodic components in the signals. For a set of discretized data in the time domain, the expression for autocorrelation is shown below:

$$R_{yy}(l) = \frac{1}{N}\sum_{n=0}^{N-1} y(n)\bar{y}(n-l) \qquad \text{Eqn. (4-1)}$$

where *N* is the total number of points of the data, l is the number of points of the time lag.

In the present study, the autocorrelation analysis is applied to sound pressure data measured by the OBSI system. Demonstration of autocorrelation analysis can be found in Appendix-F. Firstly, the autocorrelation analysis is applied to Tire 20 at 60 mph. The time history of the signals and autocorrelation is shown in Figure 4- 1. The whole length of the signals, which is sampled at 25.6 kHz, is about 10.5 s. The window selected for autocorrelation analysis is from the 76,801th to the 128,000th samples, which is a total of two seconds of data. It can be visually observed from Figure 4- 1 (b) that the autocorrelation contains much less random noise than the original signal in that time domain.

Then, the pressure power spectrum is computed using the conventional Fourier analysis on the total signal. At the same time, the pressure power spectrum is also computed by taking the Fourier transform of the autocorrelation and then computing the magnitude of the complex values. It can be seen from Figure 4- 2 that the autocorrelation spectrum shows clearer peaks than the power spectrum of original signals, which means that some broad-band signals are cancelled out by autocorrelation. However, the auto-spectrum still shows peaks in a wide frequency range for both leading edge and trailing edge signals. This indicates that the periodic signals are composed of signals from different sources, and tread-pattern noise is only one of the components of the periodic signals.

Figure 4- 3 shows the comparison between the auto-spectrum and tread-pattern noise spectrum computed using the optical signal (from Chapter 3), both of which show clear peaks around 1 kHz at both the leading edge and trailing edge. However, they do not show very good agreement.

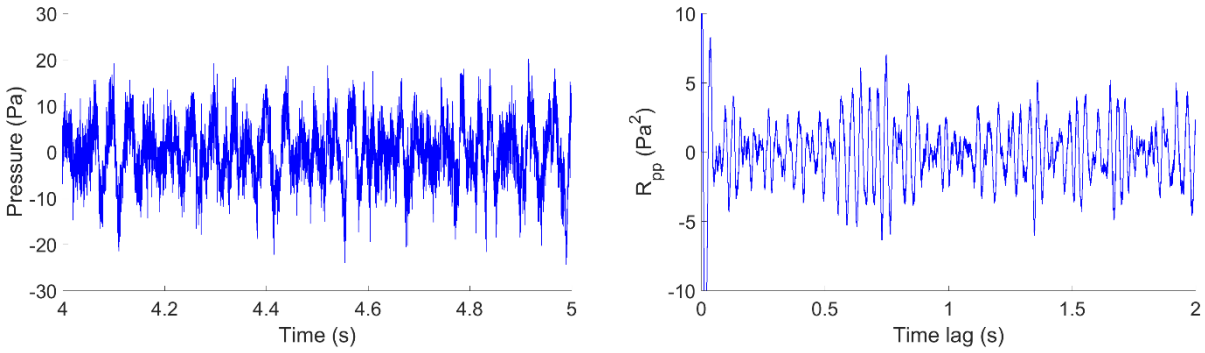

(a) (b)

Figure 4- 1: Time history of sound pressure and its autocorrelation for Tire 20 at 60 mph. (a) Sound pressure signal in window; (b) Autocorrelation of the sound pressure.

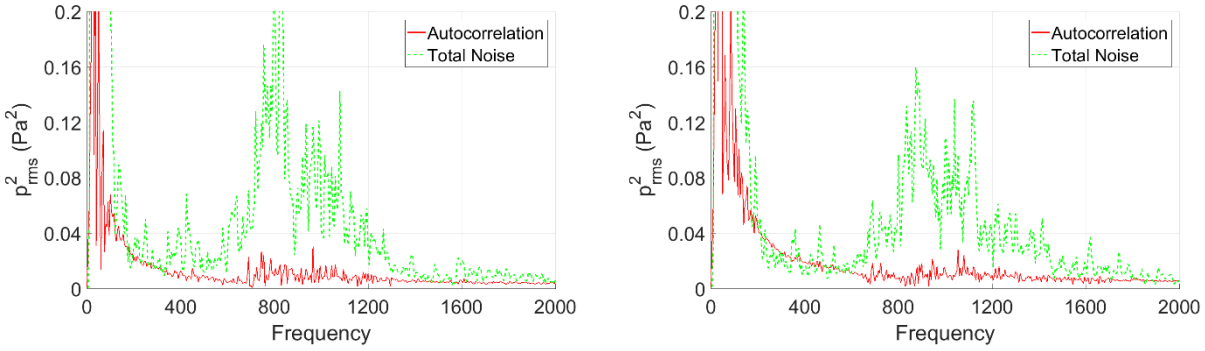

(a) Leading edge (b) Trailing edge

Figure 4- 2: Comparison between total noise spectrum and auto-spectrum for Tire 20 at 60 mph (frequency resolution = 5 Hz).

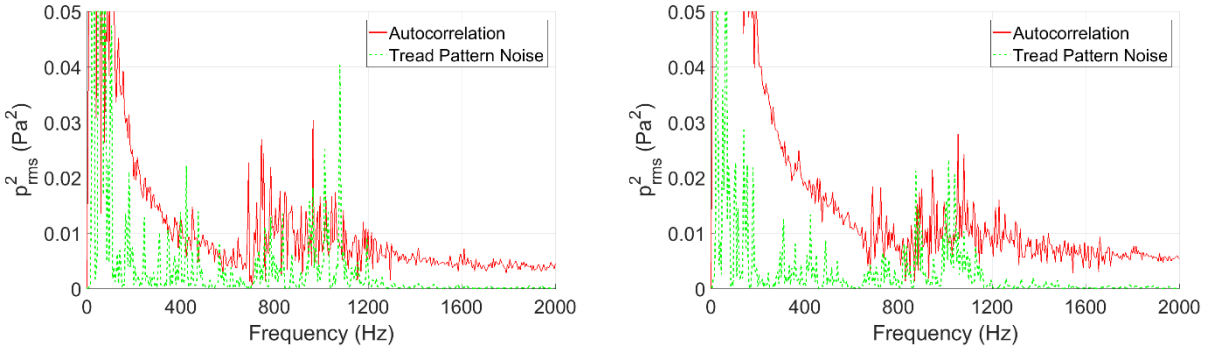

(a) Leading edge (b) Trailing edge

Figure 4- 3: Comparison between tread-pattern noise spectrum and auto-spectrum for Tire 20 at 60mph (frequency resolution = 5 Hz).

Then, the autocorrelation analysis is applied to Tire 12 at 60 mph. The whole time length of the signals, which is sampled at 25.6 kHz, is about six seconds. The window selected for autocorrelation analysis is from the 76,801th point to the 128,000th point, which contains a total of two seconds worth of data (between the 3rd and the 5th seconds). For Tire 12, the auto-spectrum shows clearer peaks than Tire 20; this is hypothesized to be related to the high-level tread pattern noise generated by Tire 12. As can be observed in Figure 4- 5, the auto-spectrum correlates much better with the tread-pattern noise than Tire 20, in shape but not in levels. Autocorrelation can preserve most periodic components in the signal, hence the results show that most periodic components of Tire 20 are not related to tread pattern, while for Tire 12 tread pattern plays a significant role in noise generation.

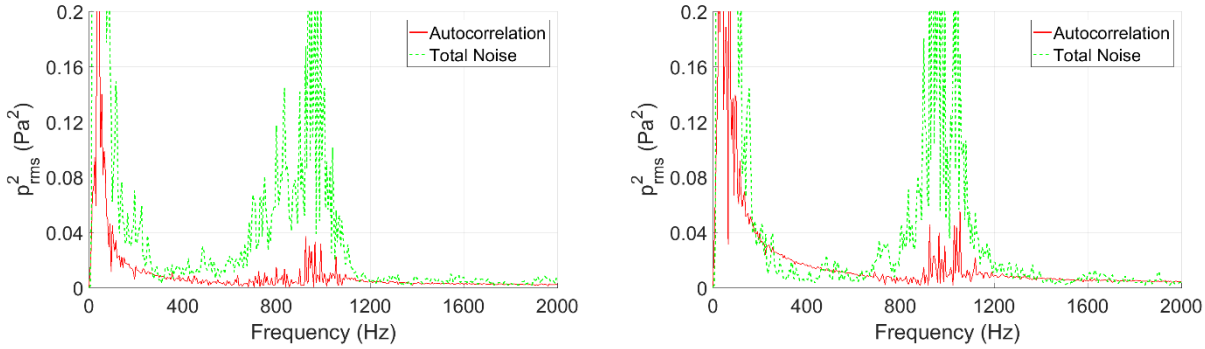

(a) Leading edge (b) Trailing edge

Figure 4- 4: Comparison between total noise and autocorrelation for Tire 12 at 60 mph (frequency resolution = 5 Hz).

(a) Leading edge (b) Trailing edge

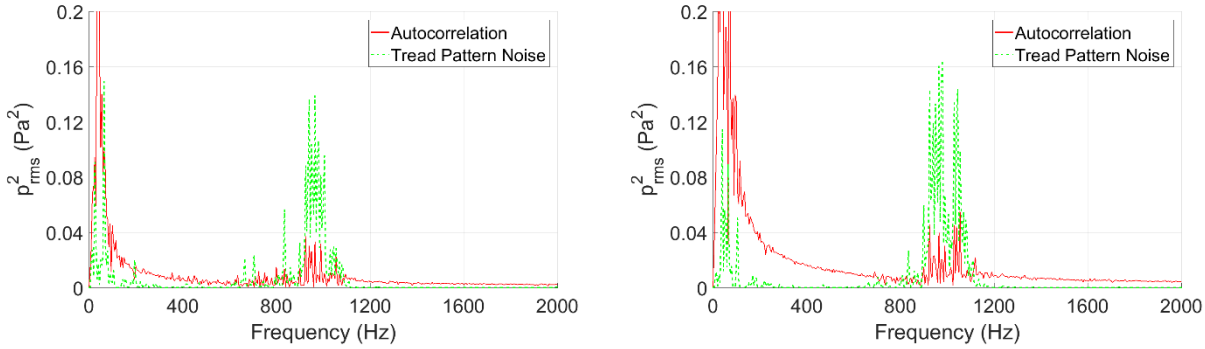

Figure 4- 5: Comparison between tread pattern noise and autocorrelation for Tire 12 at 60 mph (frequency resolution = 5 Hz).

The results from Tire 12 and Tire 20 show that autocorrelation analysis can extract most of the periodic signals, including both the signals related and unrelated to the tread pattern. By comparing the results of both tires, we can see that this method works better for Tire 12 than Tire 20. This means that Tire 12 contains more tread-pattern periodic signals while Tire 20 does not produce much tread-pattern noise. The results indicate that the autocorrelation works better for tires with higher pattern noise, which necessitates more validation later.

4.2 Frequency domain filter

4.2.1 Methodology

A frequency-domain (FD) algorithm was proposed for separating periodic signal from broadband signal [Antoni et al, 2004]. First, the problem is rephrased in terms of short-time sequences. Define $x_k(n)$ as a properly windowed sequence of length N taken at time kT, i.e. $x_k(n) = x(n + kT)w_N(n), n = 0, \dots\dots, N-1$ with $w_N(n)$, a weighting window of the length N. In the same way, let $x_k^d(n)$ be a sequence taken at time $kT - N - \Delta$, i.e. $x_d^k(n) = x(n + kT - N - \Delta)w_N(n), n = 1, \dots\dots, N-1$. The construction of sequences $x_k(n)$ and $x_k^d(n)$ is shown schematically in Figure 4- 6. The objective is to find the filter which best predicts $x_k(n)$ from $x(n)$. It should be noted that, in spite of the windowing, the deterministic components in the signal remain deterministic and are still perfectly predictable. However, the broadband noise will be rejected from the predicted $x_k^d(n)$ if the two are uncorrelated, which places as a constraint that Δ is strictly positive.

Under these conditions, the optimal filter achieving the minimum mean square prediction has a frequency response that can be given by,

$$H(f) = \frac{S_{x_k^d x_k}(f)}{S_{x_k^d x_k^d}(f)} = \frac{S_{p_k^d p_k}(f)}{S_{p_k^d p_k^d}(f) + S_{r_k^d r_k^d}(f)} \qquad \text{Eqn. (4-2)}$$

where $S_{CD}(f)$ is the cross-power spectrum between two arbitrary signals C and D; and $x_k(n) = p_k(n) + r_k(n)$ with $p_k(n)$ and $r_k(n)$ the deterministic and non-deterministic parts.

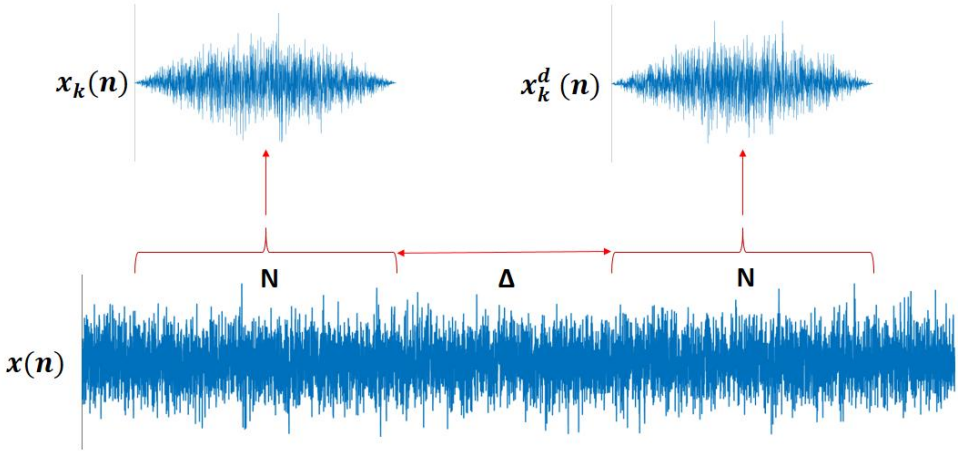

Figure 4- 6: Short-time sequence used in the frequency-domain algorithm.

Labelling $X_{k,M}(f)$ and $X_{k,M}^d(f)$ as M-long discrete Fourier transforms of $x_k(n)$ and $x_k^d(n)$.

$$X_{k,M}(f) = \sum_{n=kT}^{kT+M-1} x(n+kT)w(n)e^{-j2\pi nf} \qquad \text{Eqn. (4-3)}$$

The simple estimator of $H(f)$ on K sequences is thus given by,

$$\widehat{H}(f) = \frac{\sum_{k=1}^{K} \tilde{X}_{k,M}^d(f)\tilde{X}_{k,M}(f)^*}{\sum_{k=1}^{K} \tilde{X}_{k,M}^d(f)\tilde{X}_{k,M}^d(f)^*} \qquad \text{Eqn. (4-4)}$$

This quantity can now be transformed back into time domain to form a M-long noise cancellation filter to be applied directly on the measured signal $X(n)$.

4.2.2 Application of the FD filter to the simulating signals

Simulated signal, which was constructed in the same way as the signal introduced in section 3.2, is tested in this section. The signal contains sine wave with single frequency and white noise. The signal contains: (1) 200 Hz sine wave; (2) 80 order sine wave; (3) white noise. The sampling frequency of the signal is 25.6 kHz. The time length of one segment is chosen to be 0.1s, and in total 20 segments are used. The time delay is chosen to be the length of 52 segments, e.g., 5.2 seconds of data. As shown in Figure 4- 7. The 200 Hz sine wave becomes clear after filtering. However, the signal of interest, which is the 80 order signals, is filtered out. Hence, the method is not suitable for separating the tread-pattern noise out of the total TPIN.

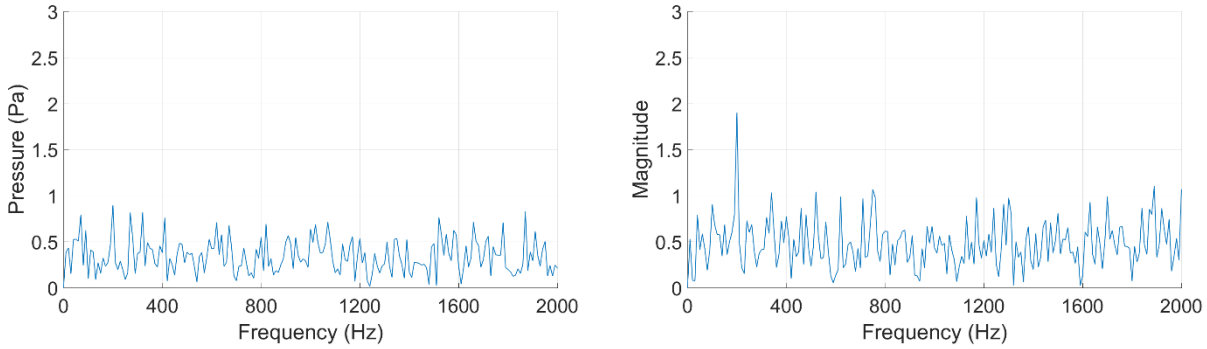

(a) Original signal (b) Filtered signals

Figure 4- 7: The power spectra of the short time sequence.

4.3 Principal component analysis

Principal component analysis is one method of summarizing data using linear combination of the original observations, to achieve dimension reduction. For p variables, $x_1, \dots\dots, x_p$, the data can be rotated and synthesized using proper coefficients, as shown below.

$$\boldsymbol{y}_m = a_{m1}\boldsymbol{x}_1 + a_{m2}\boldsymbol{x}_2 + \cdots + a_{mp}\boldsymbol{x}_p \qquad \text{Eqn. (4-5)}$$

This approach is preferable if rotation aims to maximize the variance of the data. The principal components (PC), which preserve most variance, can explain most of the data.

In this study, non-standardized data are used because different variables are based on synchronized measurement. First, the data is centered to have zero mean,

$$\boldsymbol{X}^c = \boldsymbol{X} - \overline{\boldsymbol{X}} \qquad \text{Eqn. (4-6)}$$

where $\boldsymbol{X}$ is the matrix the contains observations $\boldsymbol{x}_1, \dots\dots, \boldsymbol{x}_p$ as row vectors.

Then, the variance-covariance $\boldsymbol{S}$ matrix of the centered data matrix is calculated,

$$\boldsymbol{S} = cov(\boldsymbol{X}^c) \qquad \text{Eqn. (4-7)}$$

The eigenvalues λ_n and eigenvectors $\boldsymbol{e}_n$ of the variance-covariance matrix can be calculated. The eigenvalues represent the variance explained by one PC, and the eigenvector is the loading that transforms the original data into its principal components. The matrix $\boldsymbol{S}$ can be decomposed into the combinations of eigenvalues and eigenvectors,

$$\boldsymbol{S} = \lambda_1\boldsymbol{e}_1 + \cdots + \lambda_p\boldsymbol{e}_p \qquad \text{Eqn. (4-8)}$$

The eigenvectors can now be used to transform the originally observed data into a new set of data reordered according to value of variance,

$$\boldsymbol{y}_1 = \boldsymbol{e}_1^T \cdot \boldsymbol{X}^c$$

… …

$$\boldsymbol{y}_m = \boldsymbol{e}_m^T \cdot \boldsymbol{X}^c$$

… …

$$\boldsymbol{y}_n = \boldsymbol{e}_n^T \cdot \boldsymbol{X}^c$$

The eigenvalues corresponding to each eigenvector is the value of variance of the newly transformed data. For example, the variance of $\boldsymbol{y}_1$ is λ_1.

Tire 12 is chosen for analysis here. The time history and the spectra of the microphone signals of Tire 12 can be found in Figure 2- 6. The dominant frequencies for data from all three microphones are from 800 Hz to 1100 Hz. The first three eigenvalues of the 3 principal components are: 59.57, 30.25, 6.1, which indicates that the two PCs explain 93% of the variance and, hence, the first 2 PCs contain most of the data. This can be observed in Figure 4- 8 and Figure 4- 9. The amplitude of the time history of the signals shows a reduction between PC 1 and PC 3. In the frequency domain, in the dominant frequency range, the amplitude of PC 1 is much higher than PC 2 and PC 3. This is supporting evidence that that PC 1 preserved most of the information from the signal measured at different locations.

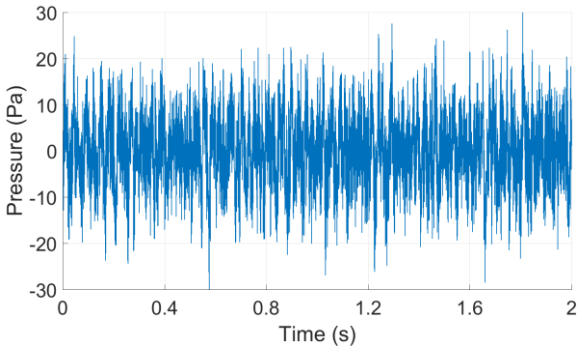

(a) PC-1

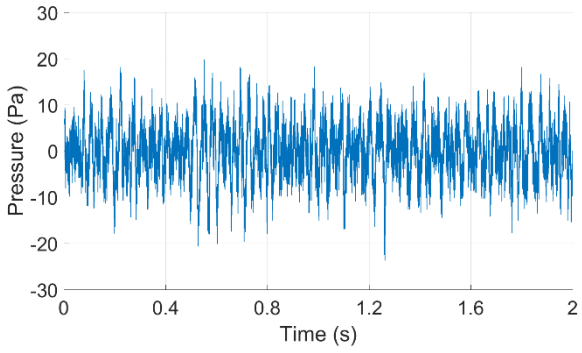

(b) PC-2

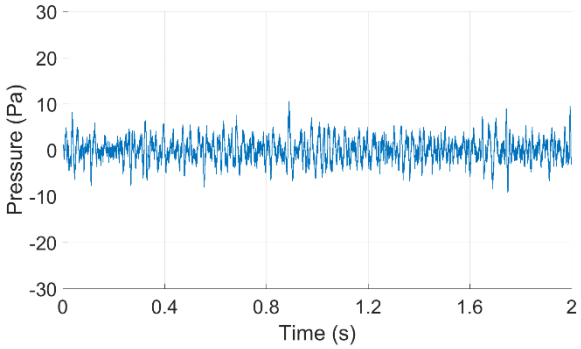

(c) PC-3

Figure 4- 8: Time history of the principal components-Tire 12 at 60 mph.

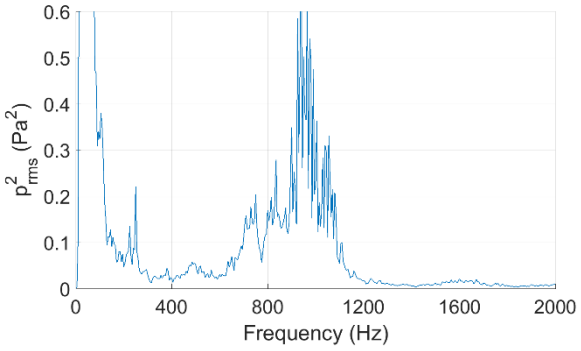

(a) PC-1

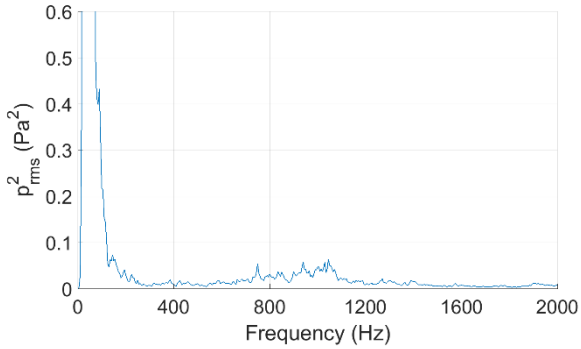

(b) PC-2

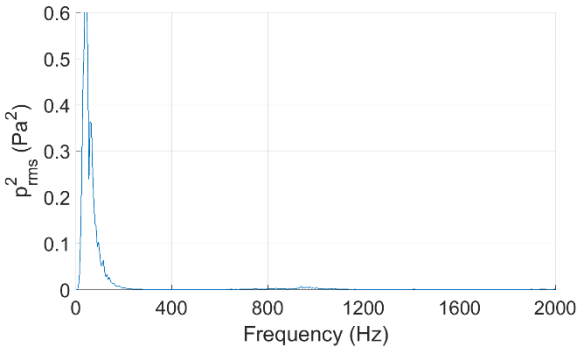

(c) PC-3

Figure 4- 9: Power spectra of the principal components-Tire 12 at 60 mph. (frequency resolution = 5 Hz).

Since PC 1 contains the most information related to the noise data, it is compared with the tread-pattern noise shown in chapter 3. In chapter 3, the tread-pattern noise spectra were displayed in order domain. However, for comparison with the spectra of the PC, the spectra of the tread-pattern noise introduced in chapter 3 are converted into frequency domain using the relationship between the speed and rotation. As shown in Figure 4- 10, PC 1 does not show significant matching with tread-pattern noise at either the trailing edge or the leading edge. One reasonable explanation for this lack of alignment is that, after summarizing the data into smaller numbers of data with large variances, the PCs with large variance contain noise generated from various other mechanisms.

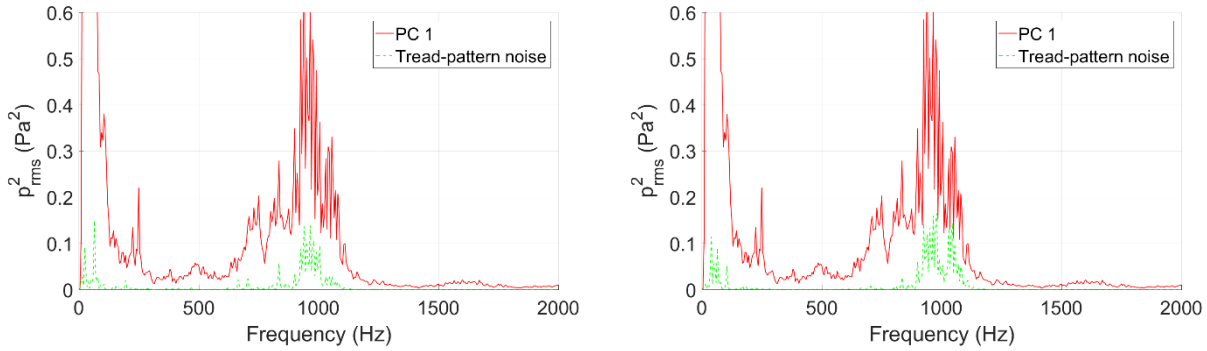

(a) Leading edge (b) Trailing edge

Figure 4- 10: Comparison between principal component and tread pattern noise-Tire 12 at 60 mph. (frequency resolution = 5 Hz)

4.4 Independent component analysis

In this study, independent component analysis (ICA) is applied to the measured data to test the feasibility of decomposing the near-field pressure signals into signals from different sources. The ICA can linearly decompose mixed signals from statistically independent and non-Gaussian sources into the original signals (Comon et al, 1994). In the ICA analysis, signals from different sources are supposed to mix linearly. Denote the observed variables by $yi(t), i = 1, \ldots, n, t = 1, \ldots, T$. In this definition, i is the index of the observed data variable and t is the index of time. The $xi(t)$ are typically signals measured by a device such as a microphone. We assume that they can be modelled as linear combinations of hidden variables $s_j(t)$, j=1, . . . ,m, with some unknown coefficients a_{ij},

$$x_i(t) = \sum_{j=1}^{m} a_{ij} s_j(t)\,, i = 1, \ldots \ldots, n \qquad \text{Eqn. (4-9)}$$

The only observable variable is $x_i(t)$, whereas both a_{ij} and $s_i(t)$ are to be estimated. The s_i are the independent components, whereas the coefficients a_{ij} are referred to as the mixing coefficients. Furthermore, the x_i are usually collected into a vector **x** of dimension n, the same is done for the s_i and the coefficients a_{ij} are collected into a mixing matrix **A** of size $n \times n$. Then, the model can be written as,

$$\mathbf{x} = \mathbf{A}\mathbf{s} \qquad \text{Eqn. (4-10)}$$

where **x** and **s** are now random vectors, and **A** is a matrix of parameters. Likewise, we can move to a matrix notation where the observed $x_i(t)$ are collected into a $n \times T$ matrix **X** and $s_i(t)$ are collected into a n × T matrix **S**, with i giving the row index and t giving the column index, giving the equation below:

$$\mathbf{X} = \mathbf{A}\boldsymbol{S} \qquad \text{Eqn. (4-11)}$$

The Eqn. (4-10) is in vector form, while the Eqn. (4-11) is formed by collecting the vectors into a matrix. The estimation of the mixing matrix **A** is critical in ICA. Several well-known algorithms have been developed to achieve the estimation. One of them is the fast fixed-point algorithm

(Hyvärinen et al, 1997), which is adopted in this study. After the matrix **A** is estimated, the independent components (IC) that represent the sources signals can be computed,

$$\mathbf{S} = \mathbf{A}^{-1}\mathbf{X} \qquad \text{Eqn. (4-12)}$$

Some simulated signals were generated and tested with ICA, which can be found in Appendix-G. First, the acceleration case of Tire 12 is analyzed, due to its high level of tread pattern produced noise. The order maps for data from the three microphones and three independent components are calculated for comparison. As shown in Figure 4- 11, the order maps of the total TPIN show a large proportion of the noise remains at the same order regardless of the rotation speed, while another part of the noise is not related to the tire rotation. For the order maps of the ICs (Figure 4- 12), IC 2 shows mostly the constant order component while IC 1 shows the components that are not related to tire rotation. The 77 order components become larger in IC 2 as the speed goes up. IC 2 shows strong characteristics of tread-pattern noise while IC 1 appears to be close to the non-tread-pattern noise. Hence, for Tire 12, the ICA method shows some potential to be able to break signals into components both related (IC 2) and unrelated (IC 1) to the tread pattern.

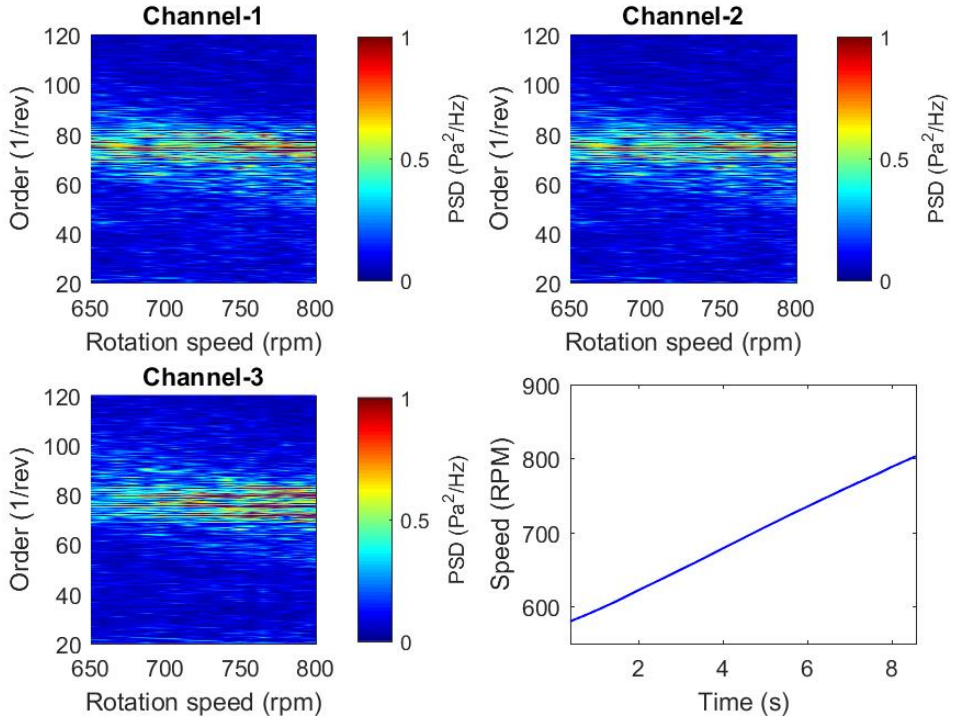

Figure 4- 11: Order map for microphone signal-Tire 12 in acceleration (order resolution = 0.5).

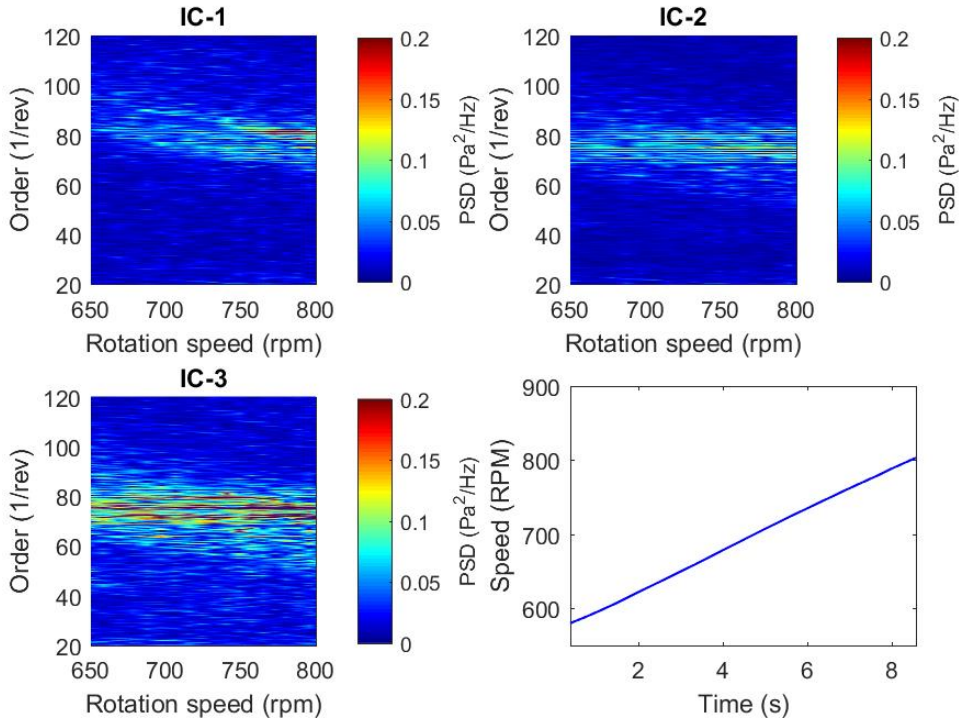

Figure 4- 12: Order map for independent components-Tire 12 in acceleration (order resolution = 0.5).

For Tire 20, as shown in Figure 4- 14, none of the order map of ICs shows clear separated tread-pattern components. As shown in Chapter 3, Tire 20 does not produce much tread-pattern noise. Hence, the results shown in Figure 4- 14 could be explained by the low tread-pattern noise level of Tire 20.

In spite of some potential that the ICA method shows to decompose the TPIN into components mixed by certain groups of sources, the results are still not satisfactory enough to make a strong conclusion that the tread-pattern noise can be separated from other mechanisms, especially for tires with low pattern noise. On one hand, the TPIN is mixed by noise generated from several complicated mechanisms; hence, the number of microphones to collect the data may be insufficient. On the other hand, two microphones within a single intensity probe are very close to each other, while the microphones in different intensity probes are much spaced further away. In the future, a new method of near-field microphone set-up with more microphones and different spacing could be tested for its efficiency in collecting tire noise data with the ICA method.

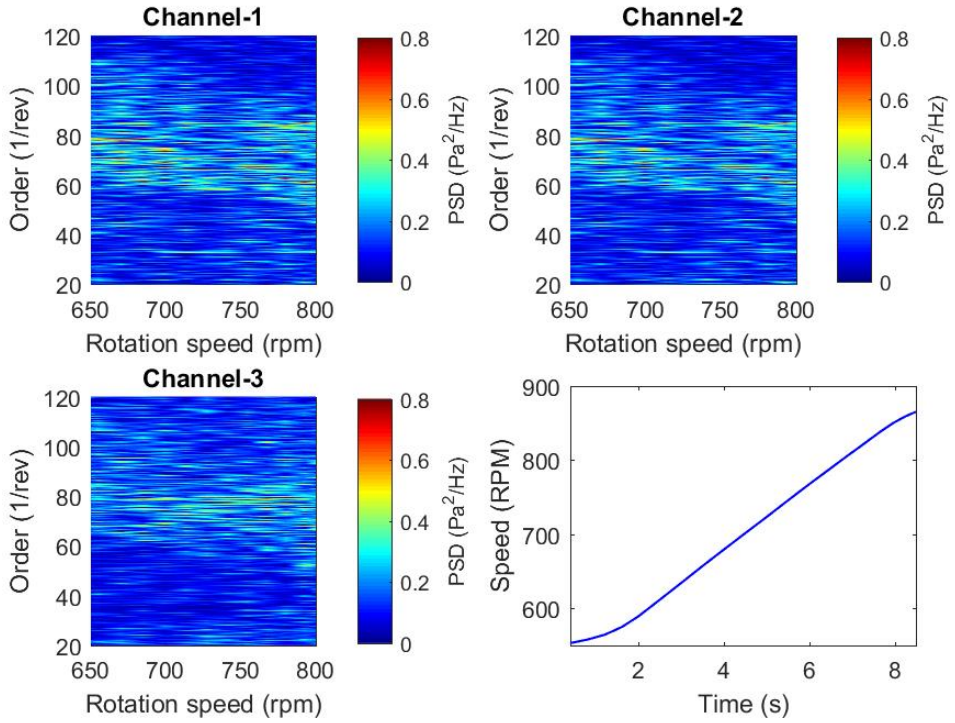

Figure 4- 13: Order map for microphone signal-Tire 20 in acceleration (order resolution = 0.5).

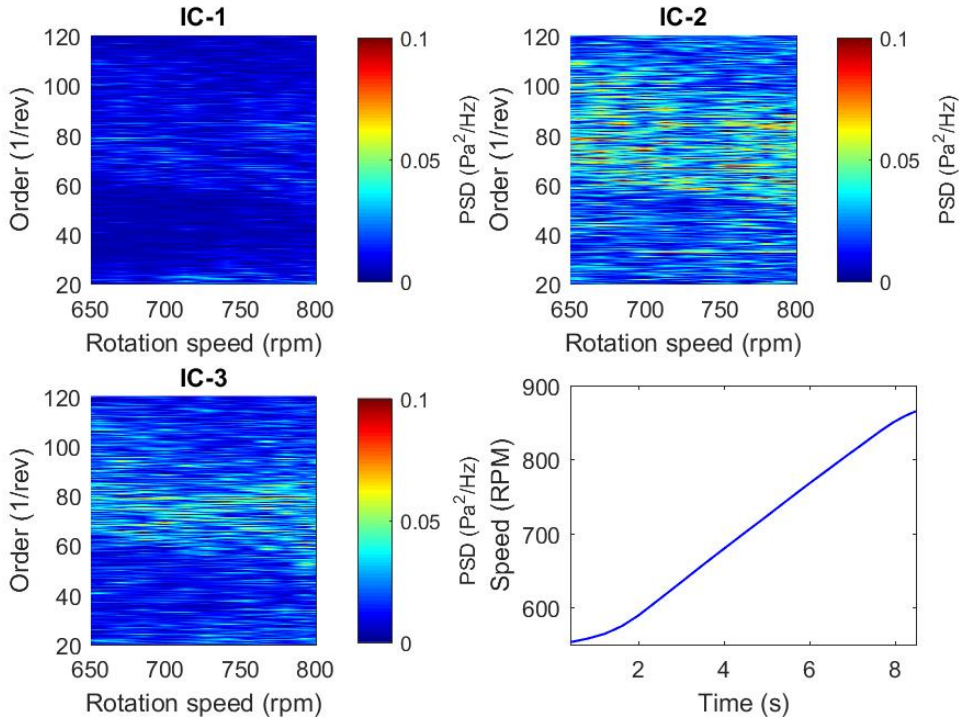

Figure 4- 14: Order map for independent components-Tire 20 in acceleration (order resolution = 0.5).

5 Correlation between tread pattern parameters and tread-pattern noise

This chapter will investigate the correlation between the tread-pattern noise and tread pattern parameters by comparing the "shape" of the tread-pattern spectra to the tread-pattern noise. The tread pattern parameters include tread pattern and air volume velocity spectra. To obtain the tread pattern parameters, the tire surface was digitized to obtain the 3D tread profile. Then, the binary matrix of the 2D tread patterns was obtained, and the order power spectra were calculated for the comparison with the tread pattern noise. The air volume velocity at the contact patch was also calculated using the tread profile. The comparison was conducted at the 3rd section of the chapter.

5.1 Tread pattern digitization

In this study, a CTWIST machine (Figure 1- 2) was utilized to scan the tire surface (the digitization is offer by Hankook). The digitization resulted in the three dimensional (3D) tread profiles of the five tires, which is in the format of a two dimensional 2D matrix saved in a text file. The 3D tread profile of Tire 20 is visualized as Figure 5- 1. The circumferential slice and horizontal slice are demonstrated in the same figure. The resolution of the 3D tread profile image is 4096*325, corresponding to the length of 2133.6 mm and the width of 165 mm, respectively. The 3D profile matrix shows a horizontally curved surface due to the inflation of the tire, which prevents the raw tread profile data from being directly used for the tread pattern analysis. Hence, codes have been developed to eliminate the curvature of the scanned tread surface profile in the horizontal direction for the more realistic representation of the tire surface that is in contact with the road, which is detailed in the next paragraph. The curved 3D tread profile is also converted directly to a 2D tread pattern matrix, which is used for the tread pattern order spectra calculation in this study.

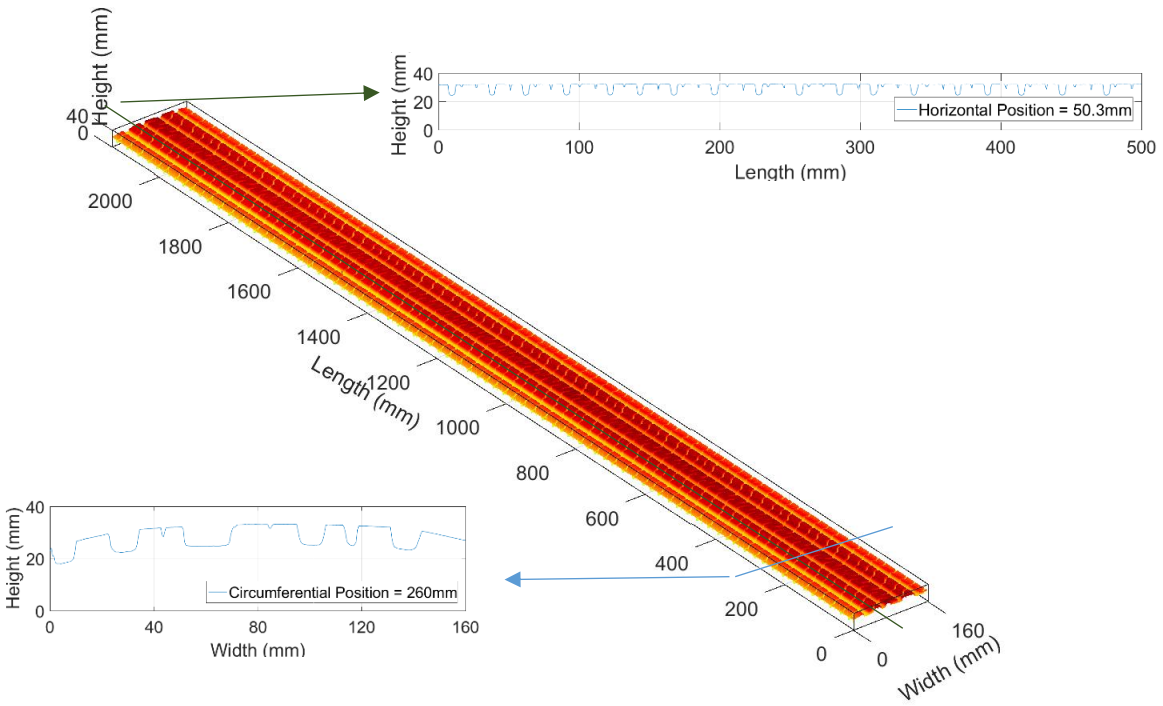

Figure 5- 1: Original tread profile demonstration of Tire 20 (SRTT).

The CTWIST machine digitized the entire tire surface, which includes section that transitions between the tread and the side wall. Hence, part of the tread surface is cut off symmetrically at both edges of the tire. For Tire 20, demonstrated in Figure 5- 2, 165 mm of manually-measured tread width is cut out of a width of 199.1 mm. After choosing proper tread width, the 3D tread profile is processed to eliminate its horizontal curvature. First, the highest point for n^{th} circumferential line with tread blocks is found and the height H_n is recorded. Then, the global maximum value H is picked out of the highest points (H_n) for all the circumferential lines. The height difference for the highest point of each circumferential line and the global highest point is calculated,

$$\Delta h_n = H - H_n \qquad \text{Eqn. (5-1)}$$

Then, the height difference Δh_n is added to all the points in the n^{th} circumferential line. After the elimination of the horizontal curvature, all the circumferential lines on the tread surface have the same reference height. The horizontally 3D tread profile without horizontal curvature is shown in Figure 5- 2.

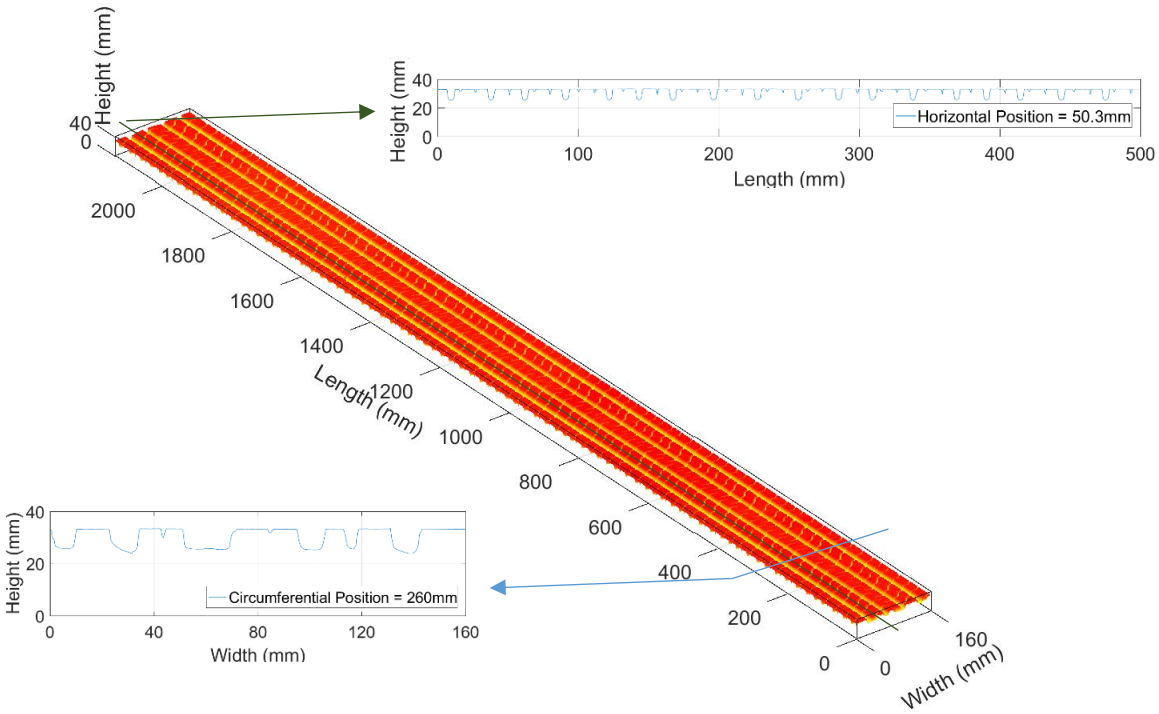

Figure 5- 2: De-curved tread profile demonstration-Tire 20 (SRTT).

The 3D tread surface height profile is also converted into a 2D tread pattern binary matrix for the calculation of the tread pattern spectral content. To this end, the highest points h_{max}^{n} and lowest points h_{min}^{n} for nth circumferential line are identified. Then, the height difference between the highest point and the lowest point of the nth line is calculated,

$$\Delta h_{max}^{n} = h_{max}^{n} - h_{min}^{n} \qquad \text{Eqn. (5-1)}$$

using Δh_{max}^{n}, the circumferential grooves are differentiated from the circumferential lines with both blocks and grooves. A reasonable difference threshold height Δh_{t}^{n} is set, according to the actual measurement, which is 4 mm for Tire 20. If $\Delta h_{max}^{n} \geq \Delta h_{t}^{n}$, the nth circumferential line has both tread blocks and tread grooves; otherwise, if $\Delta h_{max}^{n} < \Delta h_{t}^{n}$, the nth circumferential line belongs to the circumferential tread groove.

After the type of the circumferential line is identified, further detailed differentiation is needed to identify tread blocks and grooves in the rib. In this step, the height difference between all the points and the highest points in nth line is calculated,

$$\Delta h_m^n = |h_m^n - h_{max}^n|$$

where m means the m[th] points in the n[th] circumferential line. Analogous to the differentiation between different types of the circumferential lines, a reasonable difference threshold height Δh_t^m is set for tread block and groove within one line, according to the actual measurement, 3 mm is chosen for Tire 20. If $\Delta h_m^n \geq \Delta h_t^m$, the m[th] point in the n[th] circumferential line is in tread block; otherwise, if $\Delta h_m^n < \Delta h_t^m$, the m[th] point in the n[th] circumferential line belongs to the groove.

After all the points in the tread profile are identified, the points representing the tread block are assigned the value 1, while the points representing the tread groove are assigned the value 0. In this way, the 3D tread profile is digitized into a binary image matrix, in which digit 1 represents blocks and digit 0 represents grooves. The digitized 2D tread patterns of the five tires are shown in Figure 5- 3.

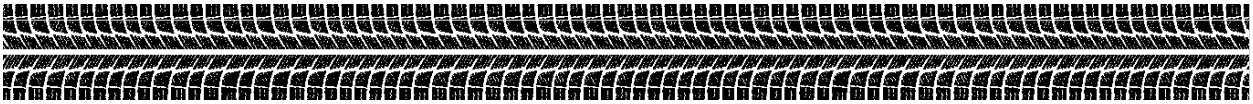

T12

T15

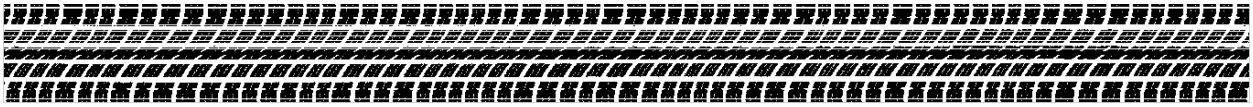

T18

T19

T20

Figure 5- 3: Tread patterns of tires.

5.2 Tread pattern and air volume velocity spectrum

The procedure of converting the 2D tread patterns into phase domain, which is a special form of time domain signals with constant phase increment, is shown in Figure 5- 4. The demonstration of the tread content for a section of one circumferential line is shown in Figure 5- 4 (b), which starts at 0 mm and ends at 500 mm. The unit of the phase is chosen to be rev. Hence, the phase of completing one revolution is 1,

$$p_{1-rev} = 1$$

where p_{1-rev} is the phase angle to complete one revolution. It is straightforward that the phase of each circumferential position can be calculated by linear interpolation,

$$p_m = \frac{m}{N} p_{1-rev}$$

where p_m is the phase of m^{th} circumferential position, N is the total number of digitized tire pixels in one revolution. Following the aforementioned procedures, the tread information can be converted into phase domain, as shown in Figure 5- 4 (c).

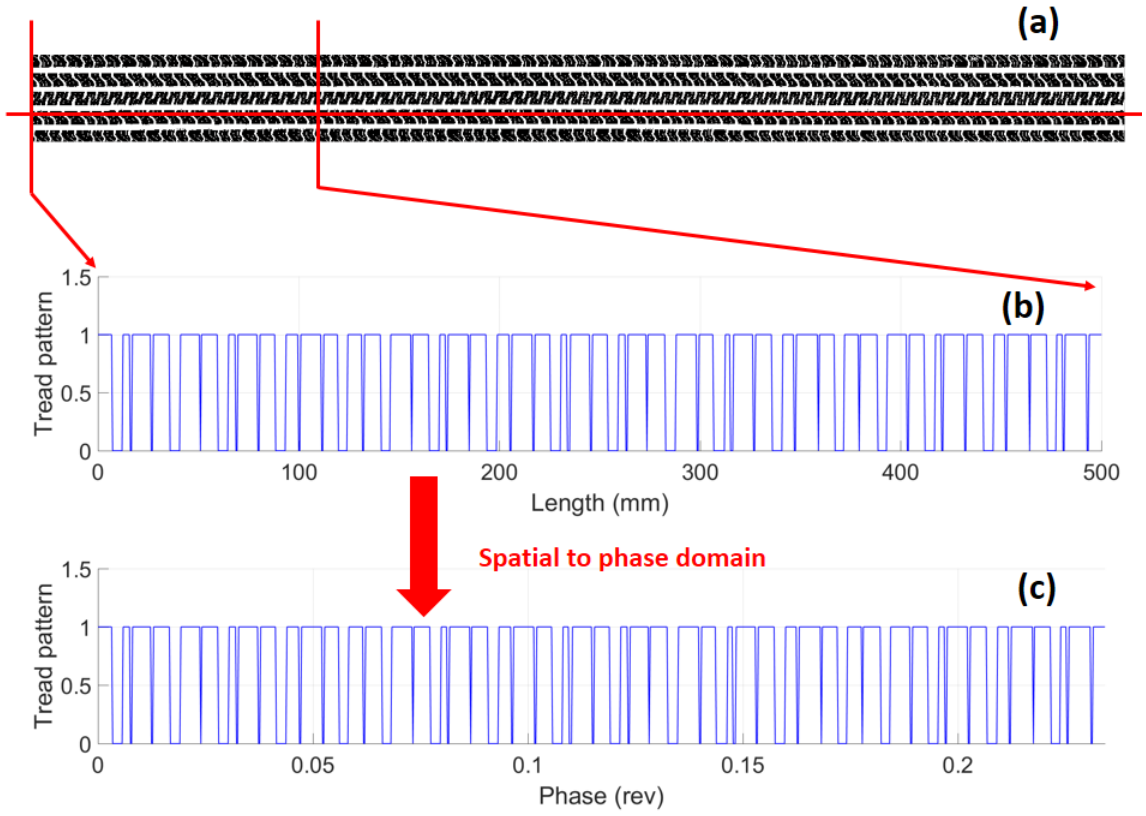

Figure 5- 4: Demonstration of 2D tread pattern conversion into phase domain.

After obtaining the phase domain signal, the Fourier transform is applied to the tread signals of circumferential lines. The phase domain tread pattern signal is converted to 2D tread pattern order spectra in this way, as shown from Figure 5- 5 to Figure 5- 9 (a). In those plots, the X-axis is order (1/rev), the Y-axis is the horizontal position (mm), and the colored lines represent the tread pattern component power in the order domain.

Then, the 2D tread pattern spectral information is reduced to a single representative spectrum. To take into account the tread block offset information, the coherent averaging approach is utilized in this study. The averaging process across the tire width is performed using the Fourier transform complex data. Then, the spectrum is computed by taking the root mean square of the magnitude of complex Fourier transformed values. In this way, the coherently averaged tread pattern order spectrum can be obtained, as shown from Figure 5- 5 to Figure 5- 9 (b). This averaged power spectrum is called a coherent tread pattern spectrum since it accounts for the relative phase between tread patterns along the tire width.

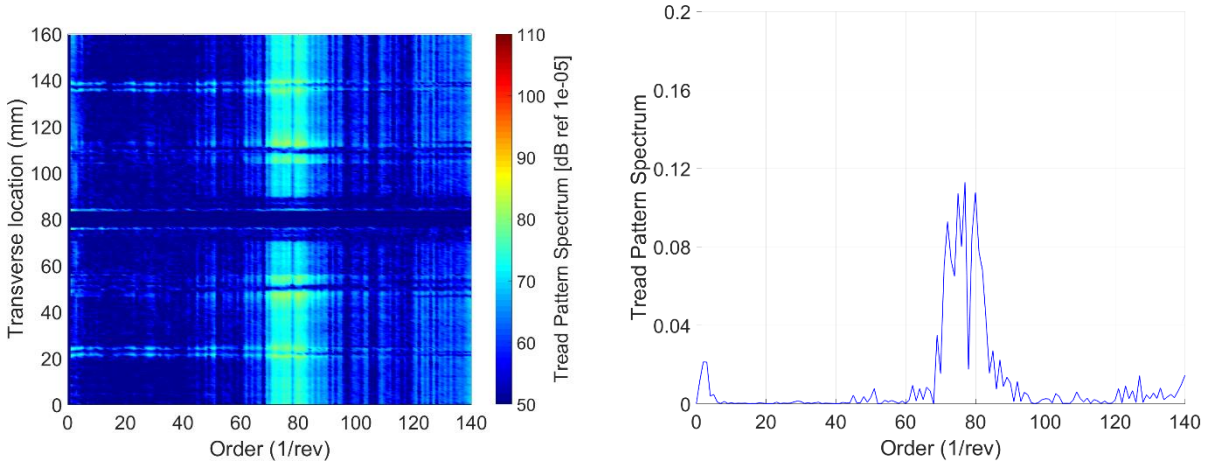

(a) (b)

Figure 5- 5: Tread pattern spectral content-Tire 12. (a) Tread pattern spectra for all of the horizontal positions; (b) coherently averaged spectrum. (order resolution = 1).

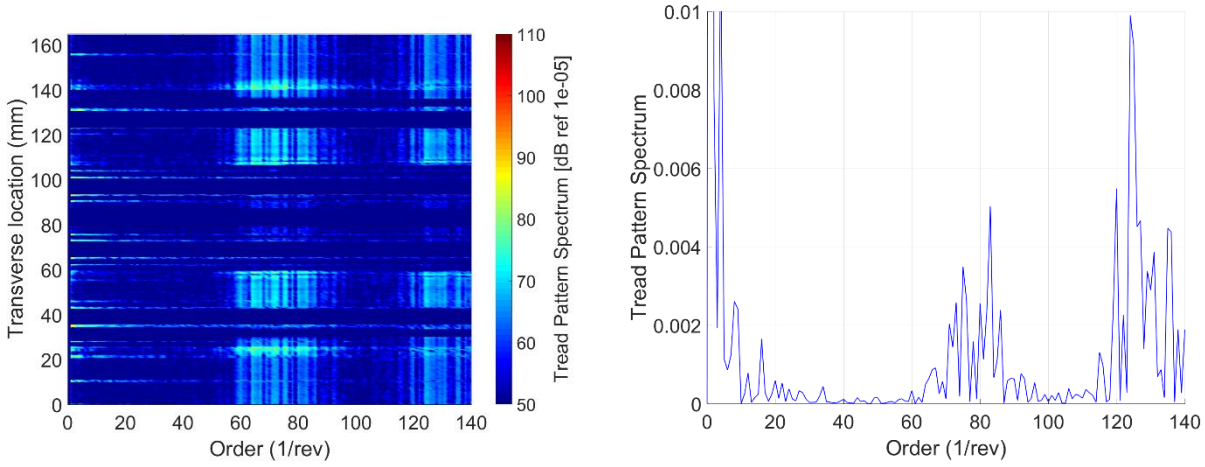

(a) (b)

Figure 5- 6: Tread pattern spectral content-Tire 15. (a) Tread pattern spectra for all of the horizontal positions; (b) coherently averaged spectrum. (order resolution = 1).

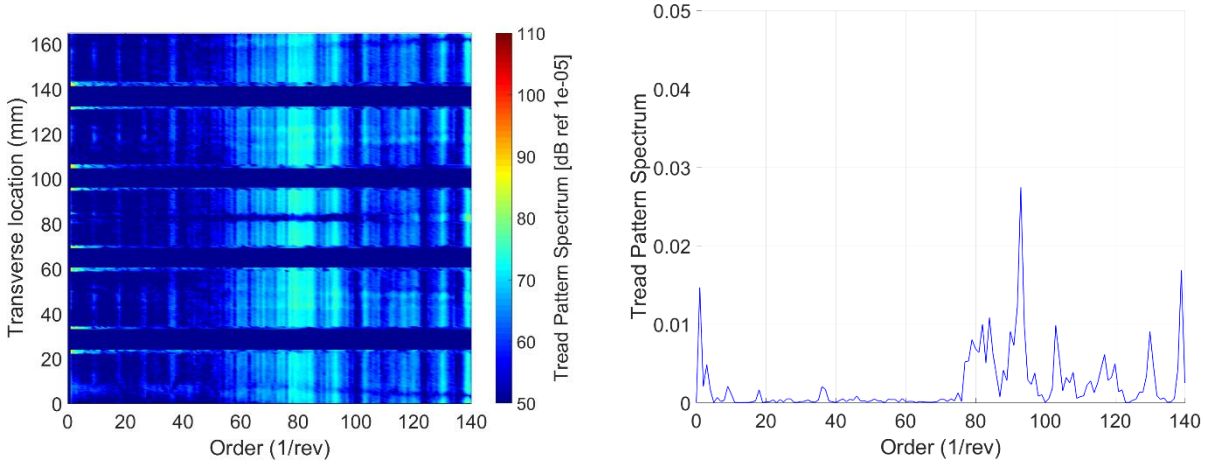

(a) (b)

Figure 5- 7: Tread pattern spectral content-Tire 18. (a) Tread pattern spectra for all the horizontal position; (b) coherently averaged spectrum. (order resolution = 1).

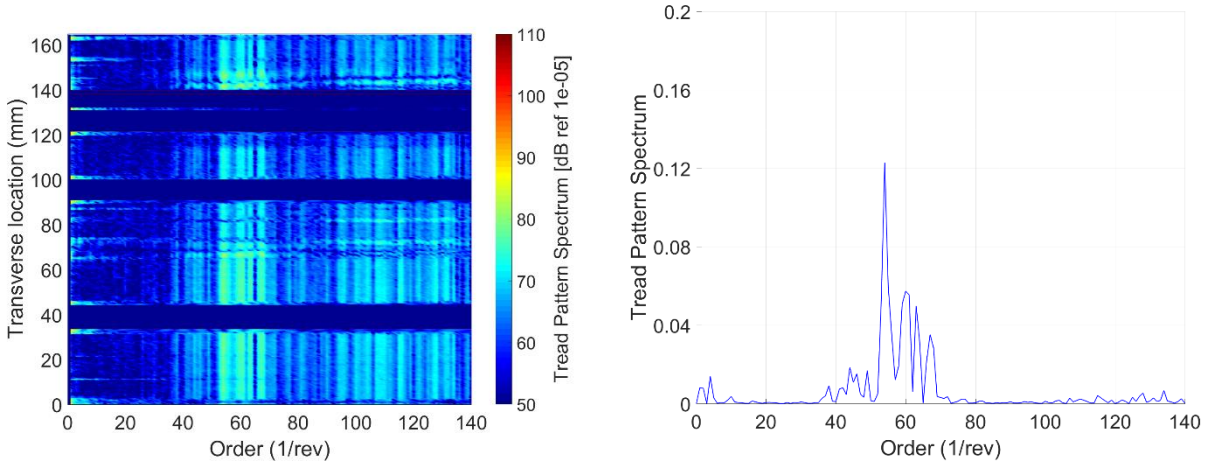

(a) (b)

Figure 5- 8: Tread pattern spectral content-Tire 19. (a) Tread pattern spectra for all of the horizontal positions; (b) coherently averaged spectrum. (order resolution = 1).

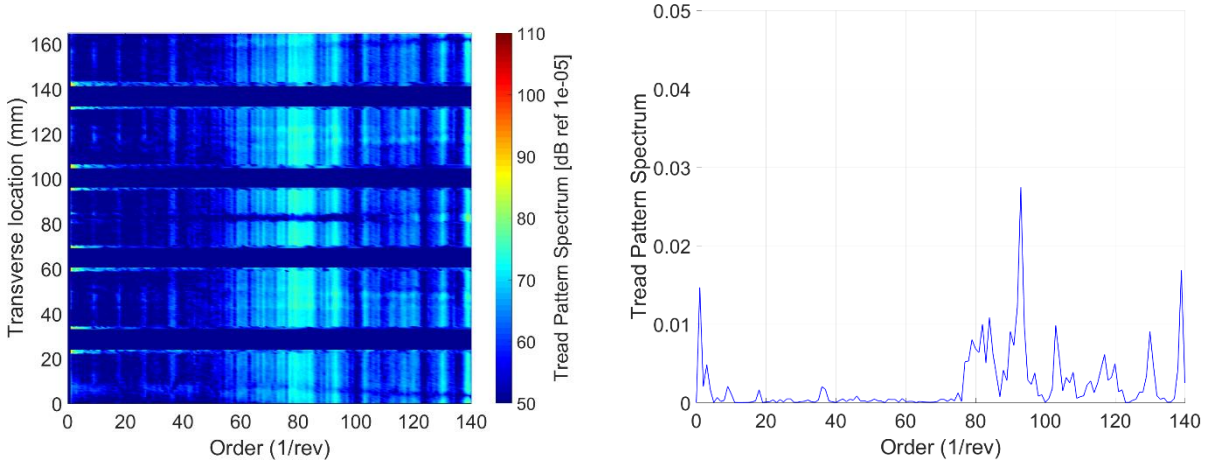

(a) (b)

Figure 5- 9: Tread pattern spectral content-Tire 20. (a) Tread pattern spectra for all of the horizontal positions; (b) coherently averaged spectrum. (order resolution = 1).

The coherent tread pattern spectra of the five tires are plotted together in Figure 5- 10. It can be observed that the two snow tires, which are Tire 12 and Tire 19, have a relatively high level of power spectra. The level of the power spectrum of the tread pattern is assumed to be related to the tread pattern produced noise. This hypothesis will be examined in the next section by comparing the tread pattern noise spectra and the tread pattern spectra.

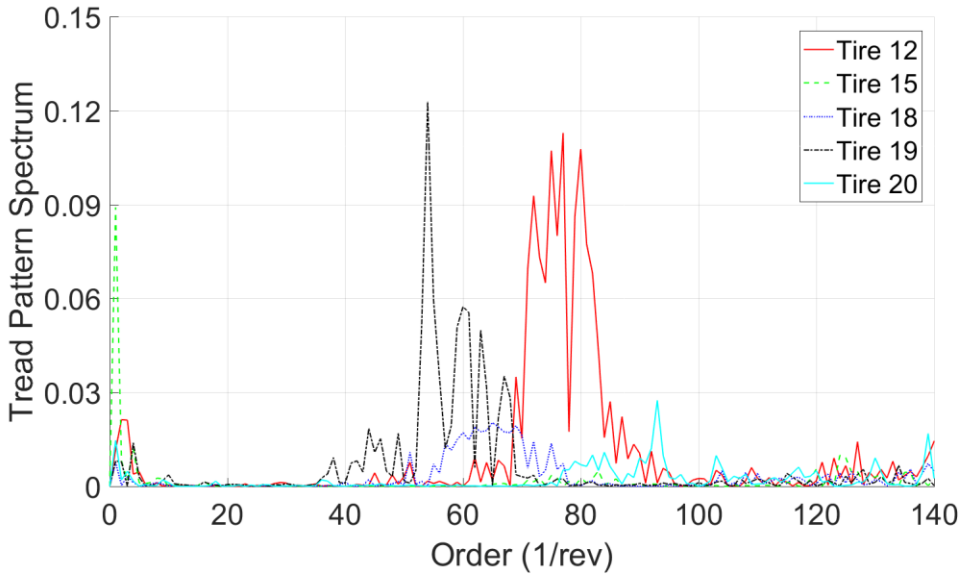

Figure 5- 10: Coherently averaged tread profile order power spectra of all tires (order resolution=1).

Another mechanism for tire noise generation related to the tread pattern is air pumping. The air pumping mechanism is caused by the variation of air volume enclosed between the tread and the road surface at the contact patch. The noise generation is related to the air volume velocity (Kinsler et al., 2000). For monopole sound sources, the pressure is given by,

$$\boldsymbol{p}(r,t) = \frac{\rho c k}{4\pi r}\boldsymbol{Q}e^{-ikr} \qquad \text{Eqn. (5-1)}$$

and

$$\boldsymbol{Q} = Qe^{i\omega t} \qquad \text{Eqn. (5-2)}$$

where **p** is acoustic pressure (bold indicates complex number), ρ is the density of the acoustic medium, *c* is the sound speed in that medium, *r* is the distance from the source, *t* is time, *k* is the wavenumber ($k = \omega / c$). The letter *Q* is the volume velocity or source strength (**Q** is its complex form), *i* is imaginary unit, ω is radian frequency of the acoustic wave.

The air volume velocity Q is the time derivative of the air volume V,

$$Q = \frac{dV}{dt} \qquad \text{Eqn. (5-3)}$$

Hence, the air volume at the contact patch is calculated for each time step. A schematic demonstration of the air volume velocity calculation is shown in Figure 5- 11. The previous study indicated that the air pumping noise is related to the air volume velocity; thus, the calculation of the air volume velocity at the contact patch is critical. The air volume under the contact patch at one particular moment is calculated by adding up the groove volume at the contact patch,

$$V^n = \sum V_{i,j}^n \qquad \text{Eqn. (5-4)}$$

where V^n represents the air volume at the contact patch at the nth time point; in $V_{i,j}^n$, letters i and j represent ith row and jth column in the tread profile matrix, respectively.

After calculating the phase history of the air volume at the contact patch, the air volume velocity can be calculated by taking the derivatives of the air volume phase history.

$$Q^n = \frac{V^n - V^{n-1}}{\Delta p} \qquad \text{Eqn. (5-5)}$$

where Q^n is the air volume velocity at the nth time step, Δp is the phase interval between the two adjacent time points. Finally, Fourier transform can be applied to the air volume velocity to calculate the air volume velocity spectrum.

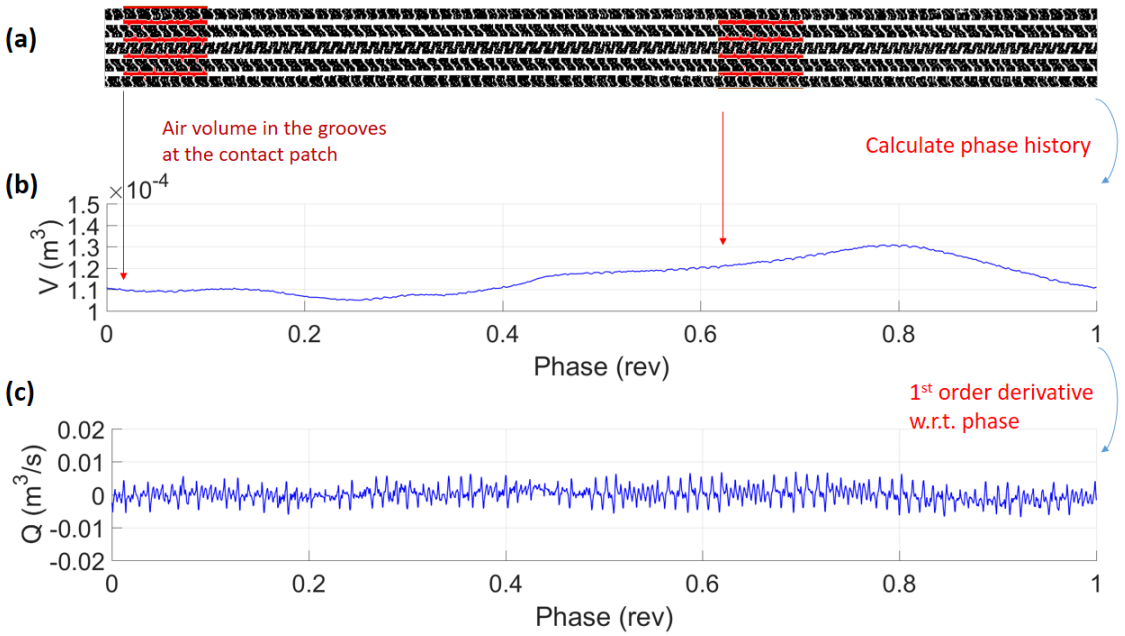

Figure 5- 11: Calculation of the air volume velocity at the contact patch-Tire 20.

Figure 5- 12 shows the order spectra of air volume velocity for all the five tires. As shown in 0, the order ranges at which the peaks occur is recorded according to visual inspection, and they are compared with the number of blocks for each tire. It was found that the number of tread blocks in one circumference is always within the peak range for all the tires. This shows that the tread pattern spectral content is still related to the tread pattern fundamental impact frequency after the randomization of the tread pattern design.

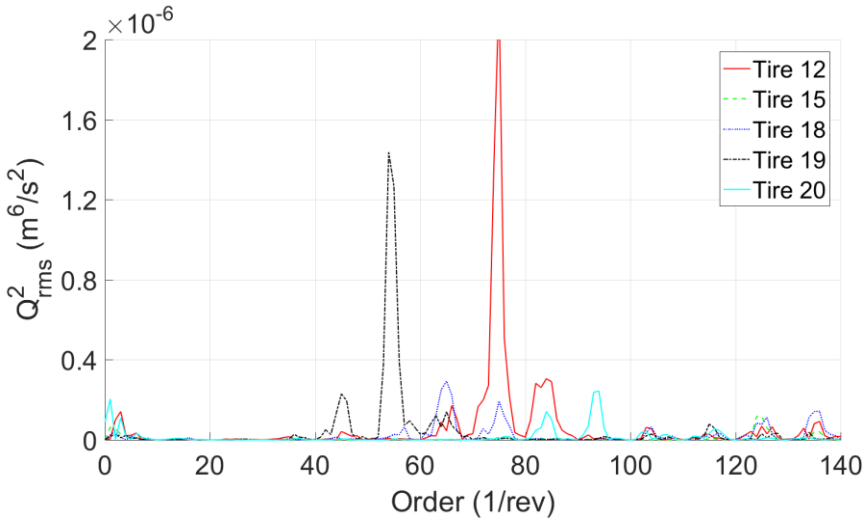

Figure 5- 12: Air volume velocity order power spectra (order resolution=0.5).

In Figure 5- 13, the tread pattern spectra and air volume velocity spectra for the each tire are plotted in the same graph for comparison. It can be observed that the peaks of the air volume spectrum match the peaks of tread pattern spectrum closely, while the tread pattern spectra show broader band width than the air volume velocity spectra. The number of tread blocks of each tire has been counted for comparison with the order spectrum of the tread pattern, which is shown in Table 5- 1. It is clear that the number of blocks in one circumference is highly correlated with the order range in which peaks occur for the tread pattern parameters.

Table 5- 1: Tread pattern spectrum peak range of the tires.

Number	Number of blocks	Observed peak order range
Tire 12	77	75-80
Tire 15	72	70-77
Tire 18	65	60-70
Tire 19	60	58-62
Tire 20	81	79-85

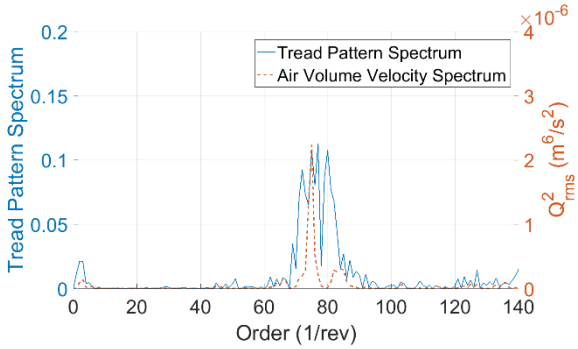

(a) Tire 12

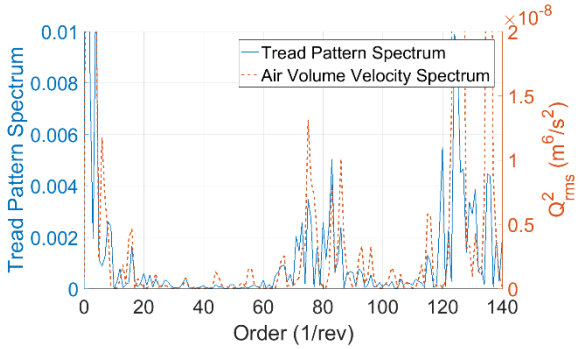

(b) Tire 15

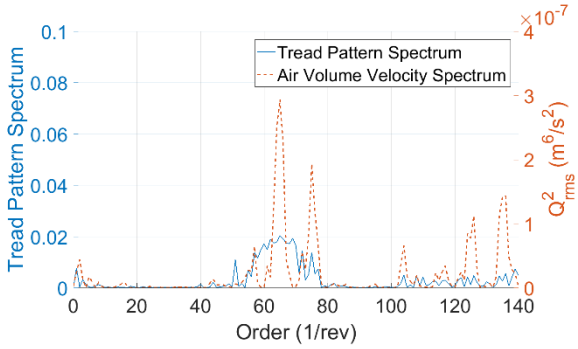

(c) Tire 18

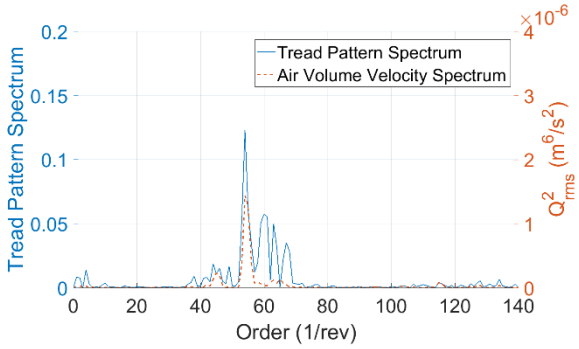

(d) Tire 19

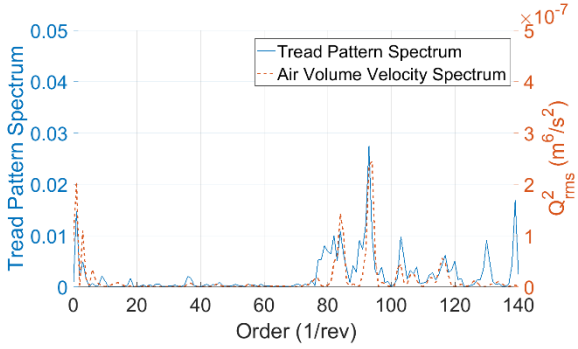

(e) Tire 20

Figure 5- 13: Tread pattern spectrum and air volume velocity spectrum comparison (order resolution=1).

5.3 Correlation between tread-pattern noise and tread pattern parameters

In this section, the order power spectra of the tread pattern parameters, including tread pattern spectrum and air volume velocity spectrum, are compared with the tread-pattern noise to investigate the relationship between them. The tread-pattern noise from both the leading edge and trailing edge are compared with the pattern parameters by visual inspection of the spectrum plot. The order resolution for all of the noise order spectra is 0.5, and the order resolution for all of the tread pattern and air volume velocity spectra is 1.

First, the tread pattern spectra and air volume spectra are compared with the total noise spectra. For Tire 12 (Figure 5- 14 and Figure 5- 15), the spectral contents near the 77 order display a good match. However, for the spectral content at lower orders, there is no match at all. For the other tires, the correlation between the tread pattern spectra/air volume spectra and total noise spectra is even more difficult to identify.

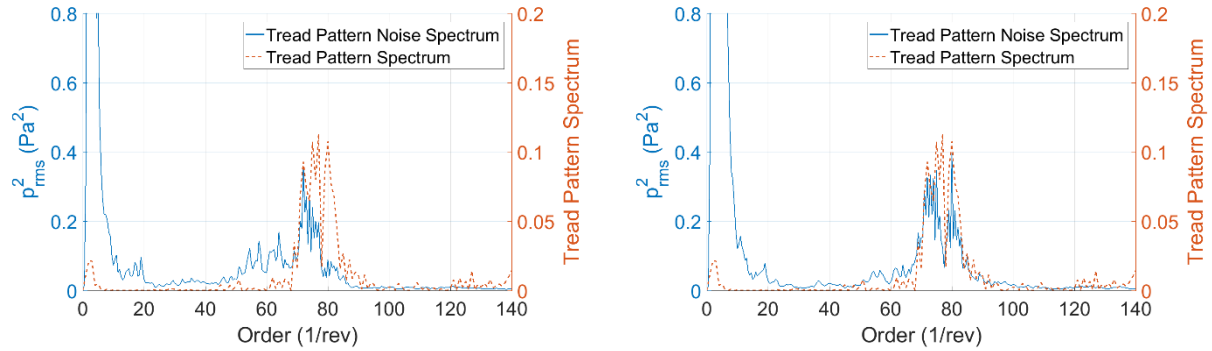

(a) Leading edge (b) Trailing edge

Figure 5- 14: Comparison between total noise spectrum and tread pattern spectrum-Tire 12 at 60 mph.

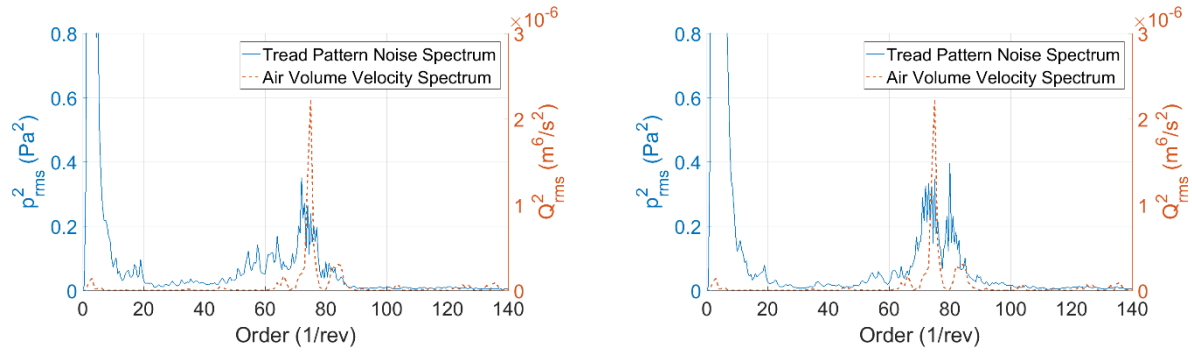

(a) Leading edge (b) Trailing edge

Figure 5- 15: Comparison between total noise spectrum and air volume velocity spectrum-Tire 12 at 60 mph.

Due to the lack of correlation between the tread pattern parameters and the total TPIN spectrum, the tread pattern spectra and the air volume velocity spectra are compared with the tread-pattern noise for all five tires. All of the tread-pattern noise data used in this section is the same as that used in Chapter 3. As shown in Figure 5- 16, Tire 12 has high tread-pattern noise and this corresponds with the high amplitude of the tread pattern power spectrum. The tread pattern spectra match well with the tread-pattern noise spectra at both the leading and the trailing edge. The air volume velocity for Tire 12 also matches well with the tread-pattern noise.

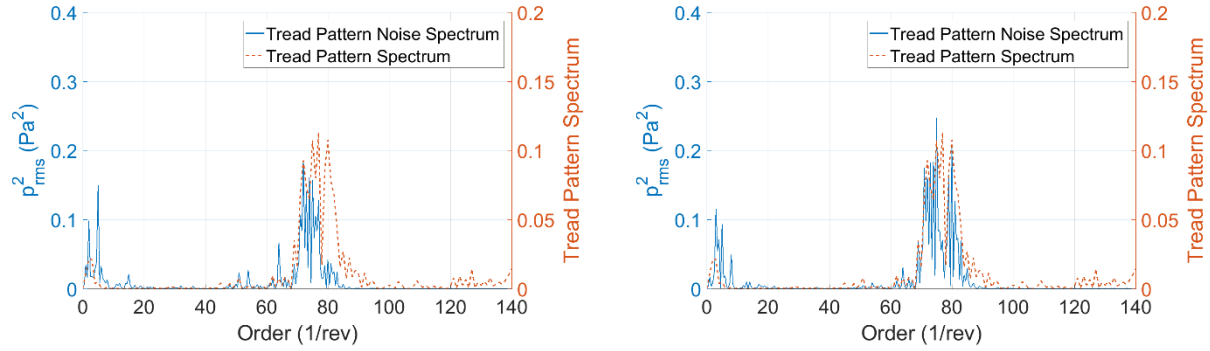

(a) Leading edge (b) Trailing edge

Figure 5- 16: Comparison between separated noise spectrum and tread pattern spectrum-Tire 12 at 60 mph.

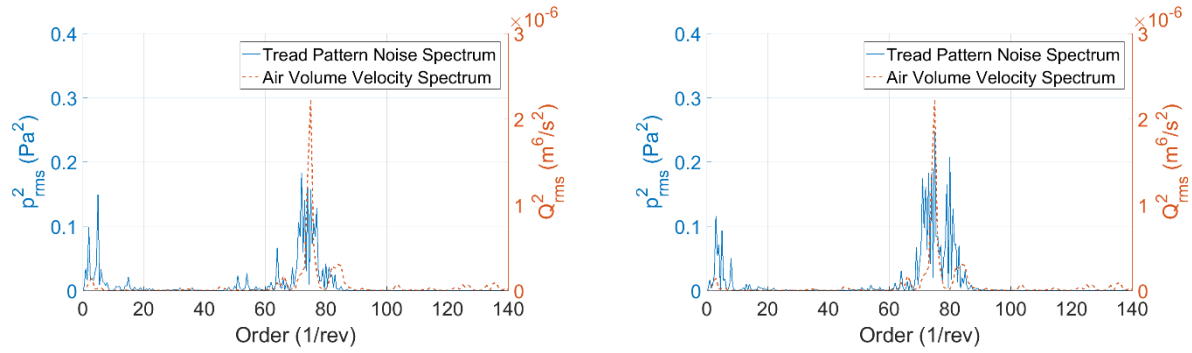

(a) Leading edge (b) Trailing edge

Figure 5- 17: Comparison between separated noise spectrum and air volume velocity spectrum-Tire 12 at 60 mph.

Tire 19 also has significant tread-pattern noise, and it is observable that it also has high tread pattern power spectrum amplitude. Both the tread pattern spectrum and air volume velocity spectrum match more closely at the leading edge than the trailing edge for Tire 19.

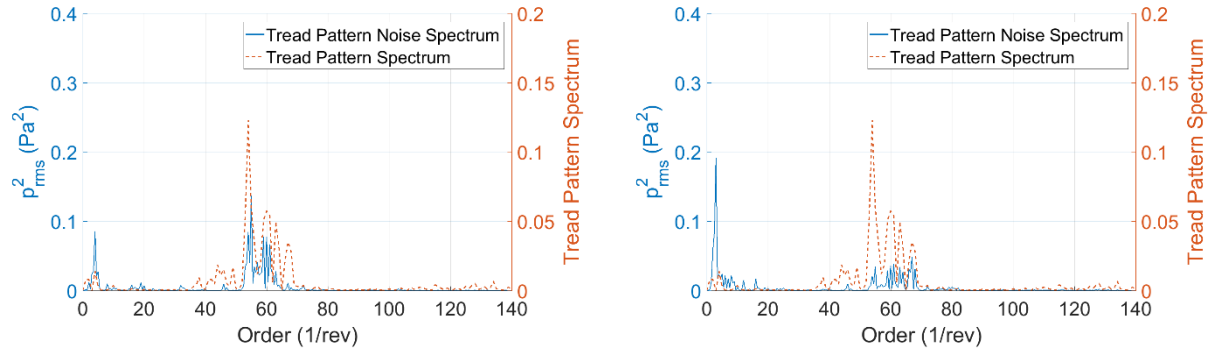

(a) Leading edge (b) Trailing edge

Figure 5- 18: Comparison between separated noise spectrum and tread pattern spectrum-Tire 19 at 60 mph.

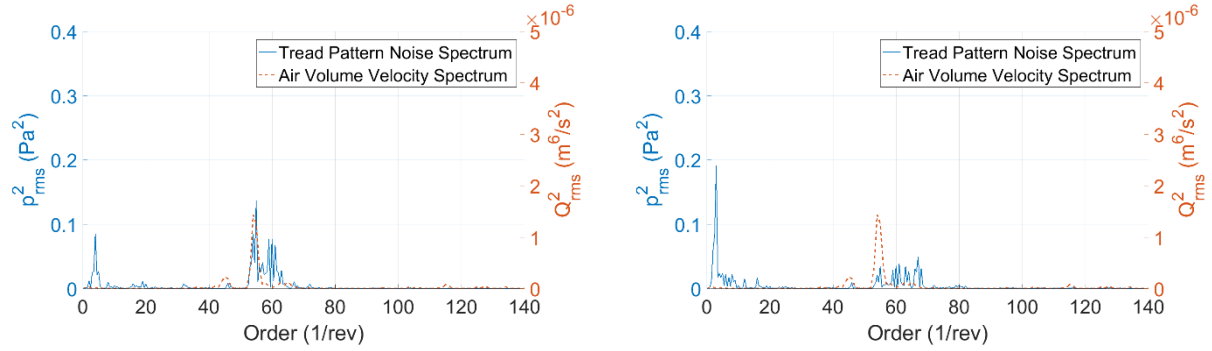

(a) Leading edge (b) Trailing edge

Figure 5- 19: Comparison between separated noise spectrum and air volume velocity spectrum-Tire 19 at 60 mph.

It was shown in Chapter 3 that the tread-pattern noise produced by Tire 15 is very low. As shown in Figure 5- 20, the tread pattern spectrum power level of Tire 15 is also very low. The correlation between the tread pattern parameters and tread-pattern noise for Tire 15 is not as close as that of Tire 12 and Tire 19. However, at the trailing edge, the amplitude for both noise and tread pattern spectra matches well at approximately 72 orders. The trailing edge shows a closer match than the leading edge for Tire 15.

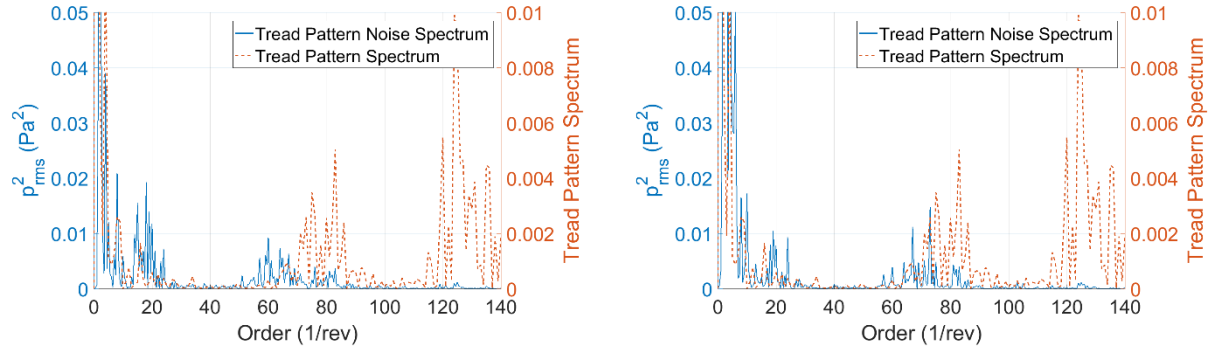

(a) Leading edge (b) Trailing edge

Figure 5- 20: Comparison between separated noise spectrum and tread pattern spectrum-Tire 15 at 60 mph.

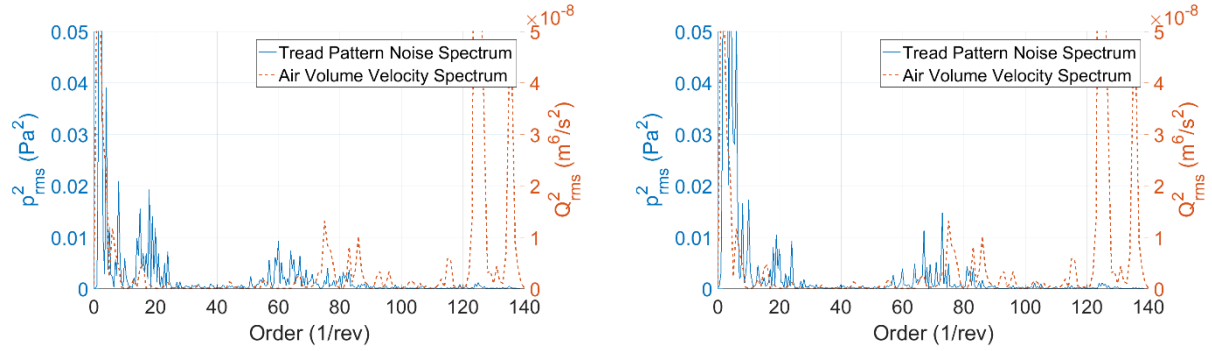

(a) Leading edge (b) Trailing edge

Figure 5- 21: Comparison between separated noise spectrum and air volume velocity spectrum-Tire 15 at 60 mph.

For Tire 18, the tread-pattern noise at the trailing edge matches the tread pattern spectrum from 60-75 orders, while at the trailing edge the two spectra match quite well for a broader order band. The air volume velocity spectrum has two peaks. The peaks on the right match well with the trailing edge spectrum, while the leading edge spectrum does not show any obvious peaks.

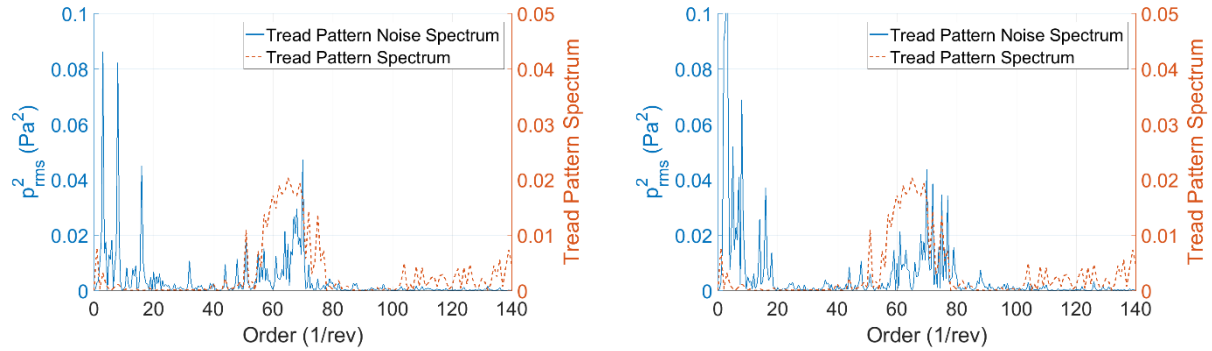

(a) Leading edge (b) Trailing edge

Figure 5- 22: Comparison between separated noise spectrum and tread pattern spectrum-Tire 18 at 60 mph.

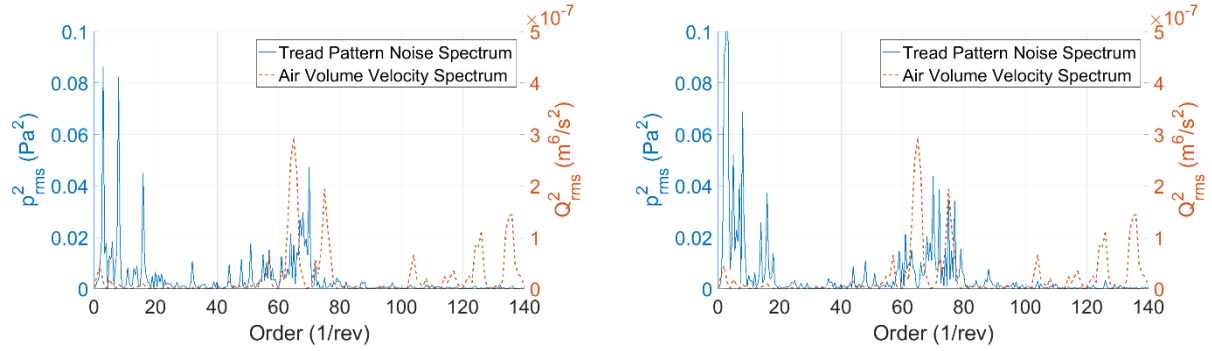

(a) Leading edge (b) Trailing edge

Figure 5- 23: Comparison between separated noise spectrum and air volume velocity spectrum-Tire 18 at 60 mph.

For Tire 20, the trailing edge noise matches quite well with the tread pattern spectrum at around 81 orders, while the leading edge signal shows three peaks around 81 orders. The air volume velocity matches more closely with the tread pattern noise at the leading edge, which is different from the case of Tire 18.

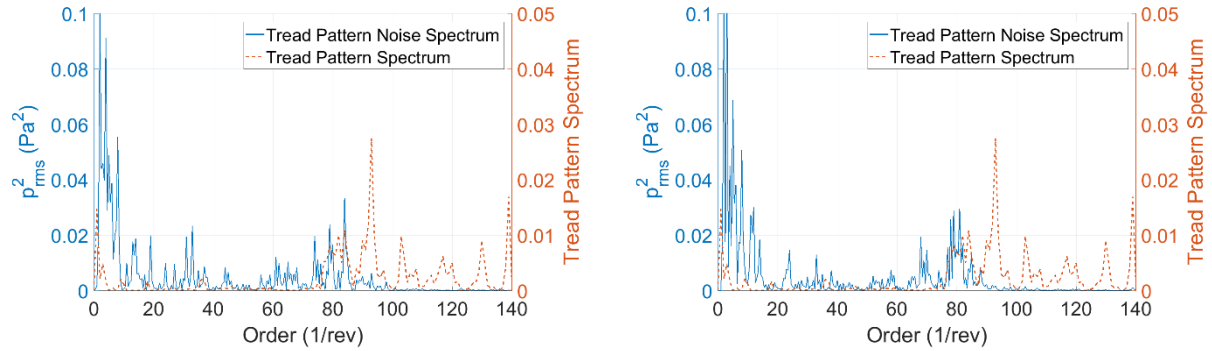

(a) Leading edge (b) Trailing edge

Figure 5- 24: Comparison between separated noise spectrum and tread pattern spectrum-Tire 20 at 60 mph.

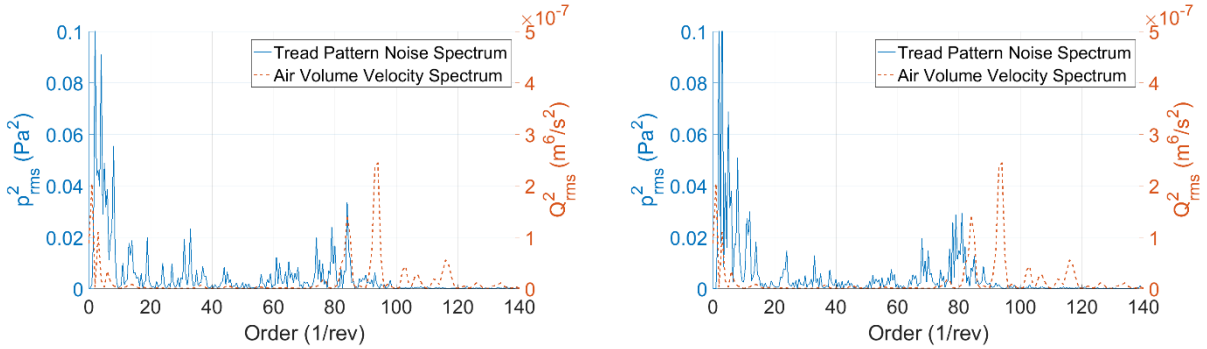

(a) Leading edge (b) Trailing edge

Figure 5- 25: Comparison between separated noise spectrum and air volume velocity spectrum- Tire 20 at 60 mph.

In summary, for most of the cases, the tread-pattern noise spectra indicate a reasonable match with both the tread pattern spectra and the air volume velocity spectra. Specifically, for the tires with higher tread-pattern noise, the matches are closer, while for the tires with low tread pattern noise, the spectra are not as well-aligned as it is for the tires with high tread pattern noise.

6 Conclusions

The study presented in this thesis mainly demonstrates the separation of tread pattern noise from the total tire-pavement interaction noise using order domain synchronous averaging. This new application of order tracking analysis and synchronous averaging have not been previously reported in the open literature for TPIN. The separation was validated by: (1) processing of a simulated signal; (2) comparison of the tread-pattern noise for the same tire on different pavements; (3) correlation between the separated noise with the tread pattern spectra and the air volume velocity spectra. In addition, when driving at a constant speed and on the same pavement, for different tires, the non-pattern noise spectra have similar shapes. The differences of the non-tread pattern spectra are possibly due to factors such as rubber hardness and tire stiffness.

In this study, a novel experimental setup that incorporates an optical sensor in the OBSI system was used. The conventional OBSI system contains two sound intensity probes, each of which has two microphone channels. However, in this study, an optical sensor takes the place of the fourth microphone channel. The experiments were conducted on both the eastbound and westbound sections of U.S. highway 460. Some additional data on different pavement types was also collected. In total, five tires were tested within a time frame of four days. Each tire was inflated with three pressures (40 psi, 32 psi, and 26 psi), and for each pressure level, tested at five speeds (45 mph, 50 mph, 55 mph, 60 mph, and 65 mph). The acceleration was also tested and it was combined with the 65 mph case. The successful collection of optical sensor signals provided critical information about tire revolutions.

The tread-pattern noise separation methodology is detailed in Chapter 3. The results show that, for tires with regular patterns, the noise level produced by the tread pattern is very low. However, for some special purpose tires, such as snow tires with patterns whose tread blocks are not well-randomized, the noise related to the pattern tends to be much higher. Both the constant-speed (60 mph) cases and the acceleration cases were analyzed. It was shown that only for Tire 12 and Tire 19, there are significant tread pattern noise components that can be separated from the total TPIN. The acceleration cases for all five tires with the 32 psi inflation pressure were

also processed. It was shown that the tread pattern noise components can be largely separated out for the tires with large tread pattern noise. One special case is that several tones appear in the noise signal collected at one section of east bound pavement. Separation was performed on the data, and it was confirmed that the tone is not induced by tread pattern.

Several signal processing techniques have been applied to the noise signals collected by the OBSI system. First, the autocorrelation analysis was performed to find periodicity in the signal. The data processed by autocorrelation shows clearer peaks, but still in a broad frequency range, which indicates that there are several periodic components in the tire-pavement interaction noise. The FD filter was used to separate the periodic components, but it did not work to extract the periodicity related to the tire rotation. Principal component analysis was applied to the data to reduce the dimension and preserve the majority of the information within the data. However, the principal components contained noise from too many sources and did not extract the information of our interest. Independent component analysis was also applied to the data. When the tread-pattern noise is high, it can be observed that the tread pattern produced components are clearer in some components. When the tread-pattern noise is insufficiently high, there is no sign of separation between the tread-pattern and non-tread-pattern noise. The application of the ICA to the OBSI multi-channel data should be investigated further with more microphones and other experimental setups.

In the future, more tires with different tread patterns and different sizes may be tested. Inclusion of a high resolution encoder in the optical sensor could allow for more precise monitoring of the vehicle speed and phase angle increment. In addition, further separation of the noise generated from different mechanisms can be carried out with a new experimental setup and implementation of proper signal processing techniques.

References

1. AASHTO. Standard Method of Test for Measurement of Tire/Pavement Noise Using the On-Board Sound Intensity (OBSI) Method. AASHTO TP 76. 2013.
2. Antoni J, Randall R. B, "Unsupervised noise cancellation for vibration signals—Part 2—a Novel frequency-domain algorithm". *Mechanical Systems and Signal Processing* 18 (1): 103–117, 2004.
3. Antone J, "Blind Separation of Vibration Components: Principles and Demonstrations". *Mechanical Systems and Signal Processing*, 19: 1166-1180, 2005.
4. ASTM F2493-14, Standard Specification for P225/60R16 97S Radial Standard Reference Test Tire, ASTM International, West Conshohocken, PA, 2014, www.astm.org
5. ASTM E1136-14, Standard Specification for P195/75R14 Radial Standard Reference Test Tire, ASTM International, West Conshohocken, PA, 2014, www.astm.org
6. Bekke D, Wijnant Y, De Boer A, Benzemer-Krijnen M, "Tread Pattern Noise Optimization by a Coupled Source Human Perception Model", *Inter-noise*, 2014.
7. Breitenbach A, Against Spectral Leakage. *Measurement*, 25:135-142, 1999.
8. Cao P, Yan X, Xiao W, Chen L, "A prediction model to coupling noise of road tread patterns and road texture", *The Eighth International Conference of Chinese Logistics and Transportation Professionals*, 2008.
9. Chen C. J, Kuan Y. D, Chen C. F, Sung M. F. Using CFD Technique to Investigate the Effect of Tire Rolling-Noise with Different Pattern Design. Applied Mechanics and Materials, 575: 469-472, 2014.
10. Comon P. Independent Component Analysis, A New Concept? *Signal Processing*, 36:287-314, 1994.
11. Dare T. P, "Generation mechanisms of tire-pavement noise," Purdue University, 2012.
12. Eisenblaetter J, Walsh S. J, Krylov V. V, Air-related Mechanisms of Noise Generation by Solid Rubber Tyres with Cavities. *Applied Acoutics*, 71: 854-860, 2010.
13. Ejsmont J. A, Sandberg. U, Taryma S, "Influence of tread pattern on tire/road noise," in *Transactions of the Society of Automotive Engineers*. Society of Automotive Engineers, Warrendale, 1984", pp. 1–9.

14. Fyfe. K. R, Munck. E. D. S. Analysis of Computed Order Tracking. *Mechanical and Signal Processing*, 11 (2): 187-205, 1997.
15. Gade. S, Herlufsen. H, Konstantin-Hansen. H, Wismer. H. J. Order Tracking Analysis. Bruel&Kjar, 1995.
16. Gagen M. J, Novel Acoustic Sources from Squeezed Cavities in Car Tires. *J Acoust Soc Am*, 106: 794–801, 1999.
17. Grosche. P, Mueller. M. Computing Predominant Local Periodicity Information in Music Recordings. IEEE Workshop on Applications of Signal Processing to Audio and Acoustics, 2009.
18. Gur B. M, Niezrechi C. Autocorrelation Based Denoising of Matanee Vocalization of using the Undecimated Discrete Wavelet Transform. J Acoust Soc. Am., 122 (1): 188-199, 2007.
19. Hanson D. I., James C. RS., NeSmith C. Tire/Pavement Noise Study. NCAT Report 04-02. United States; 2004. p. 49p – .
20. Hayden R. E, "Roadside noise from the interaction of a rolling tire with road surface," in *Proceedings of the Purdue Noise Conference*, West Lafayette, IN, 1971, pp. 62–67.
21. Hyvärinen A, Oja E. A Fast Fixed-point Algorithm for Independent Component Analysis. *Neural Computation*, 9: 1483-1492, 1997.
22. Hyvärinen A, Karhunen J, Oja E. Independent Component Analysis, John Wiley & Sons, 2001.
23. Hyvärinen A. Independent Component Analysis: Recent Advances. Phil Trans R Soc A 371: 20110534, 2013.
24. Kim G. J, Cho S. W, Kim N. G, "Prediction of the Tread Pattern Noise of the Quasi-static State Rolling Tyre", *The 29th International Congress and Exhibition on Noise Control Engineering*, 2000.
25. Kim S, Jeong W, Park Y, Lee S. Prediction Method for Tire Air-pumping Using a Hybrid Technique. *J. Acoust. Soc. Am.*, 119 (6): 3799-3912, 2006.
26. Kinsler L. E, Frey A. R, Coppens A. B, Sanders J. V. Fundamentals of Acoustics, Wiley, 2000.
27. Li T, Feng J, Burdisso R. A, Sandu C. The Effects of Speed on Tire-Pavement Interaction Noise (Tread-Pattern-Related and Non-Tread-Pattern-Related Noise). *35th Annual Meeting and Conference on Tire Science and Technology*, Akron, Ohio, USA, 2016.

28. Li T, Feng J, Burdisso R. A, Sandu C. The Effects of Tread Patterns on Tire-Pavement Interaction Noise. *INTER-NOISE*, Hamburg, Germany, 2016.
29. Liljegren K. “Visual and acoustic tyre tread design”, Chalmers University of Technology, 2008.
30. Liu Y, Li T, Liu Y, Su Y. Optimize the Structure Parameters of Tread Pattern Based on Fuzzy Generic Arithmetic. *International Conference on Measuring Technology and Mechatronics Automation*, 2010.
31. Lu W, Rajapakse J. C. Eliminating Indeterminacy in ICA. Neurocomputing, 50: 271-290, 2003.
32. Martin. N, Mailhes. C. About Periodicity and Signal to Noise Ratio-the Strength of the Autocorrelation Function. Conference on Condition Monitoring and Machinery Failure Prevention Technologies. Stratford-upon-Avon, United Kingdom, 2010.
33. McFadden, P. D. A Signal Processing Technique for Detecting Load Defects in a Gear from the Signal Average of the Vibration. Proc Instn Mech Engrs, 199 (4): 287-292, 1985.
34. McFadden, P. D. Interpolation Techniques for Time Domain Averaging of Gear Vibration. Mechanical System and Signal Processing, 3 (1): 87-97, 1989.
35. Ongel A, Kohler E, Harvey J, Principal Components Regression of Onboard Sound Intensity Levels. *Journal of Transportation Engineering*, 134 (11): 459-466, 2008.
36. Parker D. H, Garuso D. G, Blinn R. J, Thrasher D. B. Method for improving tread noise by relative rotation of a rib and simulating the effect thereof, US Patent 4788651, 1988.
37. Parthasarathy S, Mehta S, Srinivasan, S. Robust periodicity detection algorithms. *ACM International Conference on Information and Knowledge Management* (pp.874-875). ACM, 2006.
38. Potter R. W. Tracking and Resampling Method and Apparatus for Monitoring the Performance of Rotating Machines, *United States Patent* # 4,912,661, 1990.
39. Potter R. W and Gribler M, "Computed Order Tracking Obsoletes Older Methods," SAE Technical Paper 891131, 1989, doi: 10.4271/891131.
40. Priestley, M. B. *Spectral analysis and time series*. London, New York: Academic Press, 1982.
41. Sandberg U, “Tyre / road noise – Myths and realities”, *The 2001 International Congress and Exhibition on Noise Control Engineering*, 2001.

42. Sandberg U and Ejsmont J. A, *Tyre/road noise reference book*. Kisa, Sweden; Harg, Sweden: INFORMEX, 2002.
43. Tabachnik B. G, Fidell L. S. Using Multivariate Statistics, Fifth Edition. Pearson, 2007.
44. Tuma J, Runa B. Order Analysis and Averaging in the Time Domain of Gear Box Noise and Vibration Signals Tabachnik. *Sixth International Congress on Sound and Vibration*, 1999.
45. Xue Y, Cao J, Tian R, Ge Q. Feature Extraction of Bearing Vibration Signals Using Autocorrelation Denoising and Improved Hilbert-Huang Transform. International Journal of Digital Content Technology and Its Application, 6 (4): 150-158, 2012.

Appendix

Appendix-A Tire Terminology

Footprint: the contact patch between tire and ground, as shown in Figure A-1.

Tread pattern: the patterns of groove on tire surface.

Tread grooves: hollow part in the tread.

Circumferential grooves: sometimes called aqua lines, since they have very important functions on wet roads, where they enable contact on the ground. They are usually thick grooves extending around the whole tire.

Sipe: grooves that are very thin, the smallest cuts in the rubber.

Shoulder blocks: the outermost/innermost chunk of rubber that are in contact with the ground and are created from many grooves circumferentially around the tire, and running horizontally across the shoulder, out to the area where the blocks are no longer in contact with the ground.

Pitch length: the length of a shoulder block.

Cross bars: patterns that only have horizontal grooves.

Slick tire: tire with no tread pattern.

Figure A-1 Typical, simplified footprint shape.

Figure A-2 Tire tread terminology.
(http://www.offroaders.com/tech/AT-MT-Tires/tire-tech.htm)

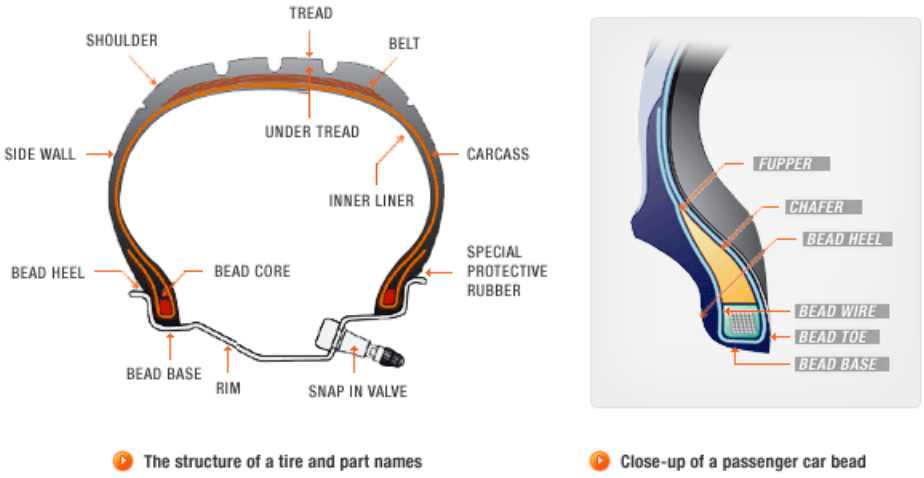

Figure A-3 Tire terminology illustration.
(http://www.hankooktireusa.com/Tech/Structure.aspx?pageNum=2&subNum=4&ChildNum=4)

Appendix-B Optical sensor specifications

Product Specifications	
Supply Voltage and Current	10 to 30V dc (10% maximum ripple) at less than 25mA (exclusive of load)
Supply Protection Circuitry	Protected against reverse polarity and transient voltages
Output Configuration	Bipolar: One current sourcing (PNP) and one current sinking (NPN) open-collector transistor
Output Rating	150mA maximum each output at 25°C, derated to 100mA at 70°C (derate H1mA per °C) **Off-state leakage current** less than 1 microamp **Output saturation voltage** (PNP output) less than 1 volt at 10mA and less than 2 volts at 150mA **Output saturation voltage** (NPN output) less than 200 millivolts at 10mA and less than 1 volt at 150mA
Output Protection Circuitry	Protected against false pulse on power-up and continuous overload or short-circuit of outputs
Output Response Time	Sensors will respond to either a “light” or a “dark” signal of 1 millisecond or longer duration, 500Hz max. 0.3 millisecond response modification is available. See Note below. 100 millisecond delay on power-up; outputs do not conduct during this time.
Repeatability	0.3 milliseconds. Response time and repeatability specifications are independent of signal strength.
Adjustments	LIGHT/DARK OPERATE select switch, and 15-turn slotted brass screw GAIN (sensitivity) adjustment potentiometer (clutched at both ends of travel). Both controls are located on rear panel of sensor and protected by a gasketed, clear acrylic cover.
Indicators	Exclusive, patented Alignment Indicating Device system (AID™, US patent #4356393) lights a rear-panel mounted red LED indicator whenever the sensor sees a “light” condition, with a superimposed pulse rate proportional to the light signal strength (the stronger the signal, the faster the pulse rate).
Construction	Reinforced PBT thermoplastic polyester housing, totally encapsulated, o-ring sealing, acrylic lenses, and stainless steel screws.
Environmental Rating	Meets NEMA standards 1, 2, 3, 3S, 4, 4X, 6, 12, and 13; IEC IP67
Connections	PVC-jacketed 4-conductor 2 m (6.5') or 9 m (30') cables, or 4-pin Euro-style quick disconnect (QD) fitting are available. QD cables are ordered separately. See page 8.
Operating Temperature	**Temperature:** -20° to +70° C (-4° to +158° F) **Maximum relative humidity:** 90% at 50° C (non-condensing)
Application Notes	The NPN (current sinking) output of dc MINI-BEAM sensors is directly compatible as an input to Banner logic modules, including all non-amplified MAXI-AMP and MICRO-AMP modules. MINI-BEAMs are TTL compatible.

Appendix-C Standard Reference Tires

This appendix includes the technical information of 2 types of standard reference test tire (ASTM F2493-14, 2014; ASTM E1136-14, 2014). The technical information are can be obtained from the references. The test data of the second SRTT are used in this study.

Appendix-D Basics Mathematics

Basic form of Fourier transform:

$$F(\xi) = \int_{-\infty}^{\infty} e^{-2\pi i \xi t} f(t) dt$$

Discrete Fourier transform:

$$F_k = \sum_{n=0}^{N-1} f_n \cdot e^{-2\pi i k n / N}$$

Inverse discrete Fourier transform:

$$f_n = \frac{1}{N} \sum_{k=0}^{N-1} F_k \cdot e^{2\pi k n / N}$$

Appendix-E Results of signal separation using optical signal

1. Constant speed cases-comparison of the tread-pattern/non-tread-pattern/total noise

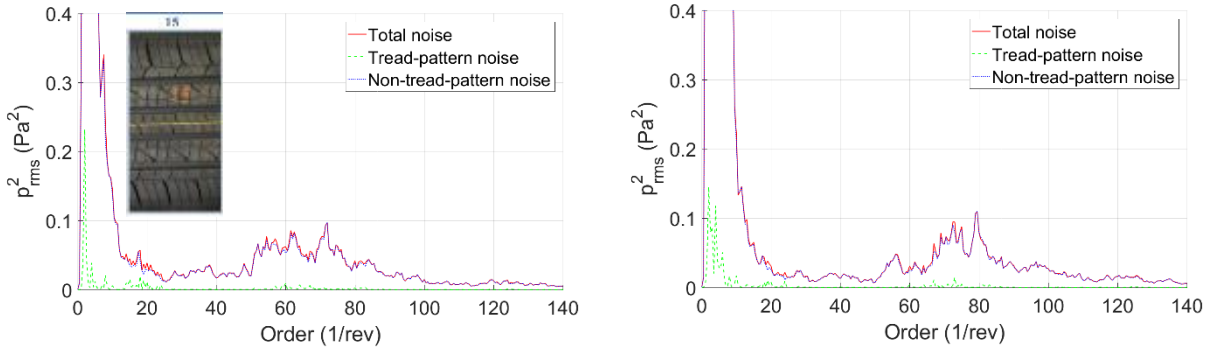

(a) Leading edge (b) Trailing edge

Figure E-1 Tire noise separation for Tire 15 at 60mph (order resolution: 0.5).

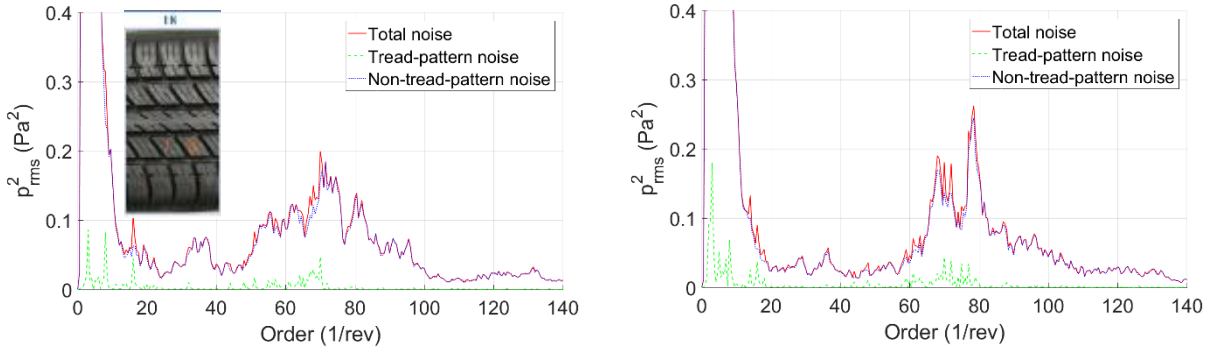

(a) Leading edge (b) Trailing edge

Figure E-2 Tire noise separation for Tire 18 at 60mph (order resolution: 0.5).

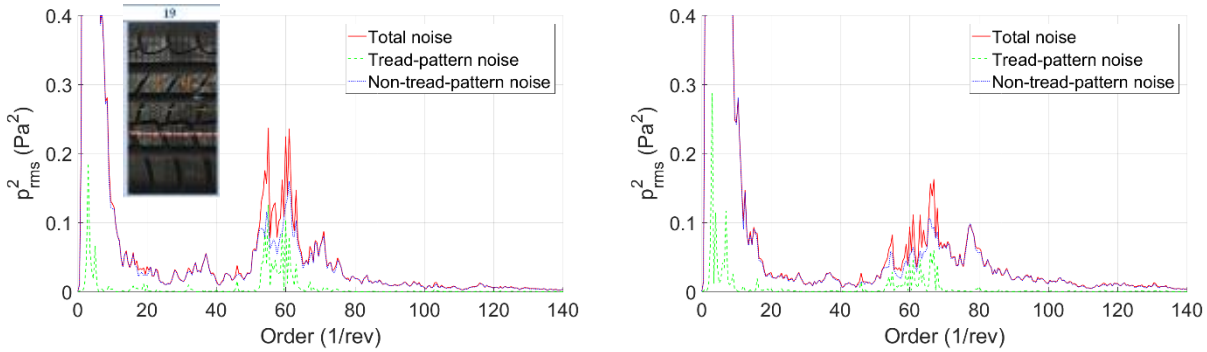

(a) Leading edge (b) Trailing edge

Figure E-3 Tire noise separation for Tire 19 at 60mph (order resolution: 0.5).

2. Acceleration cases-comparison of tread-pattern/non-tread-pattern/total noise

For Tire 20, it can be observed from Figure E-4 that, at the leading edge, there is some tread pattern noise from 60-80 orders, which is mostly separated. From Figure E-5, it can be observed that at the trailing edge there is obvious tread pattern component around 81 order, while the left noise does not show obvious peak value centered at a certain frequency.

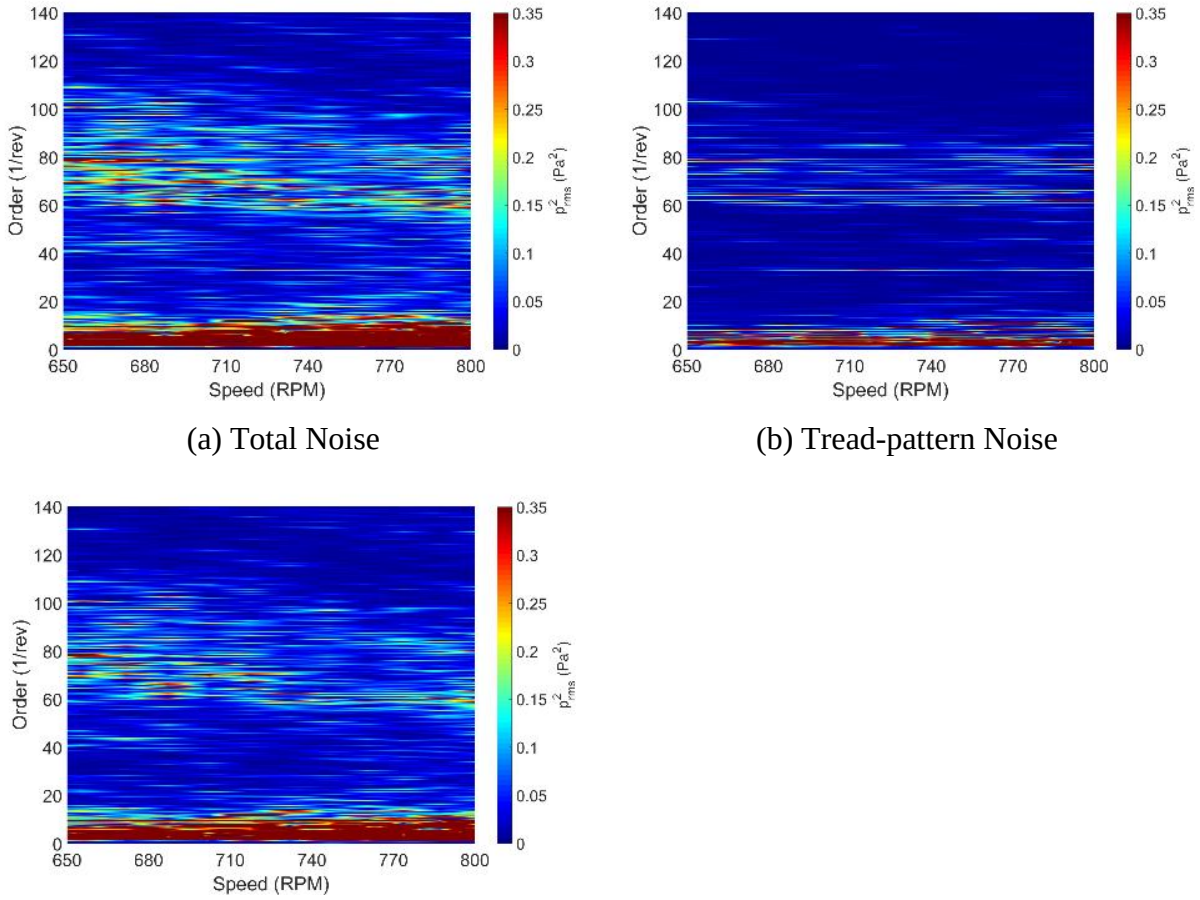

(a) Total Noise

(b) Tread-pattern Noise

(c) Non-tread-pattern Noise

Figure E-4 Tire noise separation for Tire 20 in acceleration (order resolution: 0.25)-leading edge.

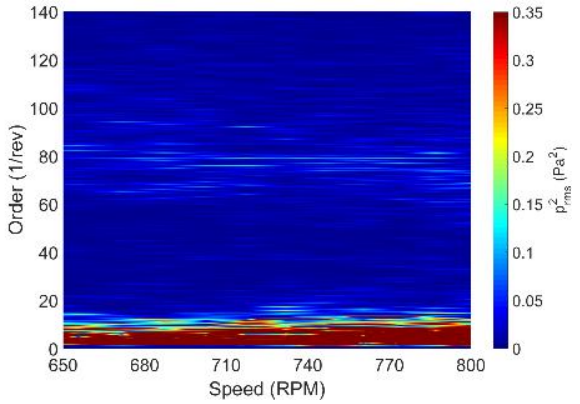

(a) Total Noise

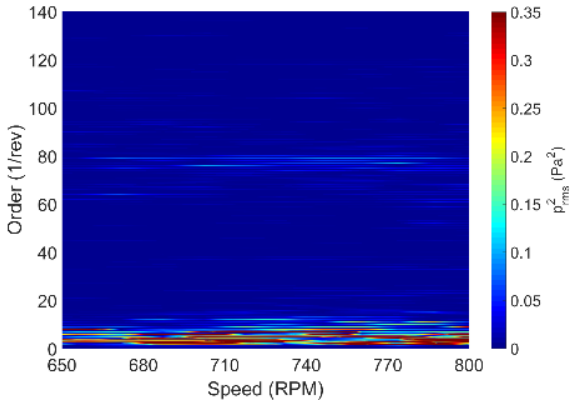

(b) Tread-pattern Noise

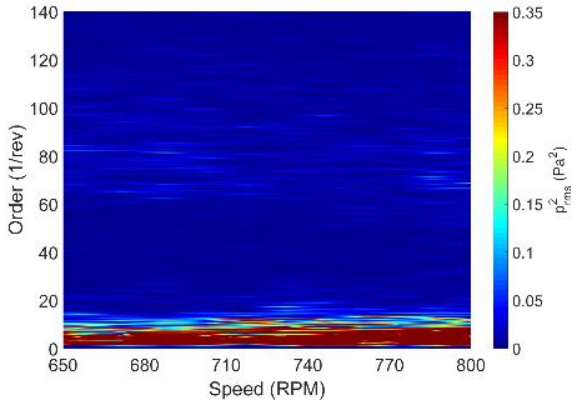

(c) Non-tread-pattern Noise

Figure E-5 Tire noise separation for Tire 20 in acceleration (order resolution: 0.25)-trailing edge.

For Tire 15, according to previous results at 60mph, the tread pattern noise is small when at a constant speed. From Figure E-6 and Figure E-7, it can be observed that the tread pattern noise is also very small in the acceleration process for Tire 15. There are 72 blocks for Tire 15. Some noise components for the tread pattern noise can be observed around 72 orders at both leading and trailing edge. Additionally, there are some noise components that do not appear at 72 order, which indicates good randomization of the tread block arrangement.

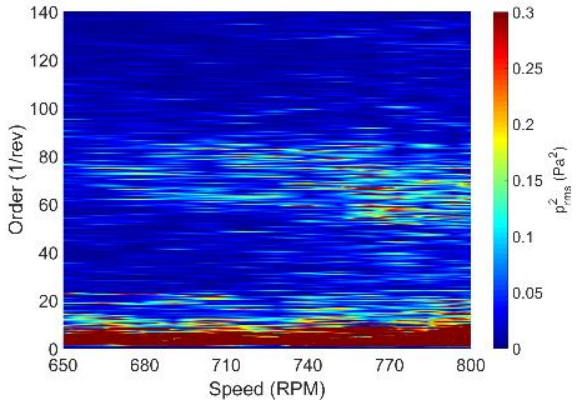

(a) Total Noise

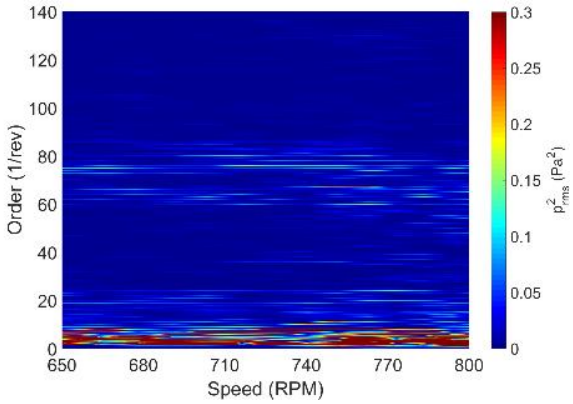

(b) Tread-pattern Noise

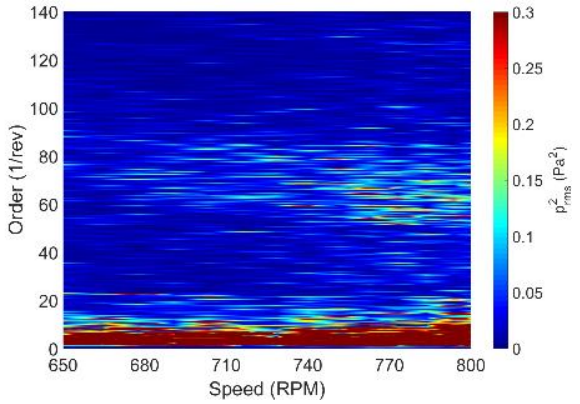

(c) Non-tread-pattern Noise

Figure E-6 Tire noise separation for Tire 15 in acceleration (order resolution: 0.25)-leading edge

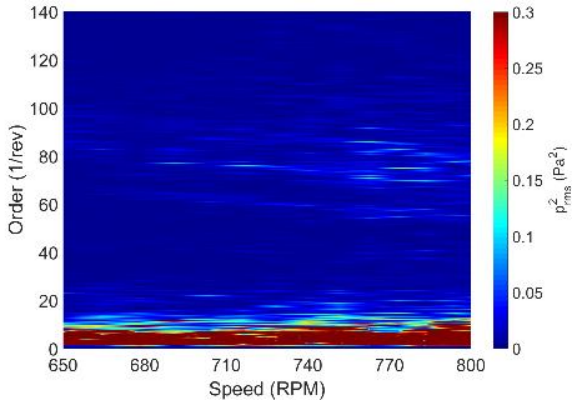

(a) Total Noise

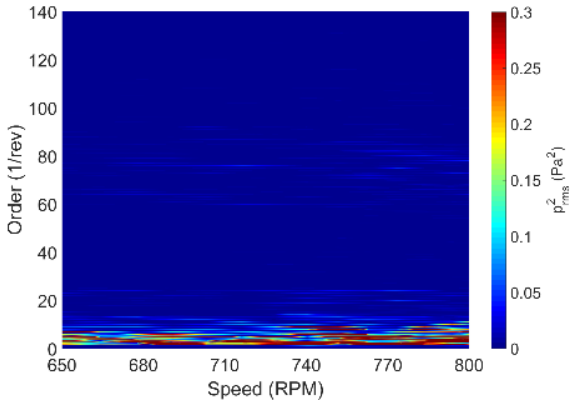

(b) Tread-pattern Noise

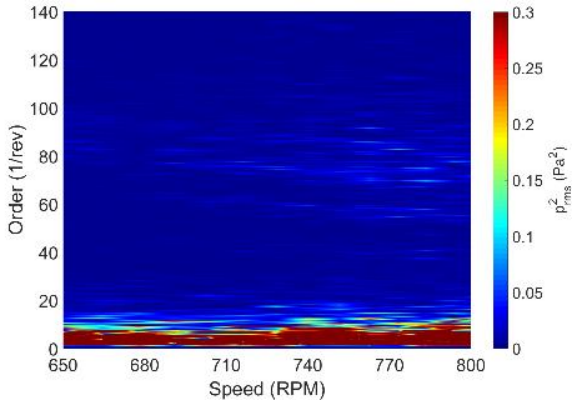

(c) Non-tread-pattern Noise

Figure E-7 Tire noise separation for Tire 15 in acceleration (order resolution: 0.25)-trailing edge.

For Tire 18, the separated noise level is higher than Tire 15 and Tire 20 as is shown in Figure E-8. At the trailing edge, when the speed is high, very obvious pattern noise can be observed close to the order 65. For the leading edge, a considerable amount of noise is separated. However, in Figure E-8 (c), it can be seen that the noise related to the rotation is not completely cancelled.

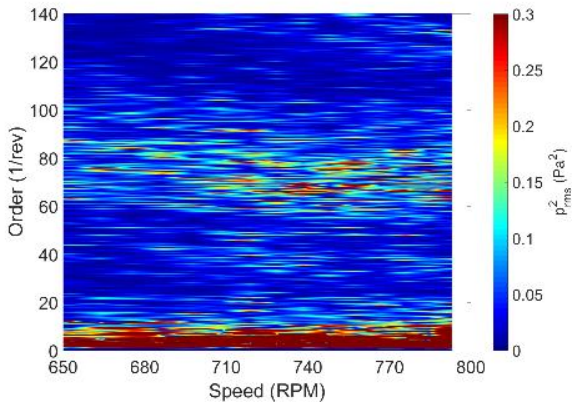

(a) Total Noise

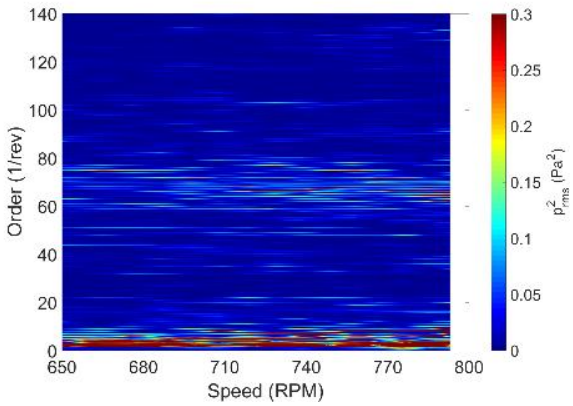

(b) Tread-pattern Noise

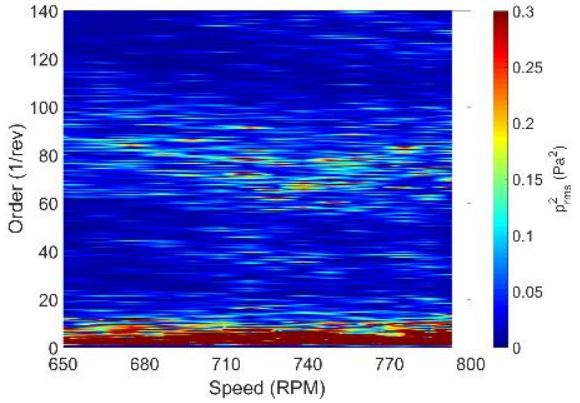

(c) Non-tread-pattern Noise

Figure E-8 Tire noise separation for Tire 18 in acceleration (order resolution: 0.25)-leading edge.

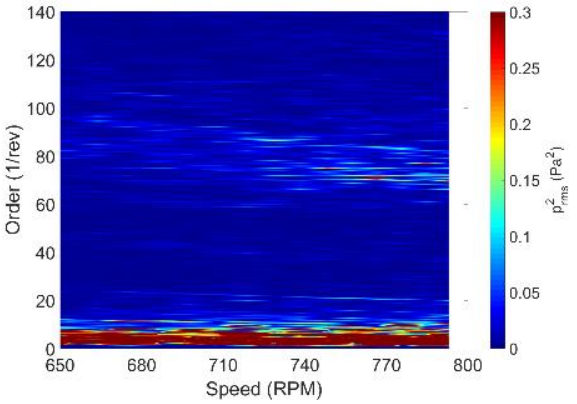

(a) Total Noise

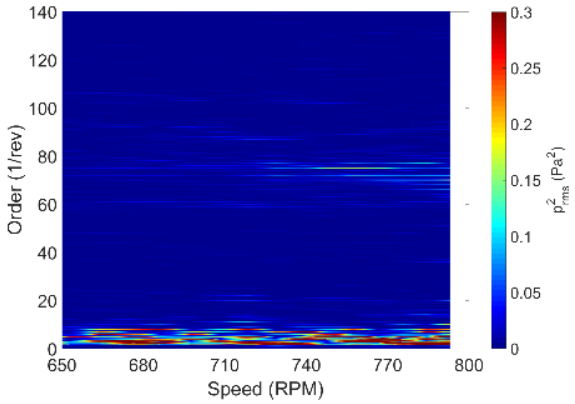

(b) Tread-pattern Noise

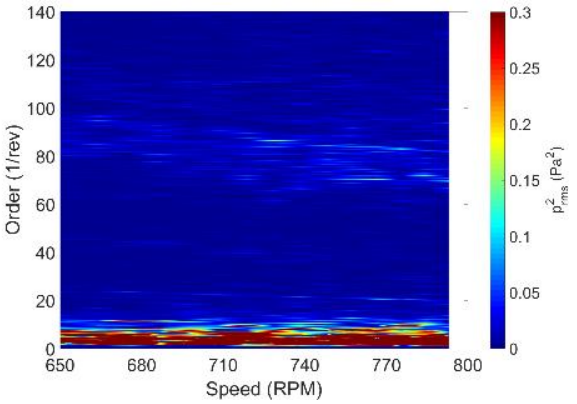

(c) Non-tread-pattern Noise

Figure E-9 Tire noise separation for Tire 18 in acceleration (order resolution: 0.25)-trailing edge.

For Tire 19, at the leading edge, there are obvious noise separations around the order of 60. However, the non-pattern noise also has large component around 60 orders. In previous study, when the speed is constant at 60 mph, the tread pattern noise is significant for Tire 19. For the acceleration case, the separated noise for the leading edge is also significant. However, the noise left after the separation also has high amplitude when the speed is high. For the trailing edge, the noise level is not high enough for observation when put in the same scale as leading edge.

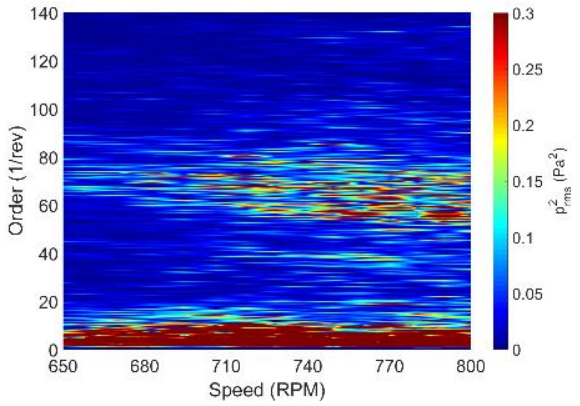

(a) Total Noise

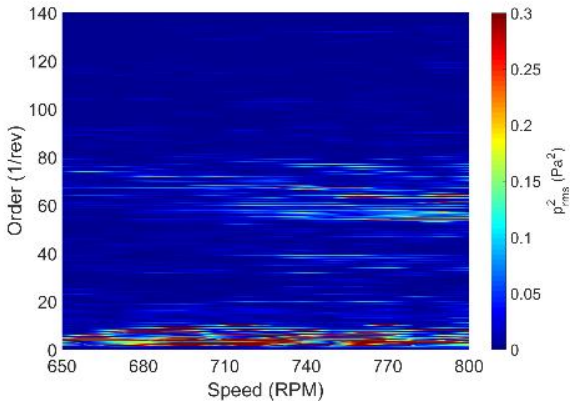

(b) Tread-pattern Noise

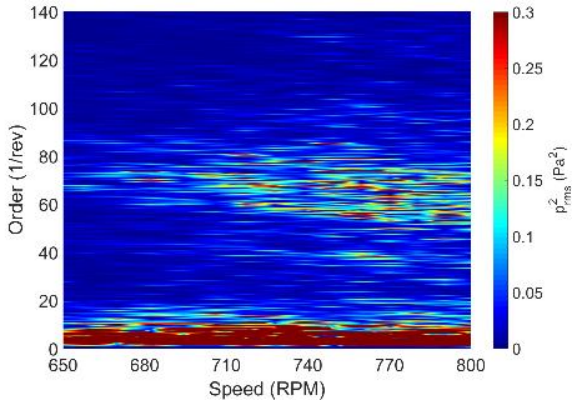

(c) Non-tread-pattern Noise

Figure E-10 Tire noise separation for Tire 19 in acceleration (order resolution: 0.25)-leading edge.

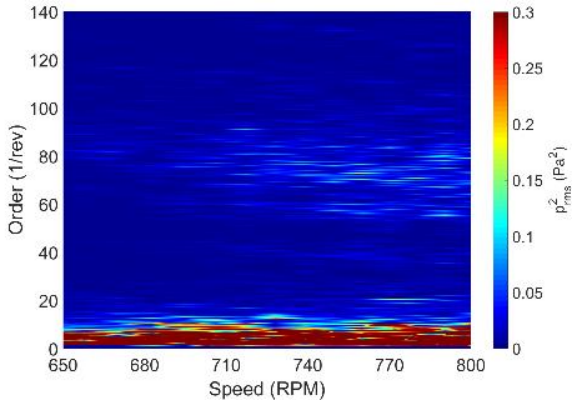

(a) Total Noise

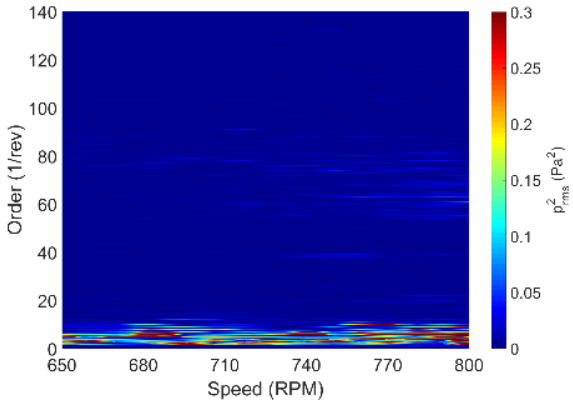

(b) Tread-pattern Noise

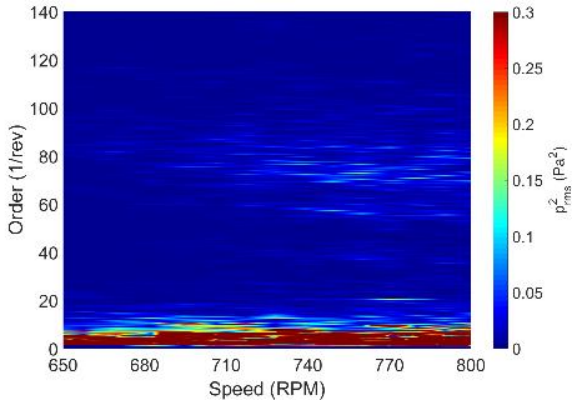

(c) Non-tread-pattern Noise

Figure E-11 Tire noise separation for Tire 19 in acceleration (order resolution: 0.25)-trailing edge.

Appendix-F Autocorrelation analysis theory and examples

First, sine wave is processed. The details of the signal are shown in Table F-1. The first 0.2s of the sine wave is plotted, as shown in Figure F-1 (a). Then, autocorrelation analysis is performed to the time signal, 2048 sampling points, which corresponds to the time duration of 0.2s, are chosen to be the lag duration. The autocorrelation of the sine wave is still a sine wave.

Table F-1 Sine wave-1 sample details

Amplitude	1
DC offset	0
Frequency (Hz)	200
Sampling frequency (Hz)	10240
Number of samples	8192
Sampling time (s)	0.7999

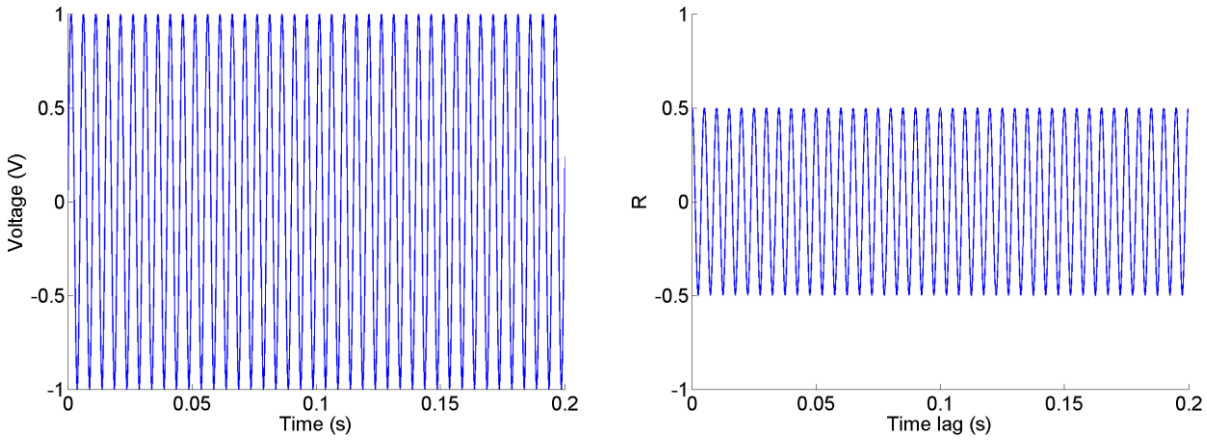

(a) Sine wave (b) Autocorrelation of sine wave

Figure F-1 Time history of sine wave (200Hz) and autocorrelation of the signal.

Then, DFT analysis was carried out for the time signal and autocorrelation value. As is shown Figure F-2, the frequency of the sine wave and autocorrelation is the same.

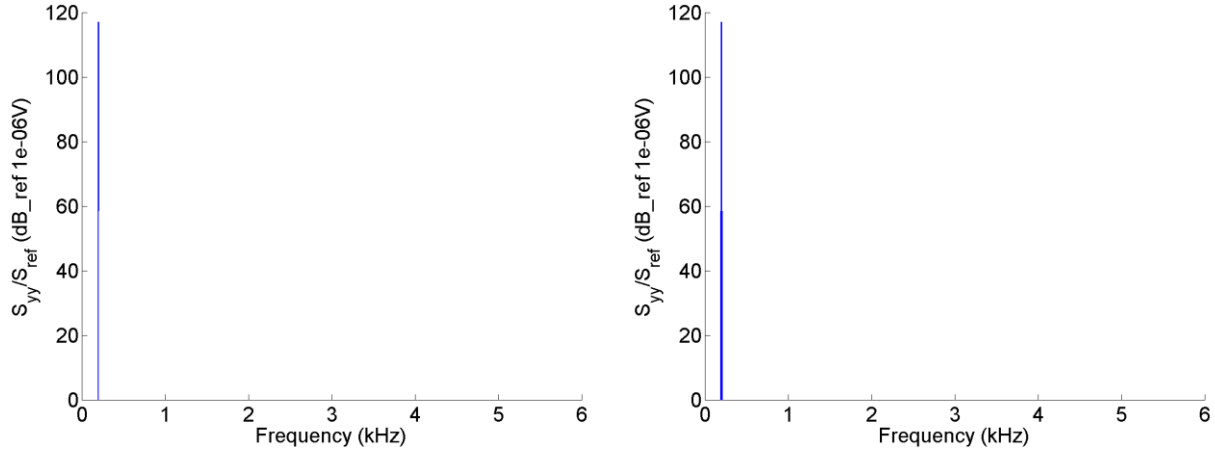

(a) Sine wave (b) Autocorrelation of sine wave

Figure F-2 Single sided spectrum of sine wave (200 Hz) and its autocorrelation.

Then, change the frequency of the signal and the corresponding sampling frequency. The details of the signal and sampling information are shown in Table F-2. The DFT for the limited time signal are sensitive to window length due to the spectral leakage (Breitenbach, 1999), and it works better when the sample length approximates integer number of signal period.

Table F-2 Sine wave-2 sample details

Amplitude	1
DC offset	0
Frequency (Hz)	197.5
Sampling frequency (Hz)	10240
Number of samples	8192
Sampling time (s)	0.7999

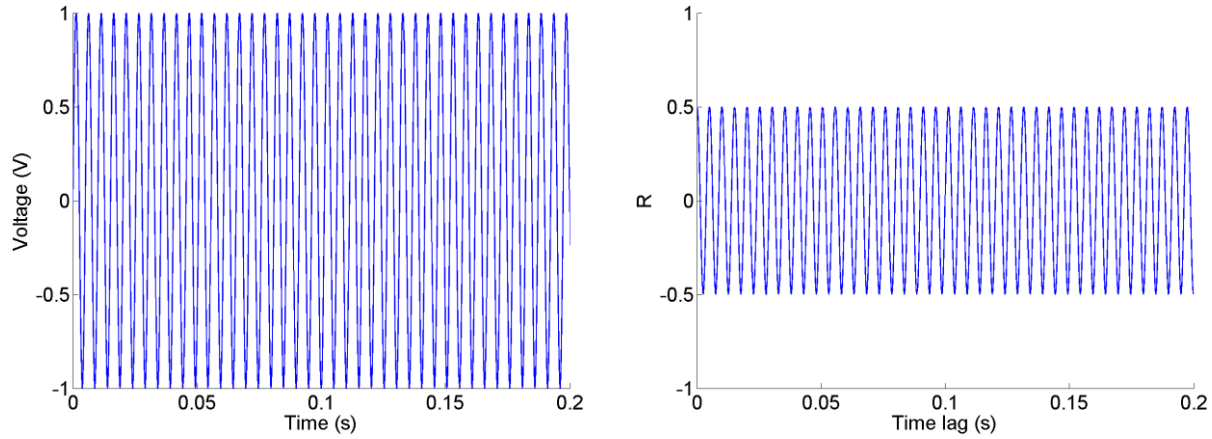

(a) Sine wave (b) Autocorrelation of sine wave

Figure F-3 Time history of sine wave (197.5 Hz) and autocorrelation of the signal.

Then, the DFT was performed to them. As is shown in Figure F-4, both the sine wave and autocorrelation show spectral leakage, due to the choice of window size is not exactly the integer multiples of sine wave period. The leakage of the autocorrelation is more obvious than the sine wave.

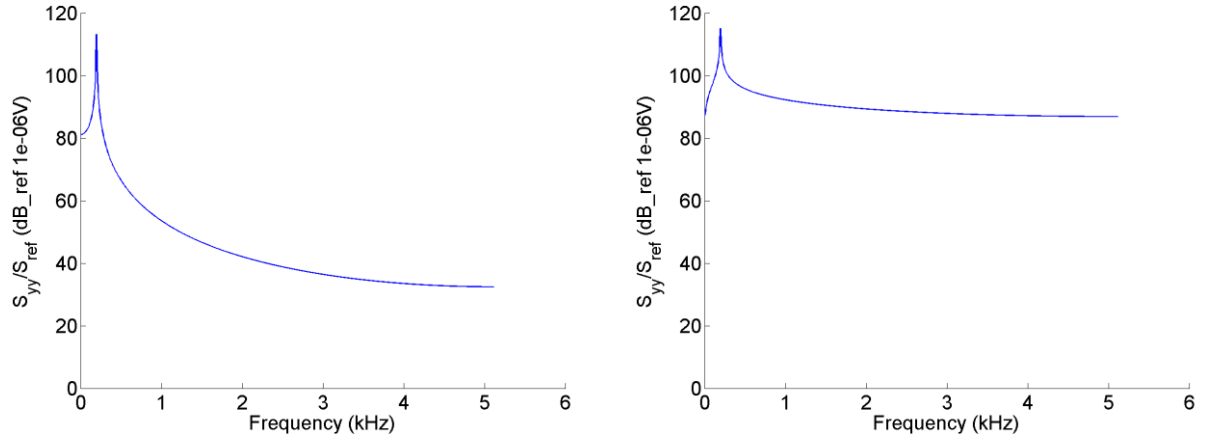

(a) Sine wave (b) Autocorrelation of sine wave

Figure F-4 Power spectrum of sine wave (197.5 Hz) and it autocorrelation.

In the last case, autocorrelation is performed to the periodic signals corrupted by both random noise and Gaussian white noise. As is shown in Figure F-5, the noise has been compressed significantly in the autocorrelation function. This shows the de-noising capability of the autocorrelation method.

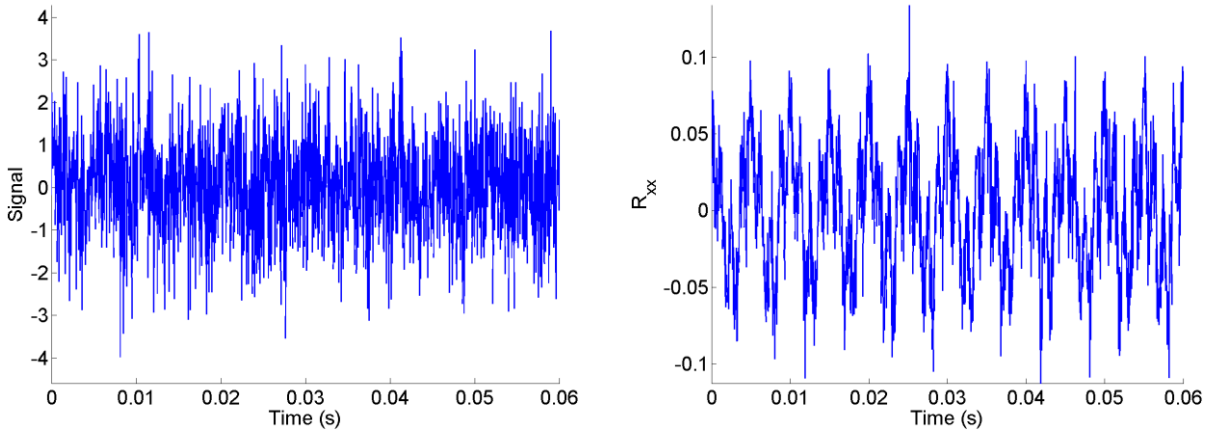

(a) Mixed signal (b) Autocorrelation of signal

Figure F-5 Time history of mixed signal and its autocorrelation.

Appendix-G Independent Component Analysis (ICA) Examples

The FastICA method can be used to separate signals that are mixed linearly. The MATLAB code package FastICA is used to perform independent component analysis to the signal. Several sample signals are processed in this section to test the capability of the codes.
(Website for ICA and BSS: http://research.ics.aalto.fi/ica/fastica/.)

1. Processing of the demo signals

As is shown in Figure F-1, four signals are mixed linearly to form four new mixed signals. In the case investigated in this part, the number of mixed signals are equal to the number of source signals. The case, for which the number of mixed signals is fewer that the number of source signals, will be investigated in the following parts.

The details of the original signals are shown in Table F-1. The signals are processed preliminarily for the preparation of ICA. First, the standard derivation mixed signals is calculated. Then, the signals are centered by removing the mean value. The original signals are shown as Figure F-2 a-d.

Table F-1 Description of original signals.

Number of samples for each signal	500
Number of signals	4
Signal types	1-Saw tooth periodic signal 2-Periodic wave 3-Sine wave signal 4-Random noise signal

The estimated mixing matrix, which mixes the source signals to the mixed signal is:

$$\begin{bmatrix} -0.7739 & -0.2807 & -0.9873 & 1.0548 \\ -0.0852 & -0.1476 & -0.333 & 0.3163 \\ -0.2134 & -0.4151 & -0.9618 & 0.5694 \\ -0.6291 & -0.2108 & -0.6724 & -0.9821 \end{bmatrix}$$

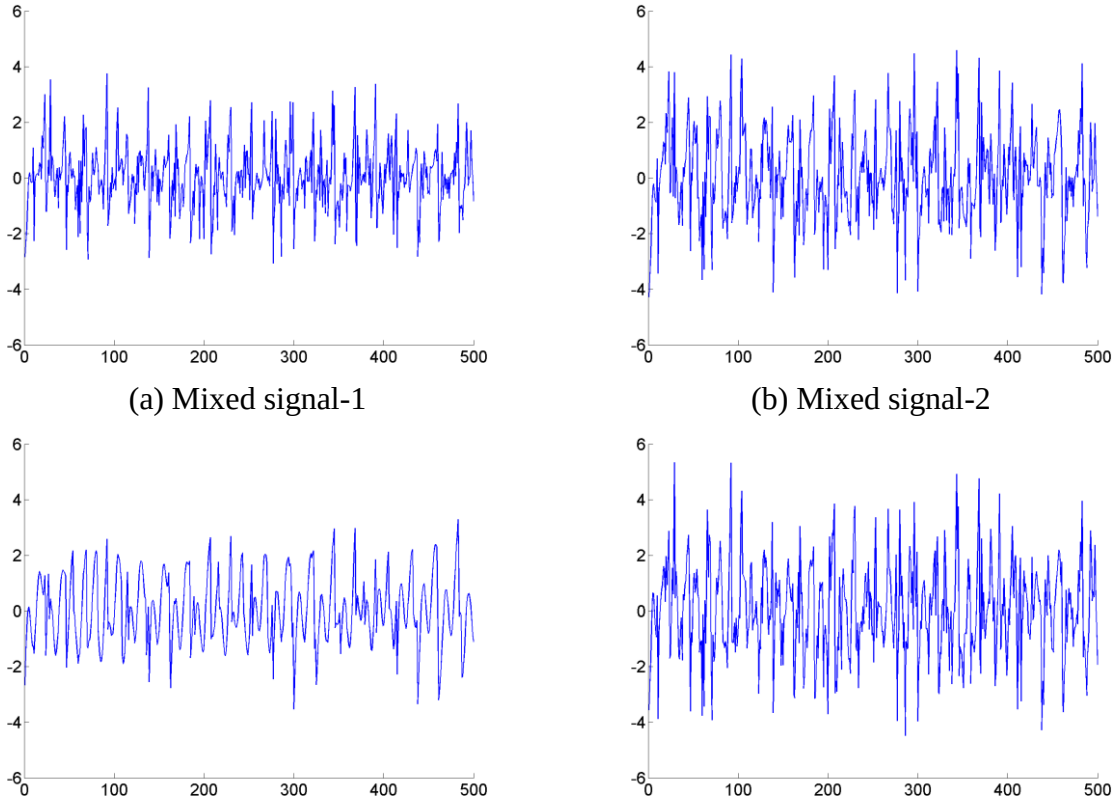

(a) Mixed signal-1 (b) Mixed signal-2

(c) Mixed signal-3 (d) Mixed signal-4

Figure F-1 Time history of the mixed signals.

It can be seen that the separated ICs remain high fidelity to the original signals.

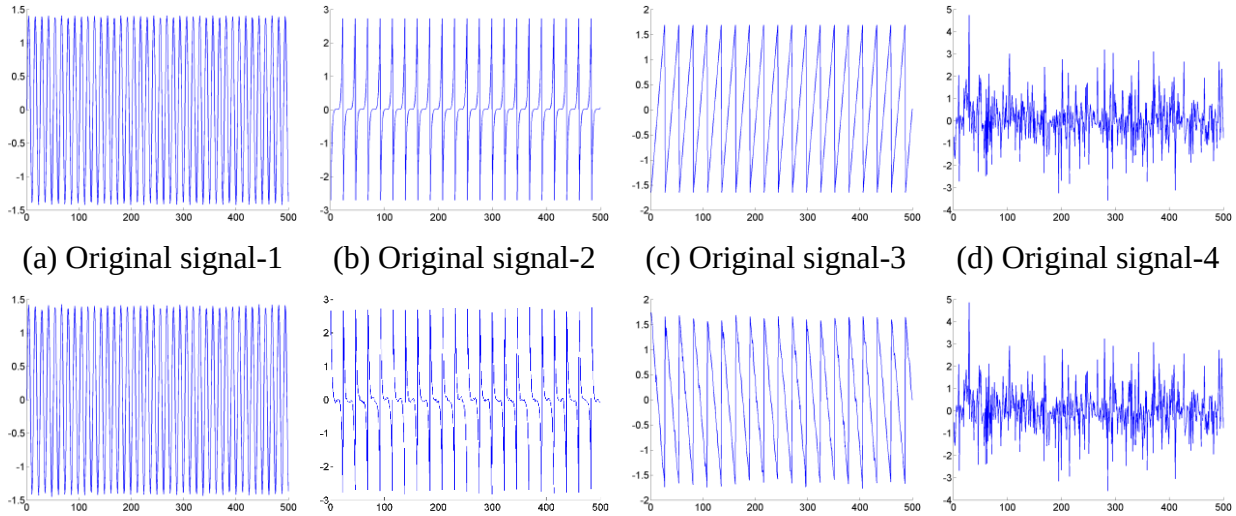

(a) Original signal-1 (b) Original signal-2 (c) Original signal-3 (d) Original signal-4

(e) Separated signal-1 (f) Separated signal-2 (g) Separated signal-3 (h) Separated signal-4

Figure F-2 Demonstration Original signals and decomposed signals.

2. Processing of simulating signals

According to literature (Lu et al, 2003), when the number of measured signal components is fewer than the number of independent components (ICs), the ICs are not fully identifiable in most cases, due to the non-invertibility of the mixing matrix. However, because little is known about the number of noise sources of the tire noise, it is necessary to investigate the cases that the number of measured signals is less than ICs. Given the condition that four microphones aligned in two pairs are used for data acquisition, two linearly mixed signals are generated by mixing the source signals linearly in this part. The details of the source signals are shown in Table F-2. The time history and frequency spectra of the signals are shown in Figure F-3 and Figure F-4, respectively. As is in the previous part, the source signals are normalized and centered.

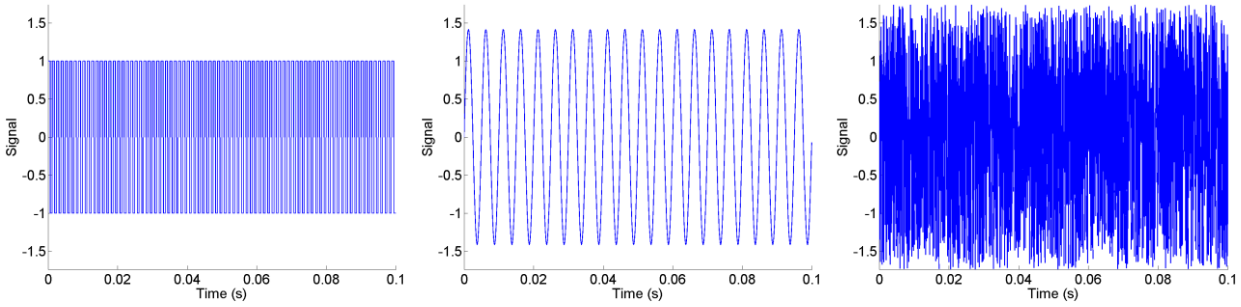

(a) Sine wave (b) Rectangular wave (c) Random noise

Figure F-3 Time history of the source signals-set 1.

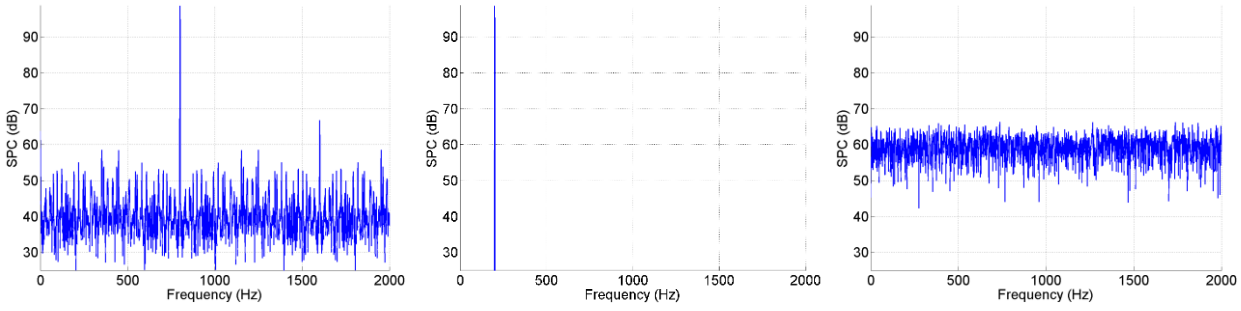

(a) Sine wave (b) Rectangular wave (c) Random noise

Figure F-4 Spectra of source signals-set 1.

In the first case, the mixing matrix to mix the source signals into the mixed signals is,

$$\begin{bmatrix} 0.55 & 0.6 & 0.3 \\ 0.35 & 0.7 & 0.5 \end{bmatrix}$$

Table F-2 Tire noise mimicking source signal details.

Time duration (s)	2
Number of samples	51201
Sampling frequency (Hz)	25600
Types of signals	1-Sine wave (variance normalized) 2-Periodic rectangular wave (variance normalized) 3-Non-Gaussian random noise (variance normalized)
Sine details	Frequency (Hz): 200
Rectangular details	Frequency (Hz): 800
Noise signal details	Randomly generated numbers (variance-normalized)

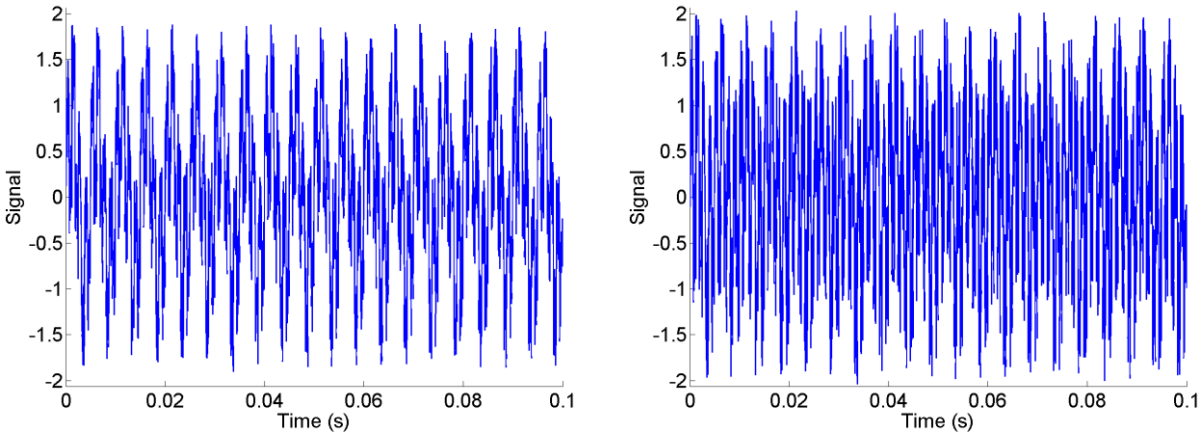

(a) (b)

Figure F-5 Mimicking tire noise signals-set_1-mixture_1. (a) Time series of mixed signal-1; (b) Time series of mixed signal-2.

The spectrum of the mixed signals are show in Figure F-6.

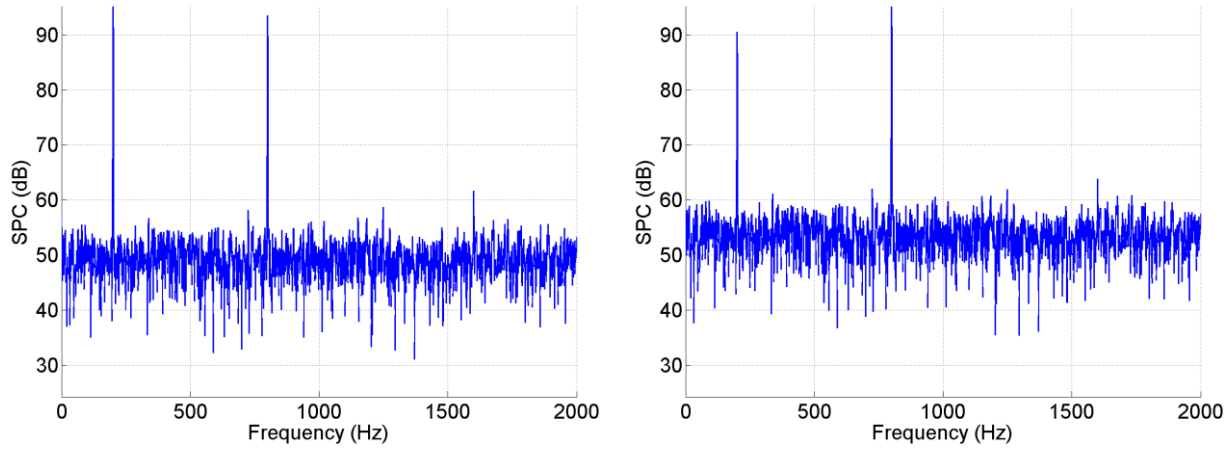

(a) (b)

Figure F-6 Spectrum of the mimicking tire noise signals-set_1-mixture_1. (a) Spectrum of mixed signal-1; (b) Spectrum of mixed signal-2.

The joint distribution between two mixed signals has been plotted (Figure F-7). It is clear that the two mixed signals are not independent, as the distribution of the signals has obvious orientation and it is not orthogonal to the axis.

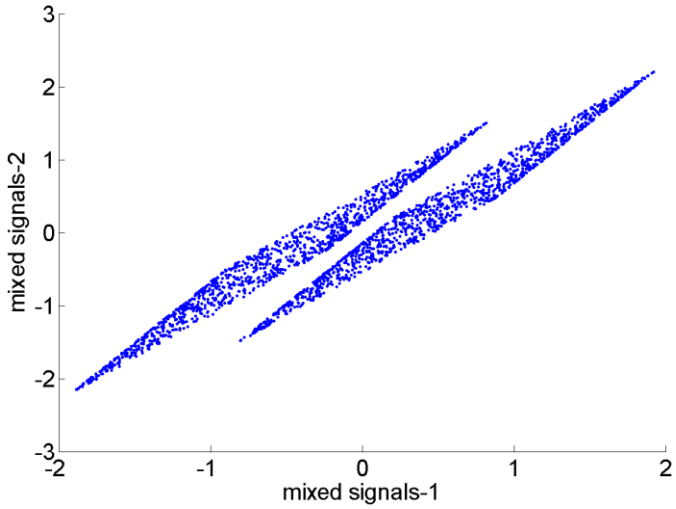

Figure F-7 Joint distribution of two mixed signals-set_1-mixture_1.

The separated independent components (ICs) are shown in Figure F-8. From observation, the first IC shows more low frequency periodic components while the second shows more high frequency signals. To characterize the properties of the ICs, spectra of them have been calculated and are shown in Figure F-9. From the power spectra, it is evident that the second IC contains mostly high frequency signal while the low frequency signal are mostly preserved in the first IC. The results indicate that the ICA is capable of separating the two periodic signal when the low level noise is present and only two observations are available.

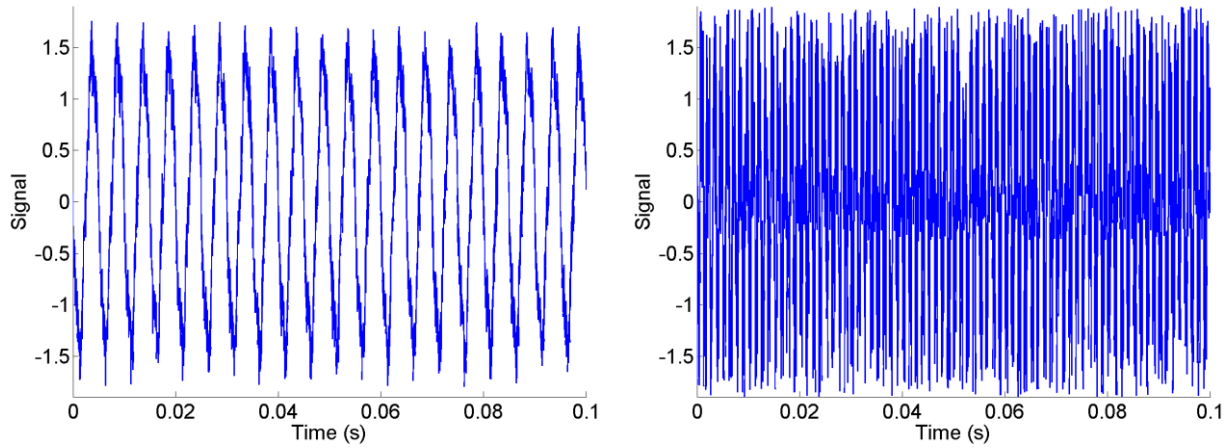

(a) IC-1 (b) IC-2

Figure F-8 Time history of the independent components.

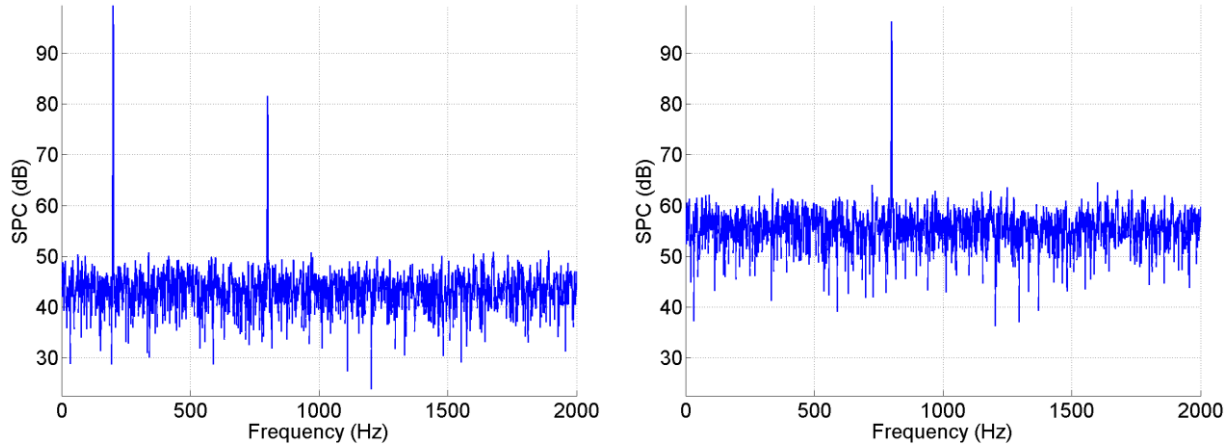

(a) IC-1 (b) IC-2

Figure F-9 Spectrum of the independent components.

The joint distribution of different the two independent component is plotted (Figure F-10). As is shown in this figure. The angle between the sides becomes larger, which means the data is more whitened. However, the whole shape does not show much rotation, which means that the two components are not fully independent.

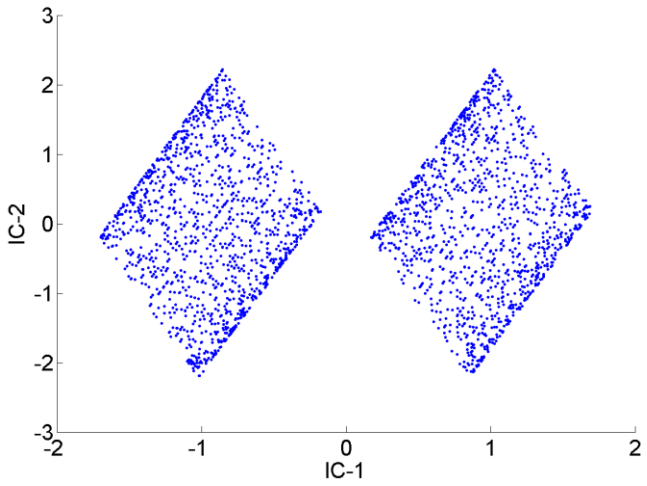

Figure F-10 Joint distribution of two independent components-set_1-mixture_1.

To investigate the effect of the noise ratio, and the signals to noise ratio is decreased by changing the mixing coefficients. The new mixing matrix is that,

$$\begin{bmatrix} 0.4 & 0.6 & 2 \\ 0.5 & 0.3 & 3 \end{bmatrix}$$

The time history of the new set of mixed signals are shown in Figure F-11, and the corresponding power spectra are shown in Figure F-12. The time series and spectra of separated ICs are shown in Figure F-14 and Figure F-15, respectively. Comparing the spectra of the ICs for the two set of data (Figure F-9 and Figure F-15) with different noise ratio, it can be found that, when the noise level is large enough, one of the IC contains much noise information when the noise in another IC can be largely separated out.

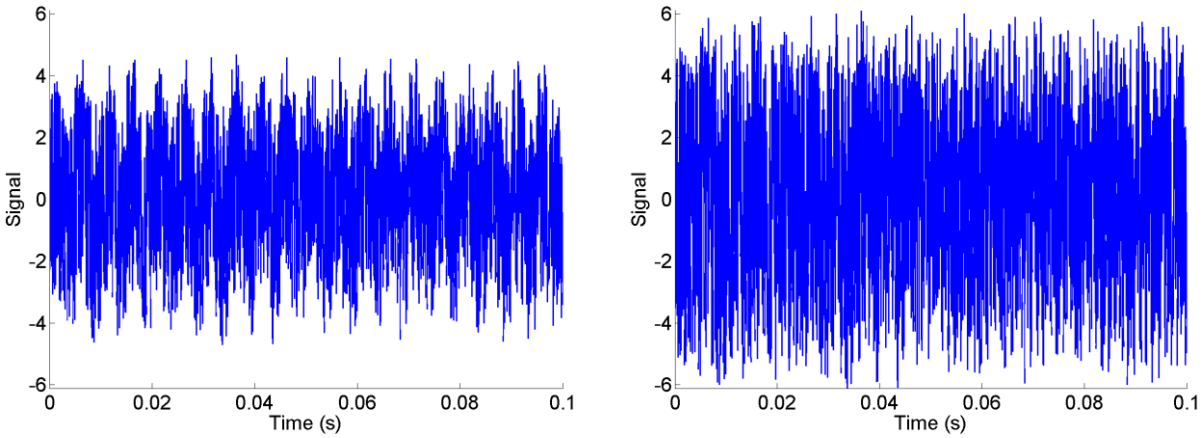

(a) Mixed signal-1 (b) Mixed signal-2

Figure F-11 Time history of the mimicking tire noise signals-set 2.

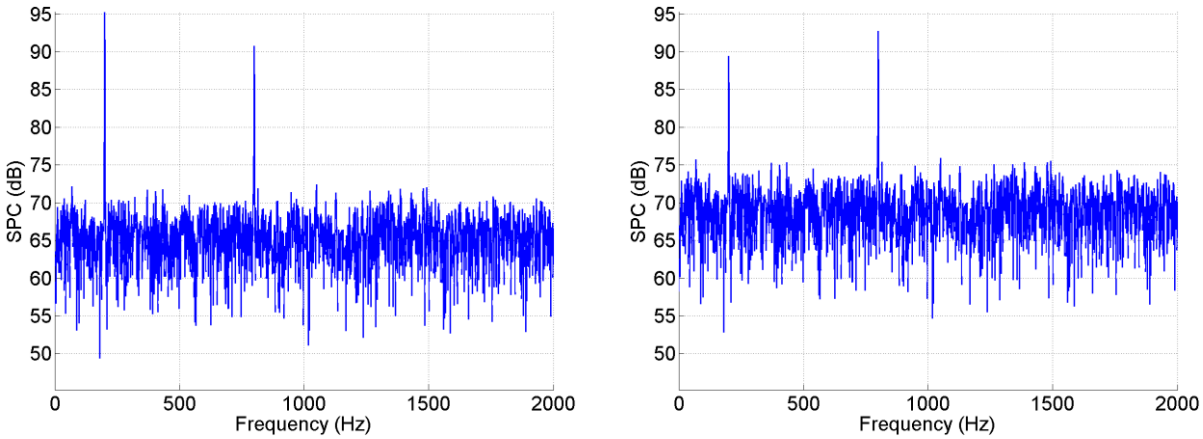

(a) Mixed signal-1 (b) Mixed signal-2

Figure F-12 Spectrum of the mimicking tire noise signals-set 2.

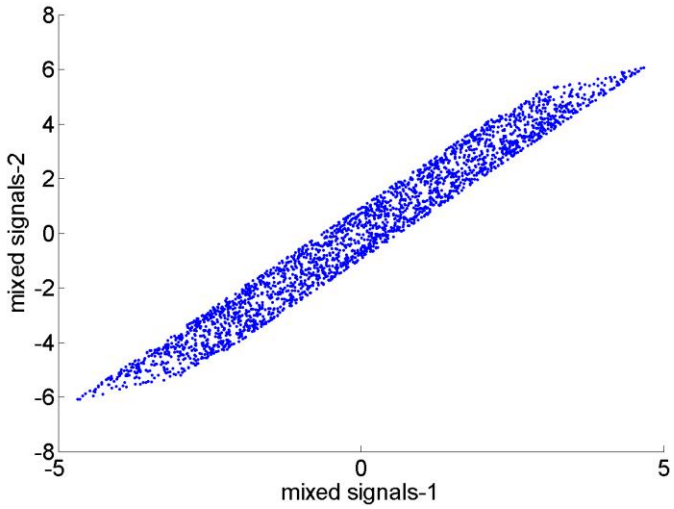

Figure F-13 Joint distribution of two mixed signals-set 2.

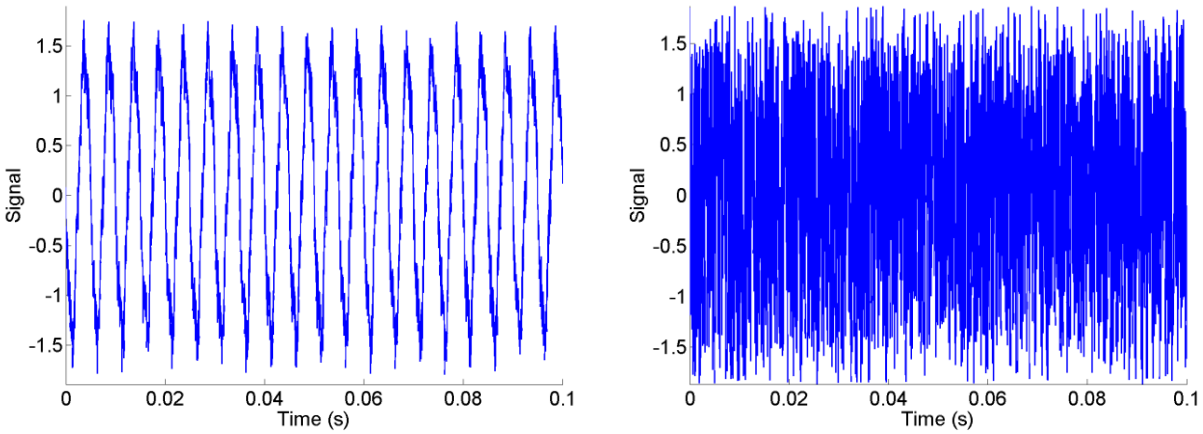

(a) IC-1 (b) IC-2

Figure F-14 Time history of the independent components.

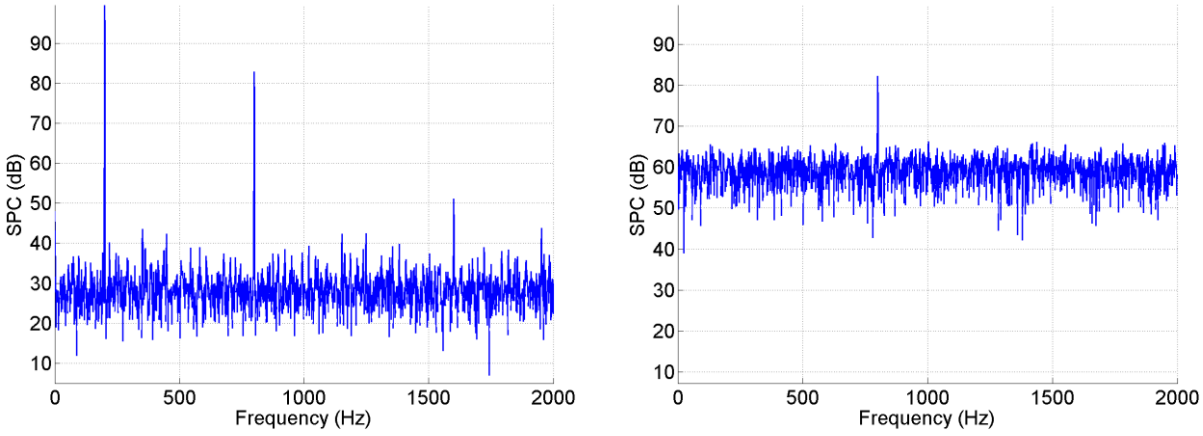

(a) IC-1 (b) IC-2

Figure F-15 Spectrum of the independent components.

Analyzing both the spectral and the joint distribution of the independent components. It can be concluded that IC 1 is mainly a mixture of two source signals and component 2 is mainly the random noise. They are mostly independent of each other.

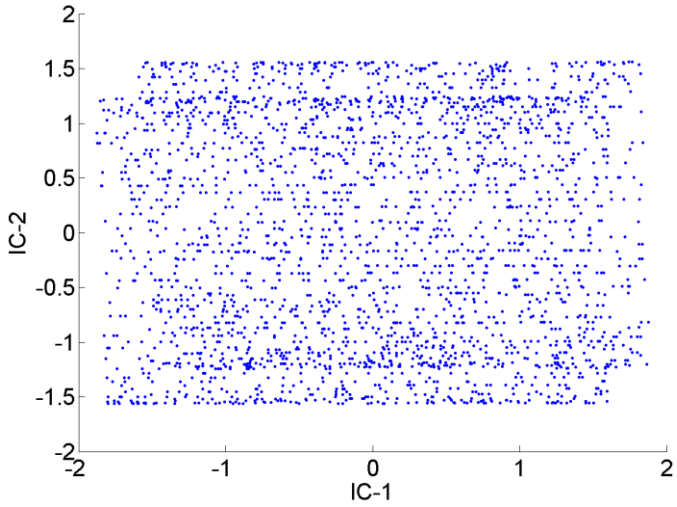

Figure F-16 Joint distribution of two independent components-set_1-mixture_2.